UNIVERSITY OF OKLAHOMA

GRADUATE COLLEGE

MICRO-STRUCTURE OF GAS SHALES AND ITS EFFECTS ON GAS STORAGE AND PRODUCTION PERFORMANCE

A DISSERTATION

SUBMITTED TO THE GRADUATE FACULTY

in partial fulfillment of the requirements for the

Degree of

DOCTOR OF PHILOSOPHY

By

RAYMOND J. AMBROSE
Norman, Oklahoma
2011

MICRO-STRUCTURE OF GAS SHALES AND ITS EFFECTS ON GAS STORAGE AND PRODUCTION PERFORMANCE

A DISSERTATION APPROVED FOR THE
MEWBOURNE SCHOOL OF PETROLEUM AND GEOLOGICAL ENGINEERING

BY

_____
Dr.Yucel Akkutlu, Chair

_____
Dr. Carl Sondergeld

_____
Dr. Jeffrey G. Callard

_____
Dr. Deepak Devegowda

_____
Dr. R. Douglas Elmore

DEDICATION

This work is dedicated to my wife and children. They have been by my side and behind me throughout my time in working on this material. Without them this would not have materialized. They are without a doubt the inspiration for me. I cannot put into words how much they mean to me. I love you all, Dawn, Joseph and Marlowe.

ACKNOWLEDGEMENTS

I would like to give my sincere thanks and gratitude to Dr. Yucel Akkutlu. Without his guidance and perseverance much of this work would not have been done. We have known each other a long time, all the way back to the end of my undergrad days and the start of his graduate work at the University of Southern California. I really enjoyed all of the work that we have done together.

I also want to thank Dr. Carl Sondergeld, who has pushed me to improve myself and to ask deeper, although often more fundamental questions. His guidance has been a main reason for this work. Additionally, I thank Dr. Chandra Rai for giving me the opportunity to continue my study that had begun at The University of Southern California. Furthermore, I want to thank Dr. Iraj Ershaghi for telling me that I needed to pursue further education and his wisdom during my academic career.

In addition I want to thank Dr. Mark Curtis, Dr. Chris Clarkson, and Chad Hartman. I thank Mark for his knowledge and wisdom in regards to microscopy. I thank Chris for his insights and support. I thank Chad for his wisdom and knowledge of gas storage in shale. Also, Jerry Youngblood and Rod Adams at Devon Energy for their wisdom and open minds in regards to shale research. This research would not be where it is today without their knowledge and expertise.

Finally, I would like to thank Gary Stowe for his assistance in getting this research off the ground. Also thanks to the people at Devon Energy for giving me this opportunity, specifically, Jeff Hall and Brett Jameson. Thank you for letting me help discover some new insights.

TABLE OF CONTENTS

LIST OF TABLES

LIST OF FIGURES

ABSTRACT

This dissertation includes discussions on three fundamental topics that are relevant to gas shale reservoir characterization and engineering. First, pore structure of organic-rich gas shale samples are investigated at the micro- and nano-scales. Second, the effect of gas adsorption phenomenon in small organic pores is discussed in relation to gas storage for both single- and multi-component fluids. Finally, a macroscopic investigation of shale gas production performance is performed. New equations provide the foundation for new analytical and experimental work in relation to gas in-place and production performance predictions.

Micro- and nano-scale visualization and analysis using microscopy is a novel approach to characterize industrial and technological materials structures. The same approach has recently become a focus of much research for the petrophysics of gas shales. The ability to directly investigate the shale pore structure and mineral diversity has given new and unforeseen insights into how gas is stored and transported. The results of this research and new insights have fostered new areas of investigation that are in their infancy stage. One major outcome of the investigation using the microscopy is that in most shales there appears to be a primary system of pores for the storage and transport of gas, rather than separate area of storage for sorbed and free phases. This simple observation has yielded a new set of equations which led to a fundamental-level correction to the previously applied method of determining the free and total gas storage in shale.

Gas storage is the foundation of transport measurement and gas reserves determination. In this dissertation a new method for determining gas storage in rocks with adsorbed gas is proposed. This methodology is first presented as a single component model, and then it is extended to a multi-component case. Additionally, the multi-component gas storage calculations are shown using two different sorption models, including one that is thermodynamically consistent.

Additionally, in this dissertation, performance prediction of multi-fractured horizontal wells is discussed. Horizontal well performance is tied to production logs with additional information from an image log study. This methodology helps to explain the performance seen in shale gas wells and gives new insights into performance prediction. The approach is later extended to give a workflow for shale gas field development. Using this approach, optimization can be performed on various economic parameters. The outcome of such optimization would be the lateral length of the horizontal well and the number of fracture stages.

CHAPTER I

Natural gas production from organic rich shales makes up an ever increasing percentage of total gas production in North America. This is a response to ever increasing demand to natural gas and lack of new conventional natural gas resources. Historically, shale has been considered a source rock for conventional oil and gas accumulations. However, beginning in the mid 1970's research and development into production from source rock began in earnest. The U.S. Department of Energy (DOE) and the Gas Research Institute (GRI) developed a set of tools and technologies to exploit the shallow Devonian shales in the Eastern US. Later, in the 1980's and 90's, Mitchell Energy and Development Corporation began to develop the Barnett shale in the Fort Worth Basin. With the commercialization of new technologies such as horizontal wells and multi-stage slick-water hydraulic fracturing, deeper shales such as the Barnett were proved to be commercially productive (King, 2010). From 2007 to 2010, US yearly production of natural gas from shales increased from 1.29 Tcf (trillion cubic feet) to over 4.8 Tcf, an increase of more than 370%. In addition, recent studies have put technically recoverable reserves at 862 Tcf in North America, and 5,760 Tcf throughout the world (EIA, 2011). During this time period, new insights have been gained and a few new findings reported in the literature about organic-rich shales, although in many aspects of exploration and production, gas shale has remained a mystery.

Understanding mineral content of the matrix and the pore structure is critical to determine how fluids are stored and transport takes place in the porous medium because the size and shape of the pores can give insights. The size of the pores is often

determined by the particles or grains that make up a porous medium. In shale, the grain size is typically less than 39 microns according to the Udden-Wentworth scale (Wentworth, 1922). At these small grain sizes, the pores would be expected to be much smaller. Additionally, because of these small grain sizes, shales are usually associated with clays. However, it is the particle size that usually assists in classifying rocks as shale. Grain sizes, in most organic shale are typically five microns or less (Sondergeld *et al.*, 2010a). Organic shale systems are similar to conventional gas reservoirs, in that they are porous sedimentary rocks that contain hydrocarbons. They have been given the term unconventional for a few different reasons; 1) as stated earlier, the grain sizes are smaller; 2) they often contain hydrocarbon in an adsorbed state (Wang and Reed, 2009; Ambrose *et al.*, 2010; Sondergeld *et al.*, 2010a); and 3) they are often the source of hydrocarbon generation. In being the source of hydrocarbon generation, the porosity system is often not formed in a conventional way. That is in conventional systems, the porosity system is a function of environment of deposition and the formation of secondary porosity. Additionally, in conventional systems the hydrocarbon within the porosity system is a function of a displacement process which is usually a function of density differences between hydrocarbon and water, and surface interactions, i.e. capillary pressure forces.

Investigating visually these small dimensions necessitates the use of microscopy. The most common microscopic tool for use at these resolutions is the Scanning Electron Microscope (SEM). Commercially available SEM's now have resolutions as low as 1 nm or less (FEI, 2009). Using these types of tools in order to investigate and characterize the pore structure of organic shale has become increasingly more popular in recent years.

With this new technology researchers are beginning to discover the unique roll the organic matter, usually kerogen or pyrobitumen, plays in these shales. (Wang and Reed, 2009; Loucks *et al.*, 2009; Moncrieff, 2009; Sondergeld *et al.*, 2010a; Ambrose *et al.*, 2010; Schieber, 2010; Passey *et al.*, 2010; and Curtis *et al.*, 2010). In this dissertation, tools such as SEM, Transmission Scanning Electron Microscopy (STEM) and Elemental Dispersive Spectroscopy (EDS) are used to assist in the characterization of the micro- and nano-pores.

The characterization of shale gas systems at the micro- and nano-scale dimensions has given many new insights into how these systems store and produce gas. In this study it is found that the location and size of the pore system within these reservoirs affects how the gas is stored. Additionally, the shape and structure contributes to the geomechanical aspects of the pore system. Other items that are a function of the pore structure and connectivity is the tortuosity and ultimately permeability and diffusivity of the matrix system. These characteristics have an effect on the micro-flow properties of the system, but ultimately have an effect on the macro-flow properties of the system, too.

This dissertation consists of seven chapters. Chapter 1 contains an introduction and literature review. Chapter 2 gives a foundational understanding to SEM, STEM and EDS technologies and their role in the characterization of the micro- and nano- structures that have been investigated within shales. Chapter 3 discusses gas adsorption in porous media and its role in organic shales. Chapter 4 focuses upon a new methodology for determining gas-in-place in shales utilizing a single-component model. Chapter 5 extends the single-component model to multiple-components and proposes a

thermodynamically consistent methodology for the gas in-place calculations. Chapter 6 looks into reservoir performance from the macro-view at the horizontal-well level. Finally chapter 7includes conclusions and recommendations for continued research.

1.1 Literature Review of Microstructure of Shale

The microstructure of shale is important to begin characterizing the geological system that contains the reservoir fluids; in essence, it is the basis for reservoir characterization. Characterization typically, starts at the pore-level, and then it is upscaled to the reservoir level through core-size correlation. From there the desire is to correlate to log-scale and ultimately to seismic resolution, however it must be stressed that it all starts at the pore level. Due to the scale differences, the research is still far from achieving pore to seismic scale characterization. Additionally, until recently only indirect measurements have been used to characterize the microstructure of shales (Sondergeld *et al.*, 2010b).

Shale microstructure investigation has only recently started to become a research topic, primarily for two reasons. First, shales were never classified as a source of economic investment until recently. Second, it is only recently that the application of the proper tools and measurements required to investigate the pore structure of shales have been used.

The first known application in to the investigation of microstructure of shales was performed by Schettler (Schettler *et al.*, 1989; Schettler and Parmely, 1991) on Devonian shales. Schettler used the Brunauer-Emmett-Teller (BET) method (Brunauer *et al.*, 1938) along with pore-filling experiments. In this work, the BET method was utilized to

measure the surface area of the system and relate it to the pore volume. Since the pore volume was small and the surface area was large, the effective pore sizes must also be small due to the ratio of surface area to pore volume relationship. The pore-filling experiments utilized the Kelvin equation (Dollimore and Heal, 1964) and gave pore size as a function of pore radius. The Kelvin equation accounts for the multi-layer adsorption thickness proposed earlier by BET, and describes the change in vapor pressure due to a curved liquid/vapor interface (meniscus) with radius *r*. The equation is used to determine pore size distribution of a porous medium using adsorption porosimetry. In this work, it was used to determine the mean pore diameter for Devonian shale. Schettler found the pore sizes ranged from 3.4 to 5.5 nm. However, their shape and connectivity were not determined.

Later, Bustin *et al.*, (2008), discussed multiple possible methods for determining the pore size distribution within shales. In this work, it was suggested that nuclear magnetic resonance (NMR), small angle neutron scattering (SANS), small angle x-ray scattering (SAXS), and adsorption porosimetry were promising methods. However, as Bustin suggested, the adsorption measurements must be done on dry samples due to very low vacuum pressures needed for the experiments. For shales, performing measurements on dry samples is problematic because removing the water held in the shale by the clays and high capillary forces changes the pore size distribution. Hence, the act of measurement affects the result of the measurement. In the case of SAXS and SANS, these measurements are costly and experimentally challenging.

Scanning electron microscopy has been utilized to determine pore size and shape in reservoir rocks for many years. However, it has been historically problematic within shale and mudrocks because it was difficult to determine what exactly was a pore and what was a function of the sample preparation process (Loucks *et al.*, 2009). Historically, in order to perform sample preparation, samples were ground with increasingly finer grit to create a smooth surface. **Fig 1a** shows a typical SEM image (from Slatt *et al.*, 2008) a shale sample. In this picture it is difficult to determine what constitutes porosity and what is a function of the mechanical damage of the sample preparation process. The mechanical damage is due to differences in the composition of the shale at the measurement scale (heterogeneity) and often makes interpretation difficult if not impossible. **Fig 1b.** shows an ion-beam milled sample. The sample preparation will be discussed more in Chapter 2 in this dissertation. Loucks *et al.* (2009) determined that by milling the sample with an Argon ion mill a smooth surface can be produced as shown in **Fig 1b**.

Ion-beam milling coupled with SEM has previously been used to determine pore structures of manufactured materials, such as catalysts including their porosity, pore surface area, and tortuosity (Smith *et al.*, 2009). This is a very similar path that adsorption porosimetry techniques have taken. Both techniques were used for manufactured materials first, and then the methods were adapted to natural materials. In the oil and gas sector, these materials are reservoir rocks. This initial technique has brought about a sea-change in how shales are imaged in an SEM. Much of the recent

research and the research focus in this dissertation uses SEM technology coupled with focused ion-beam milling.

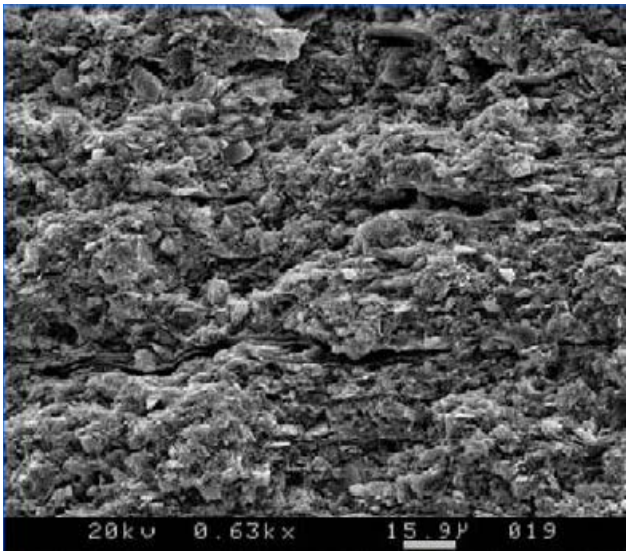

(a)

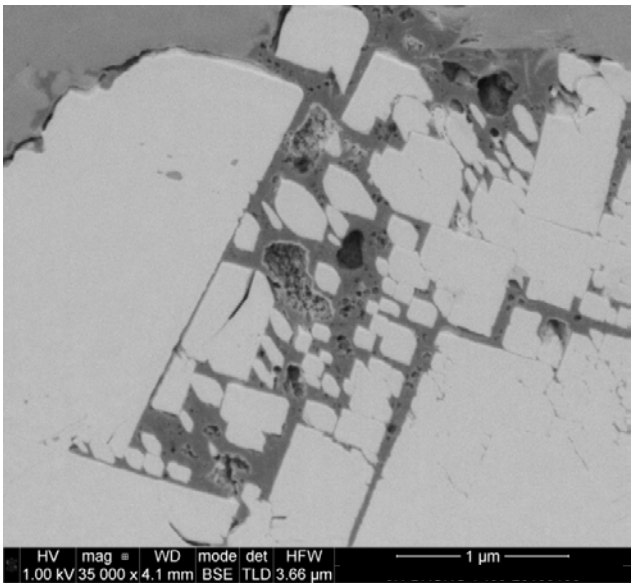

(b)

Fig. 1 (a) - Mechanically prepared SEM sample from Slatt *et al.*, 2008. The porosity system is difficult to interpret in this sample. In (b) the sample surface is prepared with a focused ion-beam mill. The porosity, shown in black, is clearly distinguishable from the matrix.

1.2 Literature Review of Gas Adsorption and Gas-in-place Measurements

Gas in place determination in shale has been discussed with increased frequency due to the economic development of these reservoirs. Methods to quantify the gas-in-place were developed specifically for coals, tight rocks and other low-permeability formations (Luffel and Guidry, 1992; Luffel *et al.*, 1993; Mavor *et al.*, 1996; and GRI, 1997). Gas is primarily stored in four thermodynamic states within the shale. It is stored as a free gas in the available pore space. It is also stored on the internal surfaces of the shale matrix; this is what is known as adsorbed gas. Also, it is absorbed (or dissolved) in liquid hydrocarbons, if the latter is present in the pore space. Finally, it is stored as dissolved gas in the water. Since the origination of shale gas petrophysical evaluation is heavily based upon methods originally developed for coals, it is most often reported on an scf/ton basis.

It was first discussed in literature by Schettler (Schettler *et al.*, 1989; Schettler and Parmely, 1991). In these works free gas, an adsorbed and a dissolved phase was introduced. Gas uptake experiments were performed where methane gas was allowed to re-penetrate a sample to obtain a total storability value. However, no attempt was made to separate the storage of gas into its main components.

Later, Cui *et al.* (2009) discussed the effect of the sorbed phase on porosity. The motivation for this work was to determine the change in porosity of a system as a function of pressure and its effect on the permeability of the system. Much of the work in this dissertation is an extension of this work.

1.3 Literature Review of Shale Gas Performance Prediction

Shale gas well performance at a macro-level has been adapted from earlier techniques. The adaptations have been grouped into four general categories (Clarkson and Beierle, 2011). These categories as described by Clarkson are: 1) empirical methods; 2) analytical and numerical simulation; 3) straight-line methods; and 4) type-curve methods. Straight-line methods are often a subset of analytical methods and type-curve methods are often a combination of empirical and analytical methods.

Empirical methods were developed first. The seminal work of Arps (1945), which is still the standard today, showed that past production can be used to forecast future performance. A few of the main advantages with this empirical technique is that the decline profile can be forecasted by a constant *b*-value. However, two main assumptions must be met: 1) current operating conditions are constant and will continue into the future; and 2) wells are producing during boundary-dominated flow (BDF). This work was extended by Ilk *et al.* (2008) and Valko (2009). They introduced the Power-Law or Stretch Exponential model, which are virtually the same mathematically. In this model, the *b* factor as defined by Arps changes throughout time. The motivation for this work is that transients in tight-gas wells last for very long times and it is unknown when boundary dominated flow will dominate the performance, if it dominates at all. Therefore, adjusting the *b*-factor throughout time compensates for the uncertainty.

Analytical and numerical methods utilize governing equations to predict the well performance. Often, the production history is used to match reservoir parameters and inputs in order to calibrate or "history-match" the model. The advantages of these types

of models is that different operating scenarios can be tested and investigated, including different operating conditions and multiple well performance. The disadvantage of this method, specifically in shale wells is that proper reservoir characterization must be used which is often difficult due to the scaling and heterogeneity issues associated with tight and shale-gas wells (Sondergeld *et al.*, 2010b).

Straight-line methods are a subset or extension of the analytical methods. These methods are mainly pressure-transient analog methods. The main goal in these methods is to identify a flow-regime by obtaining a "straight-line" on a specialty plot. This approach for gas wells has been utilized by Mattar and McNeil, (1997), Wattenbarger *et al.* (1998), Agarwal *et al.* (1999), Poe *et al.* (1999), Mattar and Anderson (2005), and Cheng *et al.* (2009). Mattar and McNeil utilize a curve where flowing pressure is plotted against cumulative production in a straight-line to forecast estimated ultimate recovery (EUR). This method is also called the flowing-material-balance method (FMB). The FMB method has a limitation because the flowrate must be constant. Wattenbarger, through several iterations, plots pseudo-pressure normalized reciprocal rate against the square-root of time, also called the linear-flow analysis plot (LFA), to forecast future production. A straight line on this plot that passes through the origin gives the product of the area of the fracture open to linear flow and the permeability of the matrix ($Ak^{1/2}$). This work has been extended by Ibrahim and Wattenbarger (2006) where a correction for drawdown error was applied. Later, Bello and Wattenbarger (2010) extended this work further to incorporate multi-stage hydraulically fracture horizontal wells with the addition of skin. In all of the linear flow models, the utility of determining contacted gas-in-place

can be performed. Mattar and Anderson (2005) extend the FMB work to a dynamic material balance plot which adjusts for a variable flowrate. Cheng *et al.* (2009) utilized a plot of the natural log (ln) of the axis of the major and minor elliptical directions (A + B) against the change in pseudopressure (Δp_p). A straight line on this plot will have a slope that indicates the permeability of the system and an x-intercept that indicates the fracture half-length (x_f).

In the next chapter new findings showing the intricacies of shale, are discussed in regards to the microstructure and pore systems in these types of reservoirs. In chapter 3 the microstructure and pore system work is extended to explore gas storage in shale. This gas storage work is then extended to new methodologies for determining the gas-in-place in these systems. Finally, a macro-scale view of well performance is discussed where image logs, micro-seismic, production logs and well performance is tied together.

CHAPTER II

MICRO- AND NANO-STRUCTURES OF GAS SHALES

In this chapter the shale gas pore size and structure is discussed. Next, different methods of measurements and their ability to determine the size and structure of pores in gas shale will be evaluated. The methods that are evaluated in this thesis are: mercury injection capillary pressure (MICP), low-temperature gas adsorption porosimetry, focused ion-beam/ scanning electron microscopy (FIB/SEM), scanning transmission electron microscopy (STEM), and nuclear magnetic resonance (NMR), spectrometry. Low pressure gas pycnometry (or briefly helium porosity) is not discussed here. A separate chapter specific to gas adsorption techniques for pore characterization follows. Examples of these measurement types and discussions about correlations between them will be shown along with discussion of the advantages and disadvantages of each. Following, the effects of pore size and structure on reservoir performance is discussed. Finally, recommendations for a complete suite of measurements and measurement workflow that complement each other will be made at the end of this chapter.

Reservoir characterization begins at the pore level. Until recently shale gas reservoir pore structure was largely a mystery. Indirect laboratory measurements such as MICP and NMR were performed in order to gain some sort of understanding of the microstructure. These techniques were used both qualitatively and quantitatively to determine the sizes from an inferred shape of the pore system. Kale *et al.* (2010) utilized MICP in order to classify three different facies types and hence pore throat sizes in the Barnett shale. However, until the works by Wang and Reed (2009), Chalmers *et al.*

(2009) , Loucks *et al.* (2009) and Sondergeld *et al.* (2010a) using FIB/SEM, no direct evidence of the pore structure existed. Bustin *et al.* (2008) discussed most of the possible methods that could be used in order to classify pore size and structure, with the exception of NMR. **Fig. 2,** adapted from Bustin *et al.* (2009), illustrates a good synopsis of the measurements that can be used to investigate pore structure at varying length scales. In this figure, two main categories of microstructure measurement methods are shown. First, there are radiation methods which include optical microscopes, such as SEM, TEM, STEM, and small-angle neutron and x-ray scattering (SANS/SAXS). The second measurement type classification is that of penetrating fluids. These types of methods involve the introduction of a fluid and either a mass, volume, or pressure measurement (or combination thereof) to indirectly measure the pore size. However, when using penetrating type measurements, the pore size and shapes can only be inferred. MICP, helium porosimetry, and adsorption porosimetry using nitrogen and carbon dioxide are widely used methods that belong to this second group.

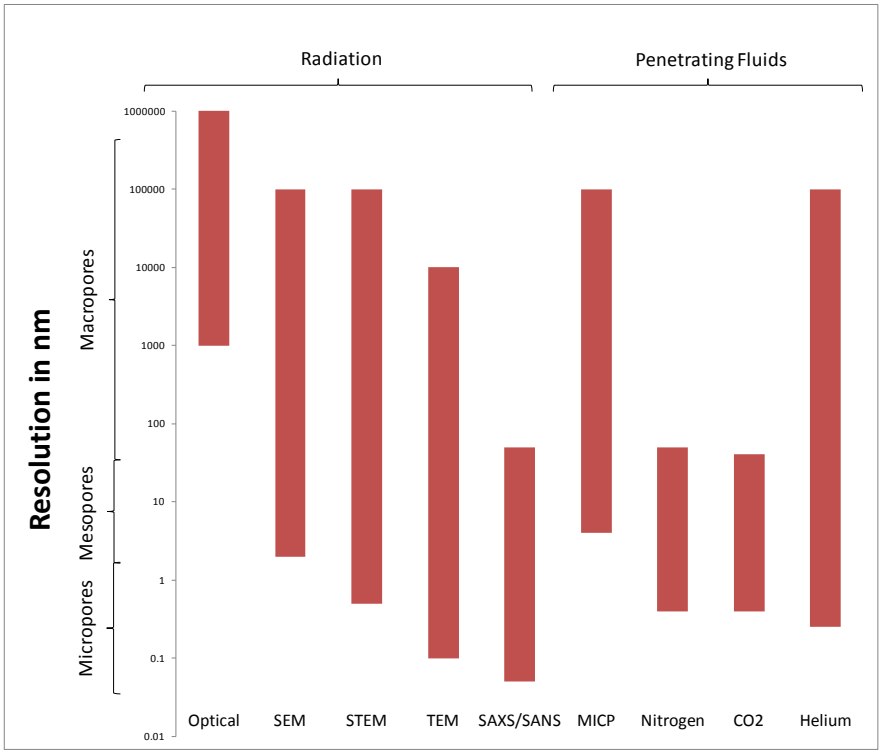

Fig. 2 – This figure shows approximate length scale of pore structure measurements. Both direct radiation and indirect penetrating fluid type measurements are shown. From Bustin *et al.* (2009).

One major concern when dealing with pore structures of shale is that the pore systems of shale are not static. Hartman *et al.*, (2008) and Passey *et al.*, (2010), noted that in bulk measurements there was a marked difference in the porosity of preserved and unpreserved samples. Bustin *et al.* (2008) noted that using certain measurement techniques requires high vacuum pressures hence dry samples. Notably, nitrogen and CO_2 adsorption, do not measure in-situ pore structure. This raises the question, "Is there a change in pore structure when samples are not preserved?" Wang and Reed (2009 - presentation only) noted that these systems are below the critical water saturations. Hartman *et al.*, (2008) suggested that these cores can desiccate or take up water depending upon the humidity that the rocks are exposed to. Dynamic nature of the pore

system and its sensitivity to the environment during the measurements will be investigated and further discussed in Chapter 3.

Another important issue when measuring shale pore structure is the measurement technique that is employed. This must be kept in mind when making bulk measurements such as adsorption, helium grain density, MICP, or NMR. Additionally, measurement conditions and core handling must be considered when making interpretations of the visual microscopic measurements. Ideally, in the future there would be one set of measurements following a carefully developed protocol that takes into account the above-mentioned concerns for shale pore structure, however at this point in time it is not technically feasible.

2.1 Measurement Methods and Application for Shale Pore Characterization

There are multiple measurement methods that can be used to assist in determining the pore structure associated with shales. Measurement methods that will be discussed here include MICP, NMR, FIB/SEM, STEM, and adsorption.

Mercury injection capillary pressure (MICP) introduced by Ritter and Drake (1945) has been used to model pore size distributions. MICP measurements determine pore throats, not bodies. Their model utilizes a bundle of capillary tubes method. **Eq. 1** shows the density function ($\alpha(D_e)$) of pore throat size distribution.

$$\alpha(D_e) = \frac{P_c}{D_e} \frac{d(V_T - V_{De})}{dP_c} \quad \textbf{(1)}$$

In this equation D_e is the diameter of the pore throat, P_c is the capillary pressure, V_T is the total pore volume and V_{De} is the volume of pores with entry diameters less than D_e. However, this model is based on a bundle of capillary tubes model and gives information in regards to the sizes of the pore throats, rather than the pore itself (Dullien, 1992). Dullien and Dhawan (1975) emphasized that this technique should be used in conjunction with visual methods. High pressure MICP can determine pore throats down to the order of 3 nm (Kale *et al.*, 2010). The recommendation of combining MICP with visual analysis is concluded in this work. An example of MICP results from Kale *et al.*, (2010), normalized for pore volume is shown in **Fig. 3**. In this figure, three different curve shapes are shown. Kale noted that for pore throats that are type 'A', 50-65% of the pore volume could be accessed by mercury, in type 'B', 65-75%, and 25-50% for type 'C'. This equates to 35-50% of the porosity in type 'A' rocks is accessed by pores than 3nm,

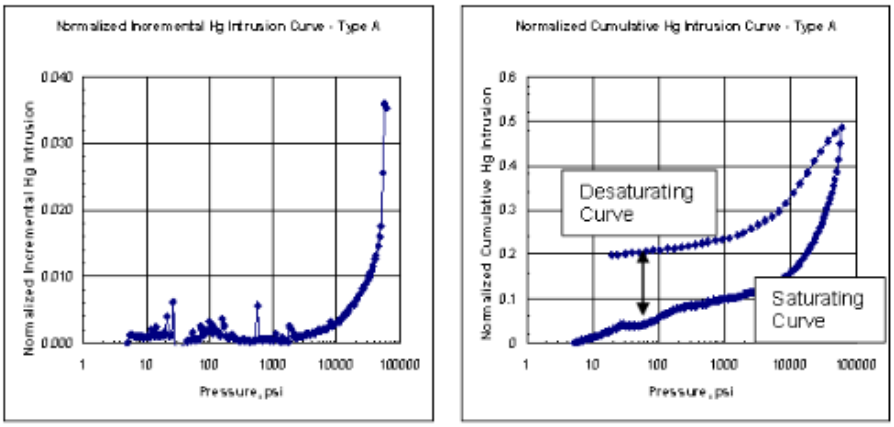

(A)

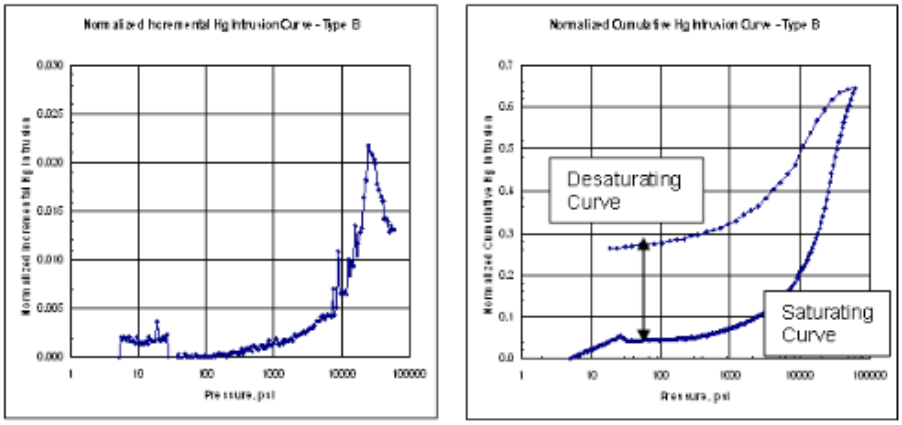

(B)

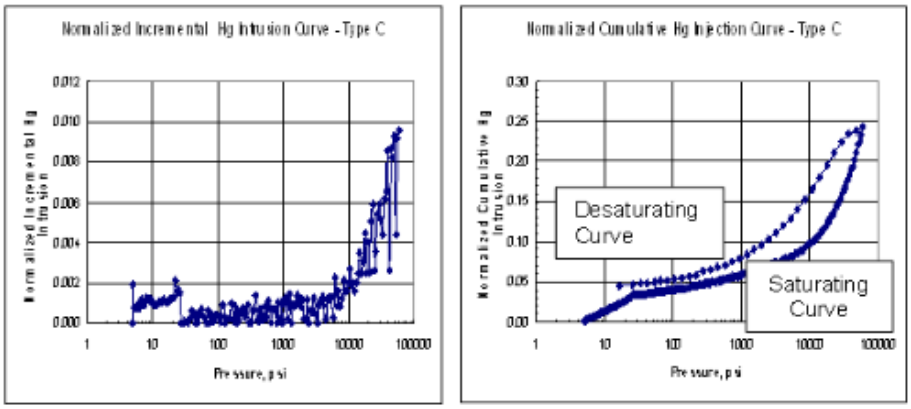

(C)

Fig. 3 - Mercury injection capillary pressure (MICP) curves from Kale *et al.*, (2010). Data shows three different pore groups are determined using the peaks in the pressure curve. Note the percentage of intrusion at 60,000 psi. Type 'A' shows 50% intrusion, type 'B' 65 % and type 'C' of 25%. This correlates to porosity accessed by pore throats larger than 3 nm.

23-35% for type 'B' and 50-75% for type 'C'. **Fig. 4** is an illustration of this drawback pointed out by Dullien and Dhawan (1975). In this illustration, due to the measurement being dependent upon the effective pore throat diameter (D_e) rather than the pore size, limited information can be inferred. In this model, the shapes of the pore throats are also assumed to be cylinders.

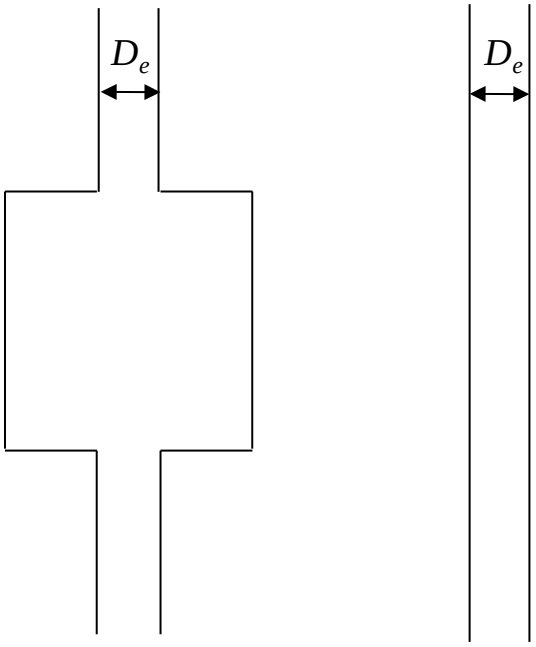

Fig. 4 - Discrepancy associated with pore volume estimation using a bundle of capillary tubes model. On the left the pore volume estimated using mercury intrusion will be much larger than the pore volume on the right, even though the pressures will be the same because of similar D_e's.

NMR techniques, on the other hand, are based on the measurement of the pore bodies, not throats. Measurement on core samples have been reported on by Howard (1991), Martinez and Davis (2000), and Dastidar (2007). NMR measurements are based relaxation times of proton spins in magnetic fields applied to a system. Protons are typically associated with the hydrogen atoms within the fluids. There are two types of relaxation times that are measured. T_1 relaxation time is caused by energy-loss to the

environment and longitudinal spin of the proton in the hydrogen atom. T_2 relaxation time is caused by an increase in entropy and a transverse spin of the hydrogen atom. The T_2 signal decay is due to the relaxation caused by spin-spin interactions (Xu and Davis, 1999). At the fast diffusion limit, the T_2 time is proportional to the pore body radius. **Eq. 2a**, shows the general form of relating T_2 relaxation times to pore throat radii. In this equation T_2 is the relaxation time in μs, ρ is the surface relaxivity constant. This constant can range between 0.00037 and 0.046 μm/ms for sands (Dunn *et al.* 2002). *S* is the surface area and *V* is the volume. For a sphere *S/V* reduces to *3/r*, where *r* is the radius of the sphere, in a cylinder, it is 2/*r*. This is shown in **Eq. 2b** and **Eq. 2c**.

$$\frac{1}{T_2} \cong \rho \frac{S}{V} \quad \textbf{(2a)}$$

$$\frac{1}{T_2} \cong \rho \frac{3}{r} \quad \textbf{(2b)}$$

$$\frac{1}{T_2} \cong \rho \frac{2}{r} \quad \textbf{(2c)}$$

The main unknown in this type of analysis for determining pore-structure is that one has to assume a pore shape to infer a pore size. Additionally, surface relaxivity constant needs to be determined for the analysis. **Fig. 5** is from Sondergeld *et al.* (2010a). It shows T_2 spectra of "as received" Barnett shale samples. Using a conservative surface

relaxivity constant of 0.05 μm/ms, pore bodies of these samples ranged from 5 nm to 150 nm.

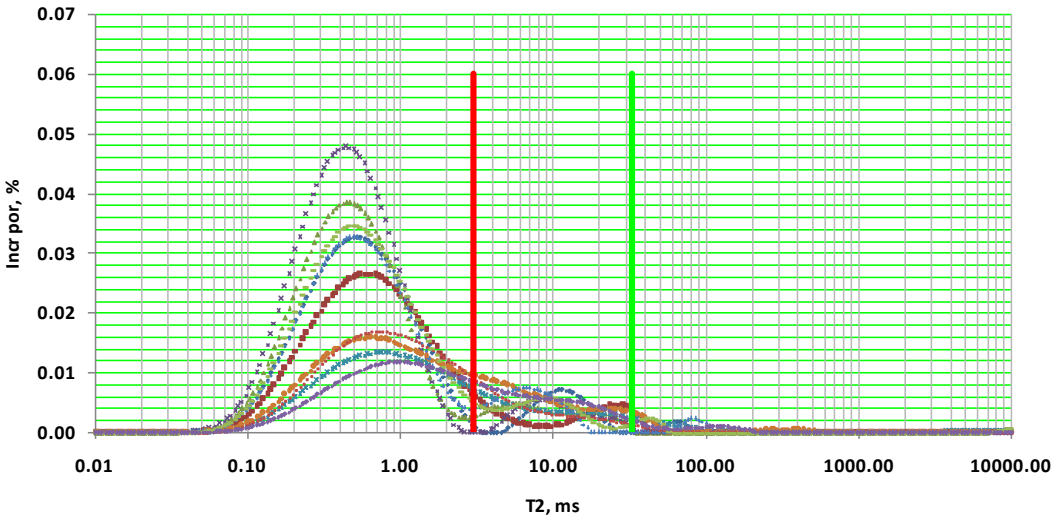

Fig. 5 - NMR T_2 spectra for an "as received" Barnett shale samples. The red line corresponds to clay bound water cutoff, while the green line corresponds to capillary bound water cutoff. These signals give indication of pore body size and porosity that is saturated by water. Sondergeld *et al.* (2010)

When we combine the pore throat information obtained from MICP and the pore body information inferred from NMR, the data suggests that pore throats are on the order of 1-10 nm and pore bodies are on the order of 5-150 nm. Based on the discussion by Dullien and Dhawan (1975), visual tools should thus be used to (1) confirm the sizes of the pores, and then (2) determine the morphology (or shape and structure) of the pore system to better understand and characterize how fluid is stored and flows in this type of porous media.

Keeping **Fig. 2** at the center of our discussions, visual tools that can provide additional insights into the morphology of the pore system are SEM and STEM. The

physics behind these measurement devices will not be discussed here, for reference the reader should consult the text "Scanning Electron Microscopy and X-Ray Microanalysis" by Goldstein at al. (2007). In these types of rocks, these tools can be used in conjunction with a focused-ion beam (FIB) to prepare a superior surface than one obtained by mechanical preparation, so that the pore system and the matrix can be differentiated in two-dimensional (2D) images. In addition, three-dimensional (3D) volumes can be generated without any difficulty. Recent investigations combines an FIB with an SEM, often called a dual-beam system or FIB-SEM. These tools are combined to provide 3D datasets to give additional insight into the pore connectivity of a system. A diagram showing 2D sectioning and 3D segmentation process is presented in **Fig. 6**.

In this dissertation the SEM images with some image interpretation and analysis utilizing Avizo Fire 6.2 ® software help build a complete picture of the pore systems within the Barnett and give a workflow for future shale pore structure analysis. Additionally, some of the issues with these types of measurements are discussed.

As shown in **Fig. 6**, high-quality 2D SEM images are taken on the order of 10 nm apart. In this figure, the ion beam and electron beam are shown meeting at the eucentric point. A platinum strip is laid down in order to provide a clean, consistent cutting surface. Additionally, a fiducial (fixed reference) point is used so that the ion beam can index where it is cutting the sample. Successive cuts and SEM images are taken providing the basic inputs of the 3D dataset. The images are then manipulated and analyzed in the Avizo Fire 6.2 ® software program. After rendering the 3D volume, a process called segmentation allows for data to be extracted from the images. Qualitative

data such as pore information related to morphology can be interpreted while quantitative information such as pore size and number can be determined during the analysis (Curtis *et al.*, 2010).

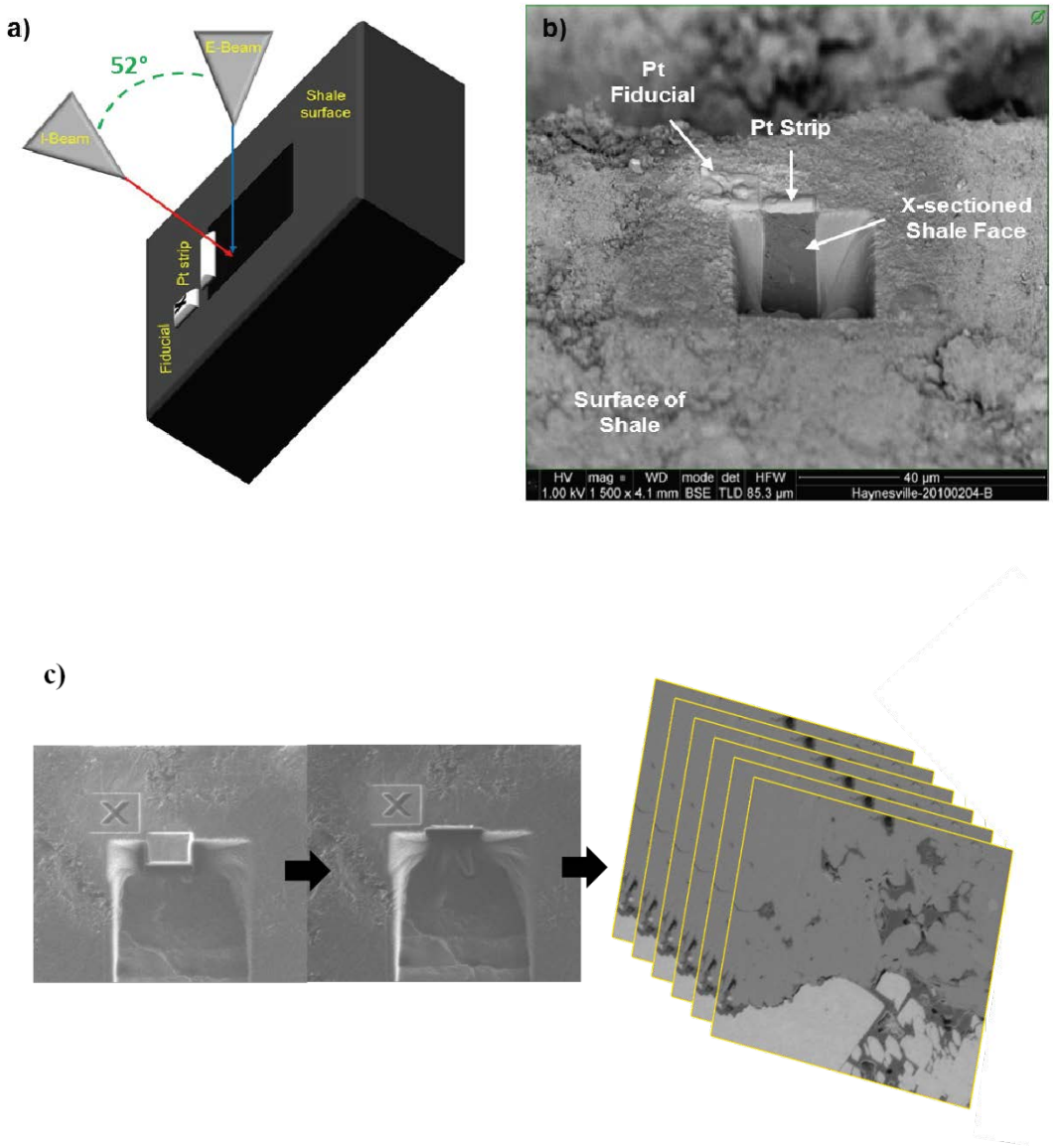

Fig. 6 - Adapted from Curtis *et al.* (2010). a) Shows a diagram of the ion-beam and e-beam used to prepare a smooth surface and create high quality SEM images. b) A back-scatted electron (BSE) image showing the prepared sample area. c) top down I-beam images illustrating the initial sample and the sample after approximately 400 successive slices and images are taken. These images are then rendered into a 3D volume in the Avizo Fire 6.2 ® program for qualitative and quantitative analysis.

A segmented volume of Barnett shale was analyzed for statistics of quantitative pore data including, number, size and surface area. The dataset was subsequently qualitatively assessed for pore connectivity and morphology. This dataset was from an area of the Barnett where the thermal maturity is quite high (R_o ~ 2.0%). A series of 500 images were obtained and a 3D volume was rendered. During rendering, image alignment must be performed due to the small perturbations that occur in between the successive SEM image acquisitions. Additionally, a Gaussian smoothing image filter is applied to the data. The filter takes data from the neighboring cells to improve image quality. The images have a pixel resolution of 2.5 nm in the *x* and *y* directions. When this data is combined to create a 3D dataset the voxel (a 3D pixel) resolution is 2.5 x 2.5 x 10 nm. When the Gaussian smoothing is also considered the real resolution is on the order of 5 nm in the *x* and *y* and 10 nm in the *z* directions.

Fig. 7 shows the 3D dataset. In this figure, a 256 color grayscale image, the pores can be seen as black, kerogen is dark gray, matrix is light gray and the lightest gray (nearly white) is determined to be pyrite. Gray scale thresholding allows the different constituents of the 3D volume to be analyzed. This is an interpretive analysis and the user has control over the values used for thresholding. An example of the thresholding used for kerogen and porosity is shown in **Fig. 8**. As can be seen in **Fig 8**, much of the porosity is associated with the kerogen. Consistently throughout all of the Barnett samples analyzed (more than 20) there appears to be a significant portion of the porosity associated with the kerogen, hence a "kerogen network". Earlier, Loucks *et al.* (2009) and Wang and Reed (2009) reached similar conclusions.

In this sample the kerogen network occupies 5.3% of the total imaged volume; visible pores take up 2.3% of that volume. If we assume all the pore space is in the kerogen, the kerogen porosity (defined as kerogen pore volume divided by kerogen bulk volume) is roughly determined as 43%. This porosity is believed to be low because image processing does not currently allow for repeated information in the 3rd dimension to be removed. Drawbacks such as these will be discussed at the end of the section. The location of the porosity as discussed in Chapters 3 through 5 of this dissertation has important ramifications to gas adsorption and ultimately to gas-in-place. The pyrite takes up about 17.5% of the total imaged volume. By taking all of the different pore bodies and converting them to an equivalent spherical radius, histograms of the pore radius, along with pore volume and equivalent spherical radius is shown in **Fig 9**. It can be clearly seen on these semi-log plots that the small pores with equivalent diameters less than 2nm do not contribute to the pore volume although they dominate the organic pore population. The larger size pores dominate the pore volume of the sample. Additionally displayed on this plot is the fractal dimension of the dataset. The red line represents a fractal dimension of the best imaged pores, the value of which is 1.8. The black line represents the fractal dimension of all the data, which is 2.1. These are very similar values to those determined by Curtis *et al.* (2010).

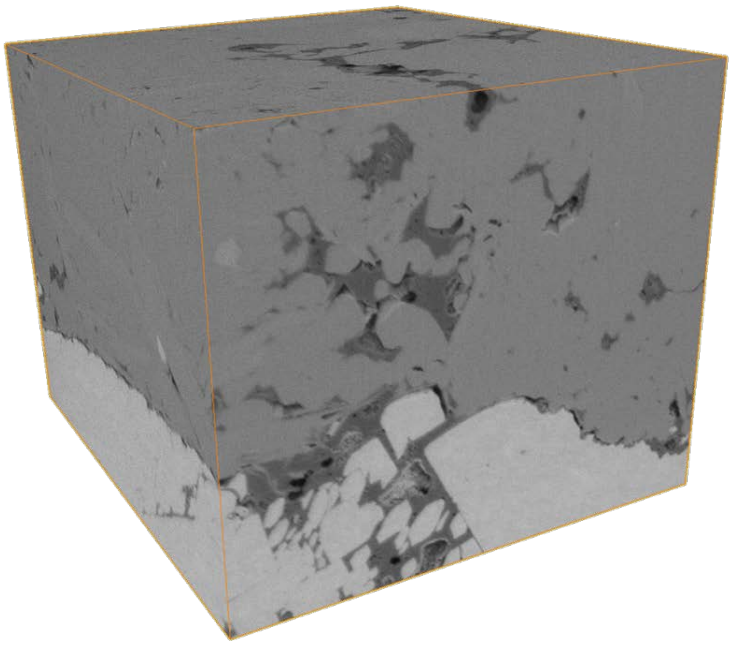

Fig. 7 - 3D rendered volume of a Barnett shale sample produced from 2D FIB/SEM slices. The sample dimensions are roughly 5 μm each side. The black represents pore, dark gray is kerogen; together they make up the kerogen network. Light gray is inorganic matrix and the almost white color is pyrite. The dimensions of each side of the cube are roughly 4 micron.

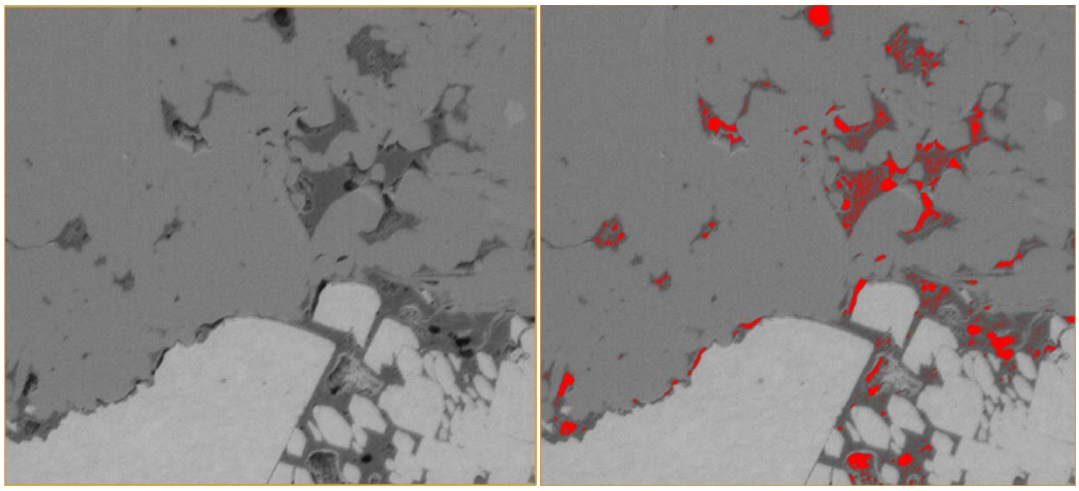

Fig. 8 – A 2D FIB/SEM slice showing the thresholding technique on grayscale interpreted as pore. In this sample the porosity from the SEM image analysis was determined to be 2.3%. This porosity is believed to be low due to repeated 3rd dimension data over multiple slices. The dimensions of the slices are roughly 5.12 micron by 5.12 micron.

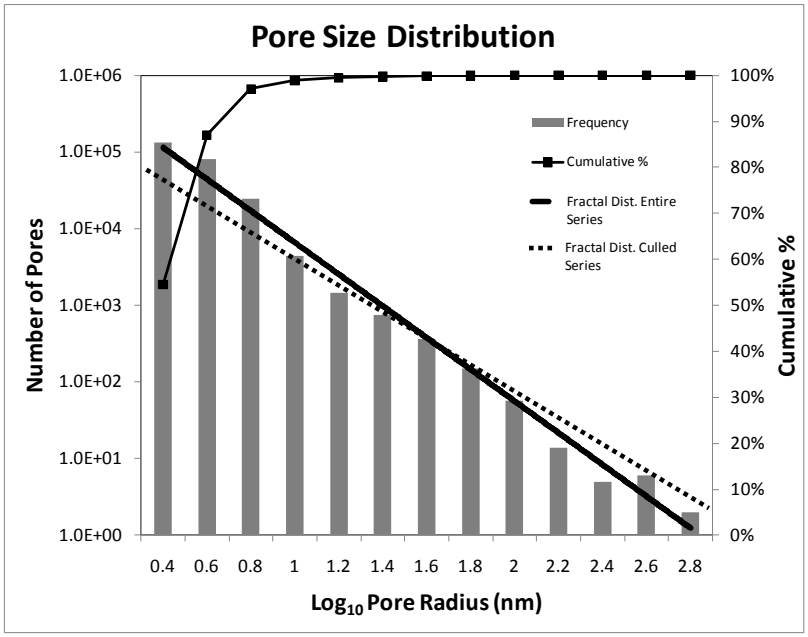

(a)

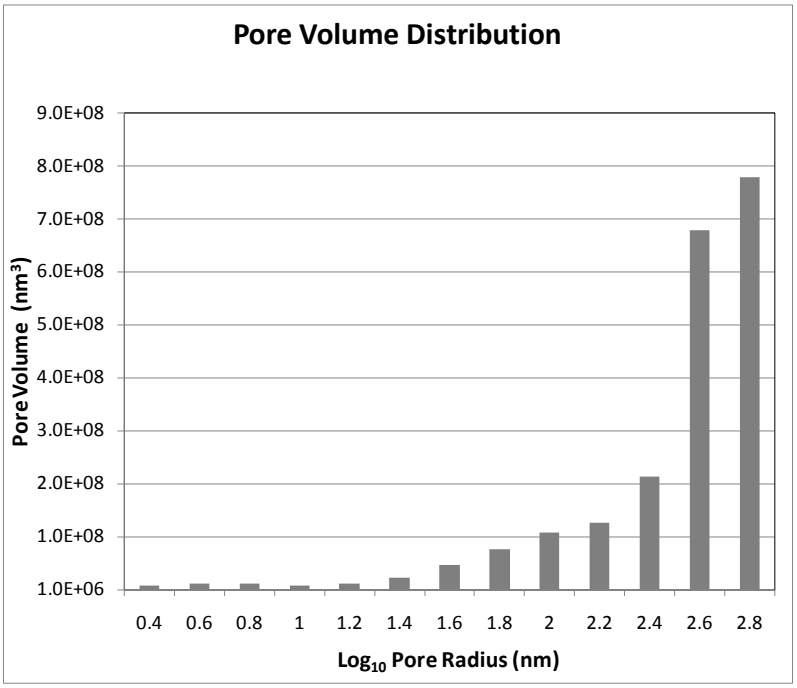

(b)

Fig. 9 - Pore volume and size distributions from 3D segmented SEM volume. (a) shows the numbers of pores discriminated by an equivalent spherical radius. The log scales represent the dimensionality of the pore system. A fractal distribution can be determined. The fractal dimension of the dashed line is 1.8, the black line is 2.1. (b) shows the actual pore volume distribution, as a function of equivalent spherical radius.

Connectivity can also be investigated from SEM data by combining those obtained from NMR and MICP. Since SEM measures pore bodies, in essence the data given in **Fig. 9** should mirror that of NMR given in **Fig. 5**. Since both pore bodies are on the same order, very close agreement is seen between the two data types, even though the samples are not the same and pore sizes from NMR need to be inferred. From MICP data showed in **Fig. 3**, the expected range of pore connectivity should be in the 10 nm range or lower. Looking at **Fig. 2** this is at the lower range of SEM capabilities. When segmenting images and creating 3D datasets in the Barnett, it is very easy to connect the kerogen networks across a sample. **Fig. 10a** shows the kerogen network of the sample in **Fig. 7**. It can be seen clearly in this figure that the kerogen network spans the sample. However, it is very difficult to connect all of the pores across the length of the sample. **Fig. 10b** shows the pores and their disconnected nature across the sample. There are a few main reasons for this. First, the disconnected pores in the image do not mean that the pores are physically disconnected; it means that the resolution of the equipment and the imaging techniques applied are not powerful enough to resolve the connectivity at that scale. Additionally, repeated information in the 3rd third dimension and the Gaussian filtering are the additional causes for the uncertainties associated with the pore connectivity. Gaussian digital filtering tends to smooth out the smallest features.

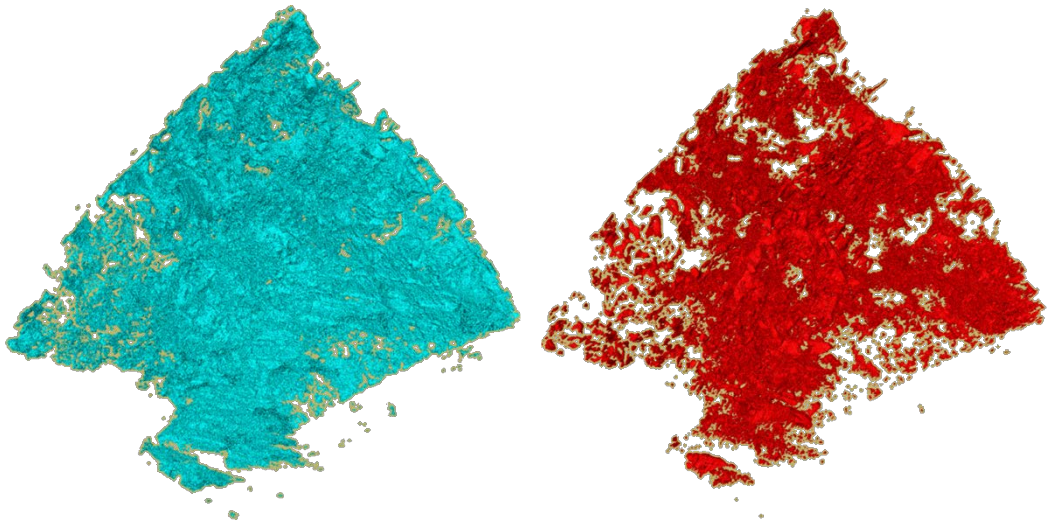

(a) **(b)**

Fig. 10 - Kerogen volume and pore volume segmentations. (a) segmentation of kerogen network consisting of both pores and kerogen, here connectivity is seen throughout. (b) segmentation of pores only showing very good connectivity across the sample. Unconnected pores can be also seen throughout

Fig. 11 shows two sequential SEM images, where data repeated in the 3rd dimension can clearly be seen. The porosity values determined from SEM data such as this will be artificially low. Curtis *et al.* (2010) addressed the artificially low porosity values obtained from 3D SEM methods. Additionally, the SEM was used in combination with MICP to assist in inferring connectivity. For this, mercury was injected into a sample up to a pressure of 60,000 psi. Then the sample was depressurized and sealed immediately in order to minimize the loss of mercury. This sample was then analyzed with the SEM. Due to the high levels of vacuum that the SEM runs at, direct evidence of mercury was not visualized.

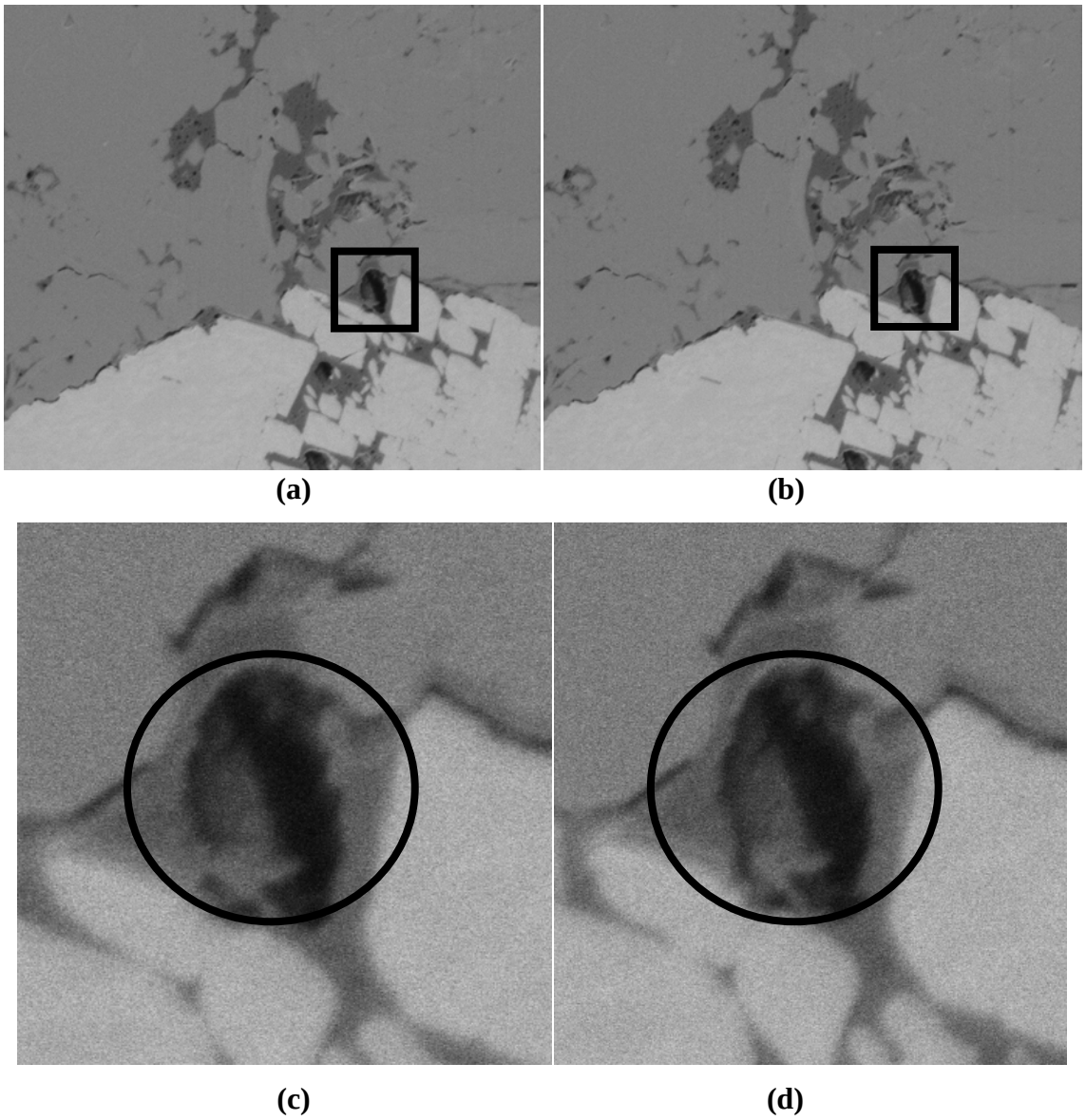

Fig. 11 - Successive SEM slices showing repeated data in the 3rd dimension. (a) is the first slice and (b) is the successive slice. Using gray scale thresholding information inside the pore is repeated across successive images. This is highlighted in (c) and (d), which are magnifications of the image in (a) and (b) respectively. Similar data is seen in images 10 slices later, indicating that in large pores, porosity is not being counted due to 3rd dimension data being repeated.

The reason that mercury is not visible on the surface is that the vapor pressure of mercury is higher than the vacuum pressure of the SEM. In order to overcome this challenge, the electron voltage of the machine was increased in order to increase the electron penetration. This enables information beneath the surface of the sample to be measured.

Later, the sample was analyzed via energy dispersive x-ray spectroscopy (EDS or EDX). EDS is a method that analyzes the energies of x-rays that are emitted from the electron level transition in the elements that are irradiated. EDS mapping allows correlation between gray scale and elements that make up the samples. **Fig. 12** is a set of SEM's that show the presence of mercury deeper in the sample. The first picture is a low voltage image (1.00 kV) that shows the surface, the second is a much higher voltage image (20.00 kV), that gives more information about what is beneath the surface. **Fig. 13** is an EDS map showing in fact that the bright spots are Hg (mercury).

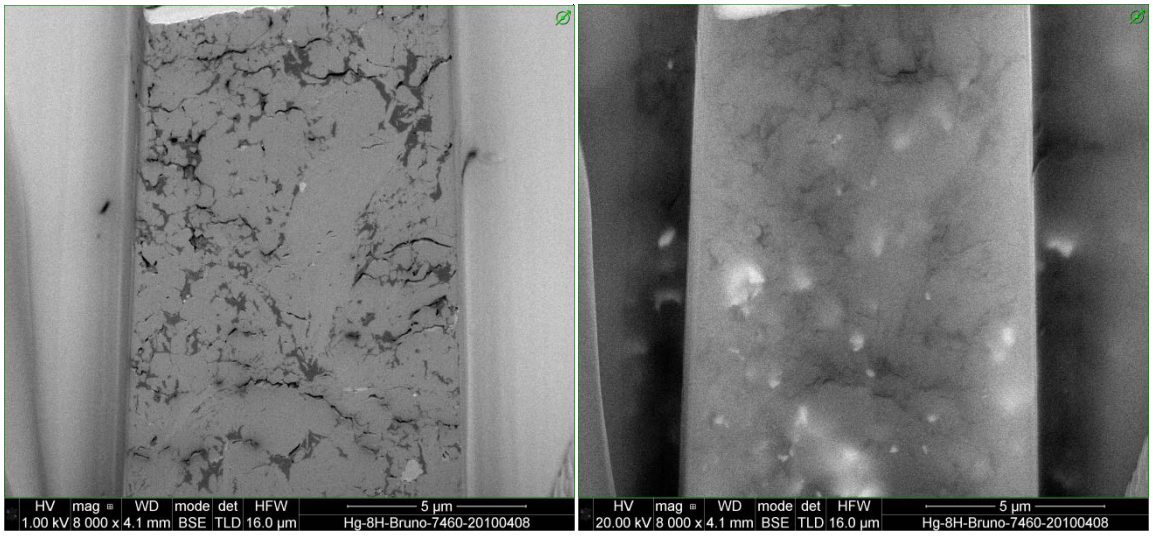

(a) **(b)**

Fig. 12 - SEM images taken at (a) 1.00 kV and (b) 20.00 kV of a sample injected with mercury. (a) shows surface features, as the electrons do not have the energy to penetrate the sample and return information. (b) shows features deeper in the sample due to higher kV electrons. The gray scale is a function of atomic z value. Due to the density of mercury being so great, mercury beneath the surface will show up as bright spots on the image.

Another method was also used to analyze pore connectivity at a level below the resolution of an SEM. Scanning Transmission Electron Microscopy (STEM) was utilized in order to increase the resolution images. According to **Fig. 2** STEM can resolve below 1nm. Sondergeld *et al.* (2010a) followed by Curtis *et al.* (2011) published some of the

first work of STEM imaging technology used on shale. **Fig. 14** taken from Curtis *et al.* (2011) gives a pictorial of the sample preparation required. STEM measurements are

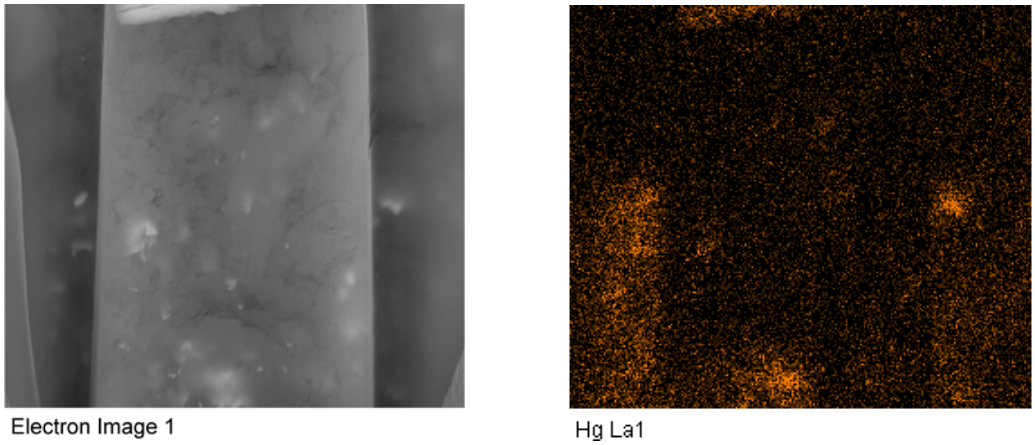

Fig. 13 - An EDS map of the sample shown in Fig. 12. The EDS highlights the presence of Hg in the sample. Hg is not normally present, however, was pumped into the sample using MICP. High voltage electrons (20-30kV) had to be used to penetrate the sample in order to "see" the presence of the mercury before it evaporated due to the high vacuum in the sample chamber.

different from SEM in that electrons are transmitted through the sample to detectors. Therefore a STEM sample must be extremely thin, on the order of 100 nm or less. The electron beam is then rastered across the sample, the electrons pass through to annular dark field (ADF), high-angle annular dark field (HAADF), and bright field (BF) detectors. ADF images of the sample are shown in **Fig. 15**. In these images, pore throats through the kerogen as small as 2 nm can be clearly seen. These sizes are on the same order as those inferred from MICP data of the sample shown in **Fig. 16**. An NMR of this sample was also performed and results are shown in **Fig. 17**. From the NMR utilizing **Eq. 2b** the pore body size is determined to be between 6 nm and 60 nm, depending upon a surface relaxivity (ρ) varying between 0.05 μm/ms and 0.005 μm/ms. Therefore the

data is consistent between all measurements, since this sample is from the same sample set that is in the images in **Fig. 8** through **Fig. 13**.

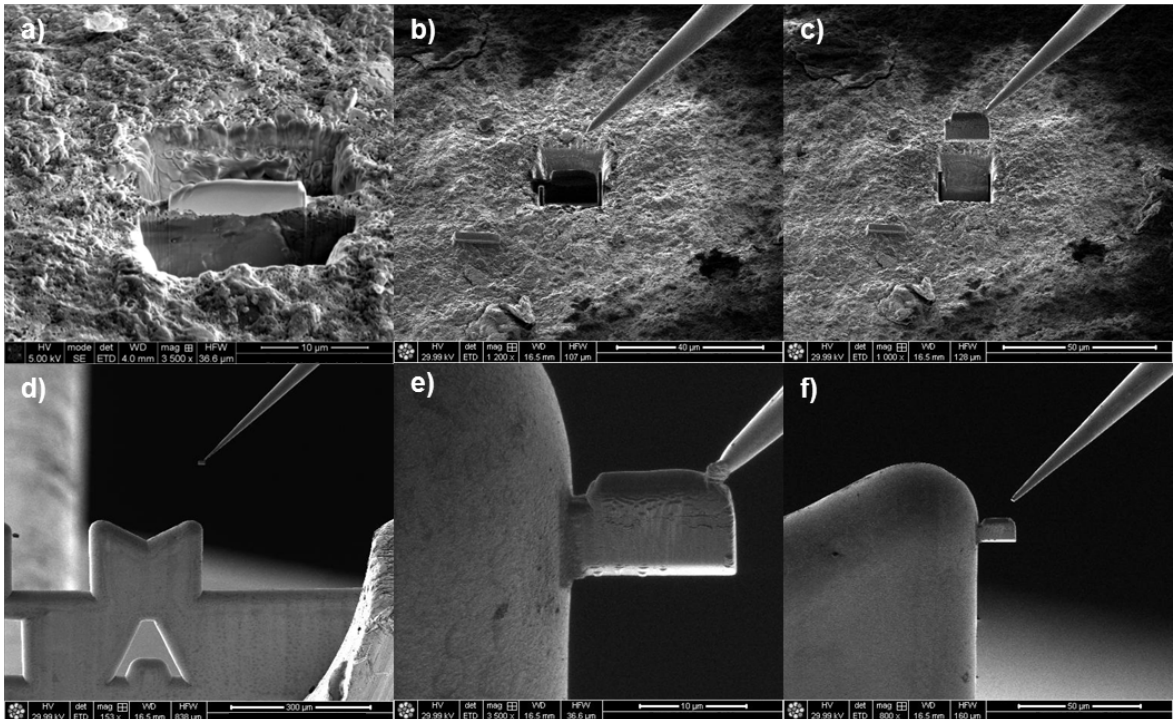

Fig. 14 - STEM sample preparation from Curtis *et al.* (2011). (a) a 2 μm shale STEM sample. (b) Omniprobe (TM) nano-manipulator needle moving into position. (c) Sample attached to needle and sample being lifted out for further preparation. (d) Sample moving closer to grid for further sample prep. (e) Sample attached to grid with platinum, before needle is removed. (f) Needle removed showing sample for final preparations and thinning to less than 100 nm.

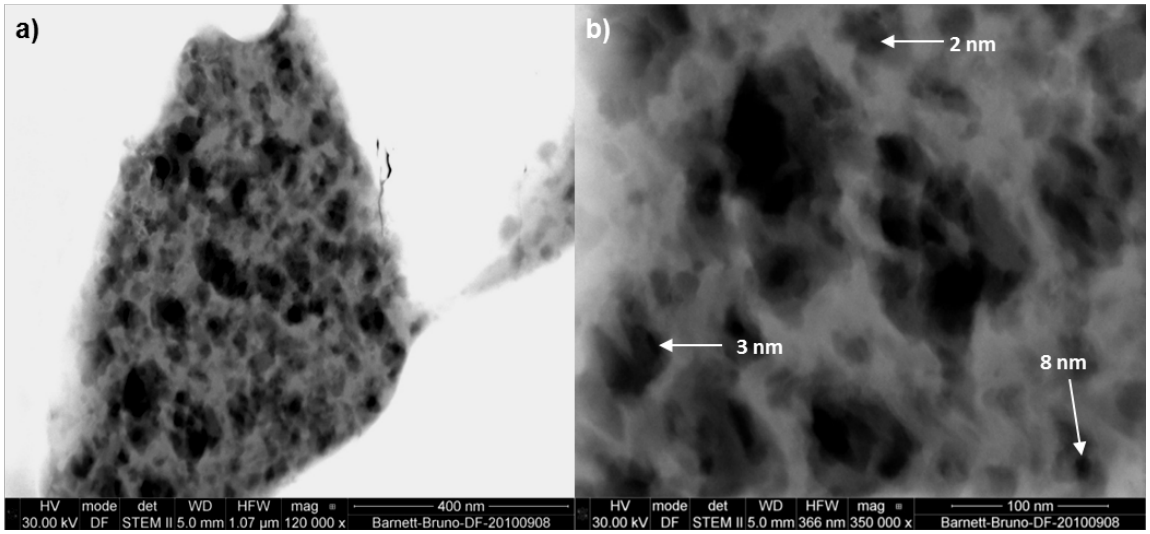

Fig. 15 - STEM images from Curtis *et al.* (2011). (a) STEM image utilizing annular dark-field (ADF) detector showing incredible structure in the kerogen network. (b) Higher magnification, high resolution image where pore throats of various sizes less than 10 nm are pointed out. Based upon the MICP data, they are the pore throats of these sizes that control the connectivity within the kerogen network.

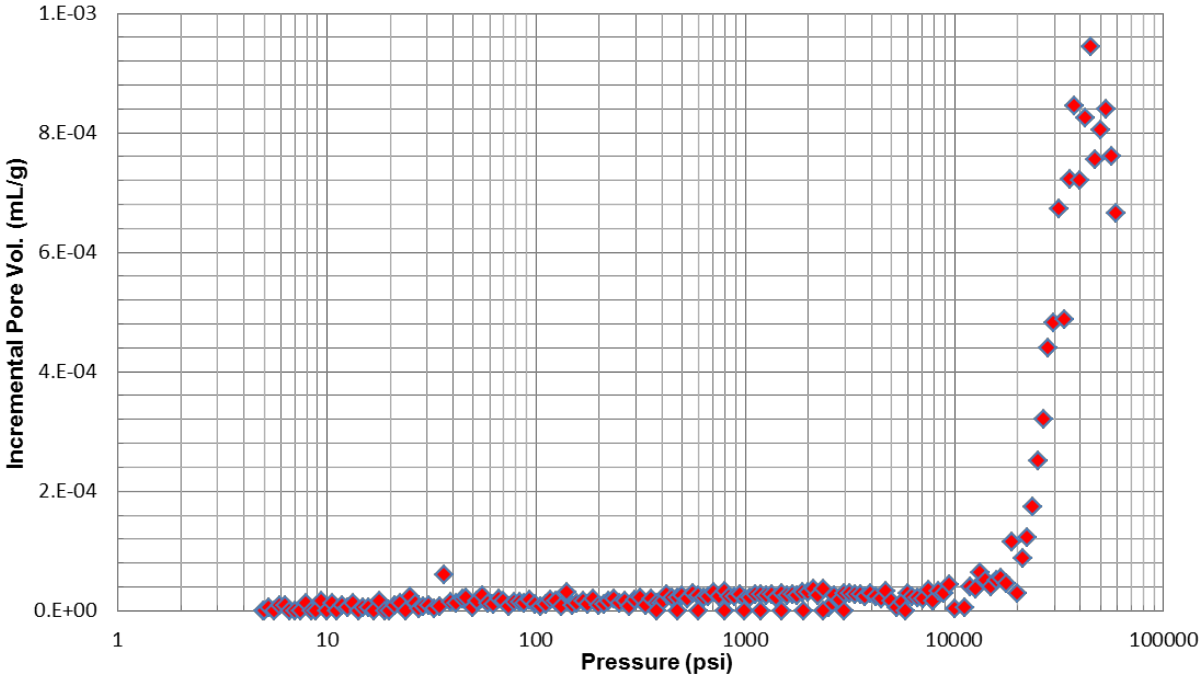

Fig. 16 - MICP data from Curtis *et al.* (2011). Data giving information on the pore throats of the sample (same sample as Fig. 8- 13). Pore throat radius of sample corresponds to 2-3 nm pore throats.

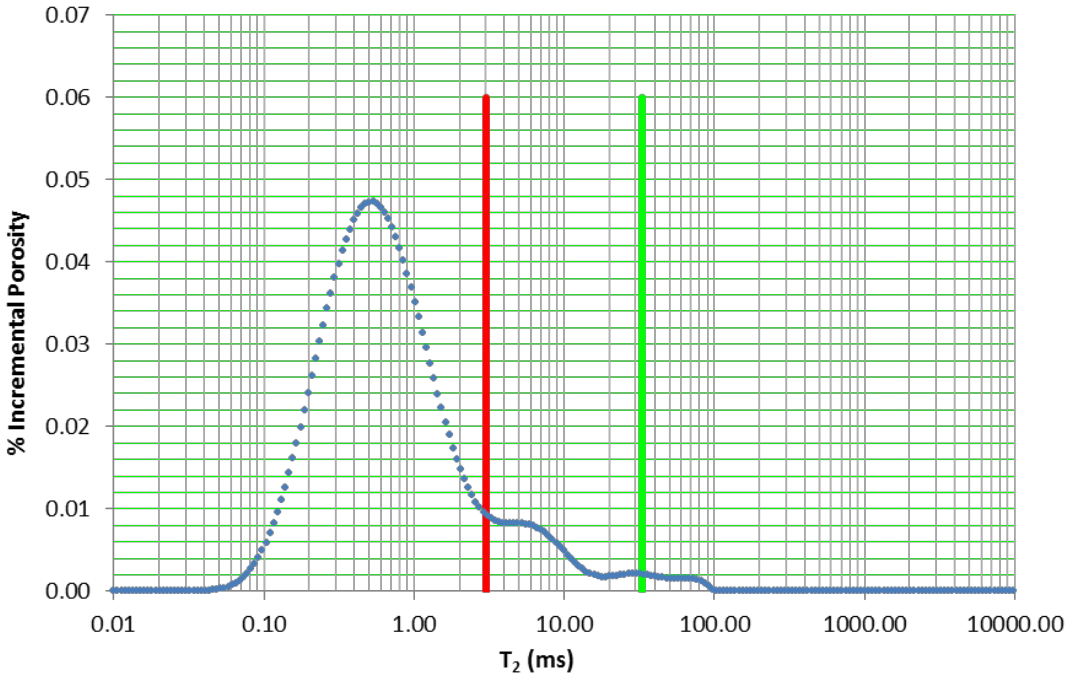

Fig. 17 - NMR data from Curtis *et al.* (2011). Data giving information on the pore bodies of the sample (same sample as Fig. 8- 13). Utilizing a spherical model (Eq. 2b), and a surface relaxivity (ρ) between 0.05 and 0.005 μs/ms, pore bodies range from 6 - 60 nm. This corresponds very well with all visual data taken from SEM and STEM.

CHAPTER III
GAS ADSORPTION IN SHALES

Reservoirs that are defined as unconventional display one or more of the following characteristics; 1) significantly smaller grain and pore sizes exist, often on the clay or mudstone scale; 2) source rock contains organic carbon often called total organic carbon (TOC); and 3) hydrocarbons are contained in an adsorbed state, or attached to surfaces of the porous reservoir rock. Pores in these reservoirs with TOC are often associated with kerogen (Wang and Reed, 2009; Ambrose *et al.*, 2010; Sondergeld *et al.*, 2010a). It has also been found that gas adsorption takes place in these organic pores and in clays in these systems (Hartman *et al.*, 2008). As discovered in chapter two, the extremely small scale creates a problem in characterization because most of the measurements are indirect macroscopic averages. Another issue is that in order to make measurements in a reasonable period of time, the core is often crushed or modified; which leads to issues with repeatability and confidence in the measurement (Sondergeld *et al.*, 2010b).

Adsorption is the process which describes attachment of molecules to a surface. The term adsorbate is used for the molecules attached and adsorbent for the surface they are attached to. Adsorption isotherms are widely discussed in literature due to their relevance in catalyst evaluation and coal-bed methane (CBM). Catalyst effectiveness is usually associated with their surfaces. Therefore sorption, being a surface phenomenon, is usually used to measure the surface area of the catalyst and is one of the methods used most widely in catalyst characterization. Catalysts research defines pores based upon their diameter. **Table 1** is the International Union of Pure and Applied Chemistry

(IUPAC) definitions of pore sizes, based upon work originally performed by Dubinin and Radushkevich (1947).

Pore classification by diameter	
Ultramicropore	≤ 0.7 nm
Supermicropore	> 0.7 and < 2 nm
Mesopore	> 2 and < 50 nm
Macropore	≥ 50 nm

Table 1 - IUPAC pore classification by diameter

Adsorption was first described and modeled by Langmuir (1916). Langmuir made four assumptions in the model he proposed. First, the adsorbent is composed of a uniform surface, and all sorption sites are energetically similar. Second, there is no interaction laterally between the molecules. Thirdly, the kinetic mechanism of adsorption is similar for each molecule. Finally, only a monolayer is formed. **Eq. 3** is one form of the Langmuir equation that mathematically describes the adsorption process at a constant temperature:

$$\theta = \frac{\alpha \cdot p}{1 + \alpha \cdot p} \qquad \textbf{(3)}$$

In this equation θ is the fraction of the surface area that is covered by the adsorbed molecules, P is the pressure of the gas and α is the Langmuir adsorption constant. In the case of shale gas and coalbed methane this equation is rewritten as **Eq. 4**. Here G_{sL}, is commonly called the Langmuir volume. It is a theoretical quantity referring to the maximum adsorbed volume at the measurement temperature and maximum pressure. The Langmuir pressure p_L, is the pressure at which half the gas is adsorbed to the surface. In other words, it is the pressure at which G_s, the amount of gas adsorbed at pressure p is

equal to one-half of G_{sL}. **Eq. 4** can yield the surface area of coverage of an isotherm, if a single layer Langmuir type coverage is assumed.

$$G_s = G_{sL} \frac{p}{p + p_L} \quad \textbf{(4)}$$

The Langmuir isotherm is the simplest model of adsorption. In practice the four assumptions of Langmuir are often not satisfied and, hence, more complicated mechanisms are needed to describe the physical process. IUPAC used the information from sorption experiments to classify porous systems based upon their isotherm shape, shown in **Fig. 18**. In this figure, six types of isotherms are displayed. IUPAC adopted the first five types from the classic work of Brunauer *et al.* (1940). Later this was increased to six with the introduction of isotherm VI by Sing (Gregg and Sing, 1982). Type I isotherms are representative of microporous solids, such as those of kerogen in gas shales. The interpretations of these isotherms are the most difficult. Type II isotherms are representative of a non-porous solid. The type IV isotherm is a characteristic of a mesoporous solid. Both of these isotherms provide information related to surface area. The type IV can be used to determine the mesopore size distribution. Type III and V isotherms are characteristic of systems with weak adsorbent-adsorbate interaction, where the type III system is non-porous and type V system is porous. Type VI isotherms are more theoretical in nature (Gregg and Sing, 1982).

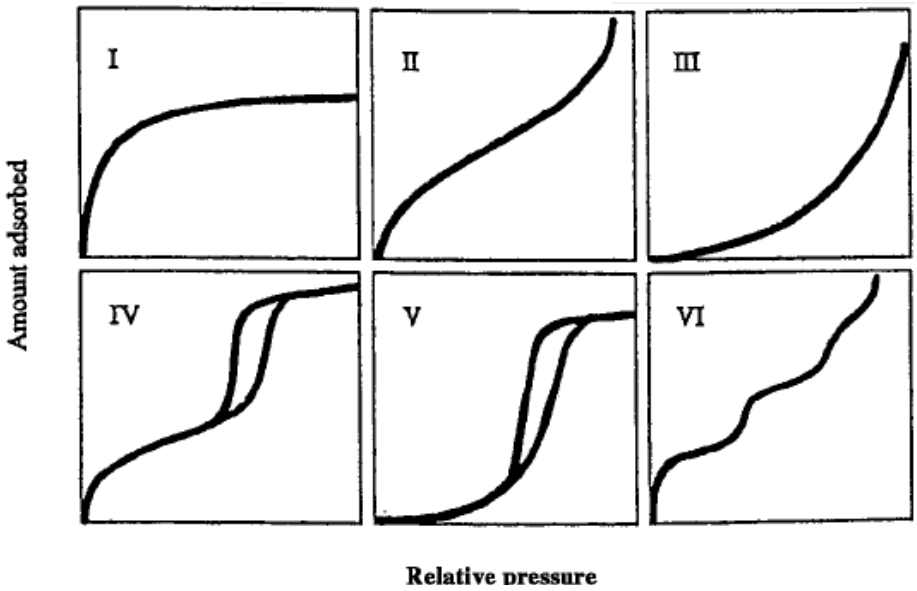

Fig. 18 - IUPAC Classification of Adsorption Isotherms

Early research into adsorption showed that the Langmuir theory cannot explain the intricacies of physical adsorption phenomenon. Most of this early work dealt with measuring the surface areas of catalysts which were an important part of the chemistry and chemical industry research. Brunauer, Emmett and Teller published a seminal paper in 1938 of their work in regards to multi-layer adsorption. They gave an explanation for the two distinct regions of observed isotherms of type II-V. For gases that are near their dew points they commented on a concave region at lower pressures and a convex region at higher pressures. They formulated a generalization of Langmuir's isotherm equation in **Eq. 5**.

$$n = \frac{n_m c p}{\left(p^o - p\right)\left[1 + \left(c - 1\right)\frac{p}{p^o}\right]} \qquad \textbf{(5)}$$

In this equation c is related to the net heat of adsorption (q_1-q_L) through ($c = e^{(q1-qL)/RT}$), n is the number of moles adsorbed and n_m is the monolayer capacity in number of moles.

This equation reduces to **Eq. 3** if the pressure is significantly less than the dew point pressure of the fluid, i.e., $p << p^o$. Additionally, it was observed if an adsorption isotherm is at a pressure region near the dew point, **Eq. 4** can be re-arranged in a linear form, where the slope is $(c\text{-}1)/n_m c$ and intercept is $1/n_m c$ resulting in **Eq. 6**.

$$\frac{p}{n\left(p^o - p\right)} = \frac{1}{n_m c} + \frac{c-1}{n_m c}\frac{p}{p^o} \qquad \textbf{(6)}$$

Plotting $\frac{p}{n(p^o - p)}$ vs $\frac{p}{p^o}$ the two constants n_m and c can be determined (Brunauer *et al.* 1938). If the effective area of the fluid molecule, a_m is known, the surface area of the adsorbent can be calculated. **Eq. 7** is BET calculation for surface area of an adsorbent:

$$A = a_m v_m \qquad \textbf{(7)}$$

This equation is the classical BET equation for the determination of the surface area of a catalyst. A table of values of some typical gases used in adsorption experiments is shown in **Table 2**.

Gas	Adsorption temperature	Saturated vapor pressure	State	Area	
	K	psi		nm^2 per molecule	
				Range	Common value
Nitrogen	77	14.7	liquid	0.13-0.20	0.16
Argon	77	4.0	solid	0.13-0.17	0.15
Krypton	77	0.049	solid	0.17-0.22	0.20
Krypton	90	0.40	liquid	0.17-0.22	0.20
Xenon	90	0.0012	solid	0.18-0.27	0.23
Methane	90	1.6	solid	0.15-0.17	0.16
n-Butane	273	14.7	liquid	0.32-0.57	0.44
Carbon dioxide	195	14.7	solid	0.14-0.20	0.20

Table 2 - Properties of gases used in typical BET measurements (from Anderson and Pratt 1985)

3.1 Practical Considerations of Adsorption Experiments

In gas shales there is a question of how representative is the pore size estimation that is determined from experimentation. Estimation of pore size distribution from methane adsorption is proposed here. With any adsorption experiment, the conditions at which the experiment is run is one of the primary concerns. Most of the adsorption methods described previously must be done at very low temperatures and near vacuum conditions which creates potential experimental error. Hartman *et al.* (2008) and Bustin *et al.* (2008) pointed out that changing the humidity within the apparatus could greatly alter the shape of the shale gas adsorption isotherm. Examples are shown in **Fig. 19a** where two different shale isotherms were measured under different humidity conditions. As can be seen, the gas storage capacity is greatly dependent upon the water content of the shale. It is believed that this is primarily due to the large surface areas exposed by dehydrated clays.

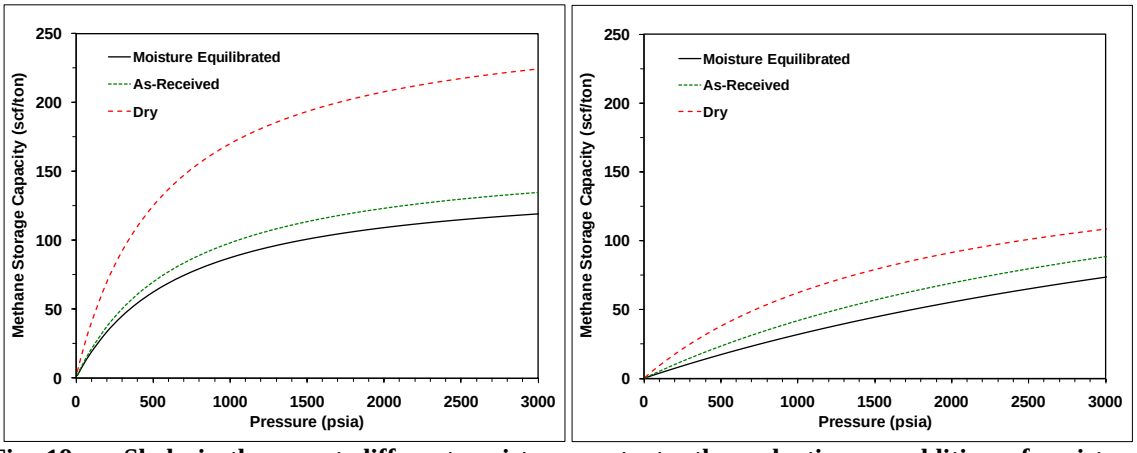

Fig. 19a – Shale isotherms at different moisture contents, the reduction or addition of moisture greatly increases or decreased the sorbed gas content of the shale. (modified from Hartman *et al.* 2008)

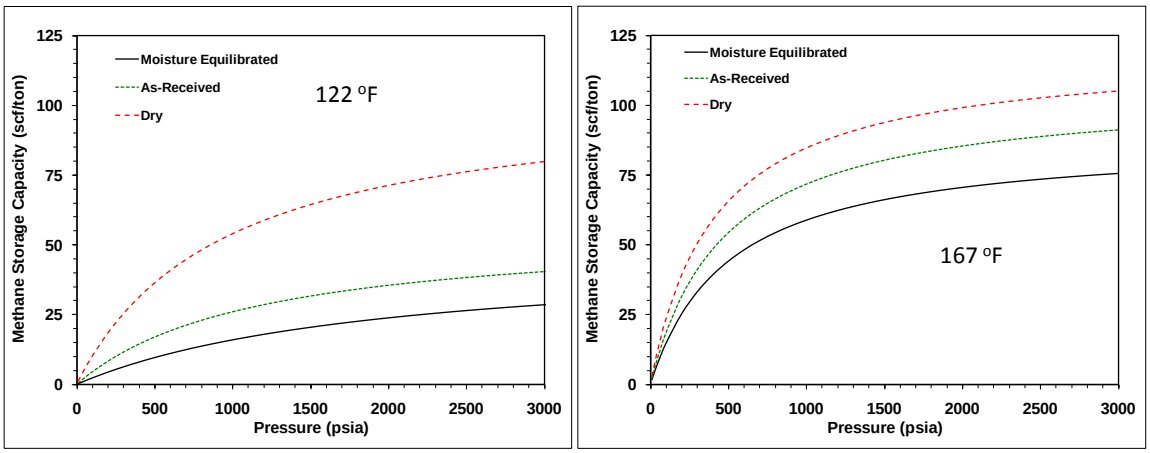

Fig. 19b – Showing dependence of humidity on sorbed gas content of clays (modified from Hartman *et al.* 2008).

Evidence of gas adsorption on dehydrated illite is shown in **Fig. 19b**. In this example Hartman, *et al.* (2008) used industrial grade illite at three different temperatures and moisture contents to study the effects of temperature and adsorption on clays. In this figure, just the higher temperature results are shown. As can be seen from the diagrams the moisture content plays a much larger role than the temperature in terms of determination of gas content if clays only are considered.

Typical gas shales such as Barnett, Woodford, Marcellus, Horn River and Haynesville have large clay percentages, sometimes greater than 60%; therefore, one would expect the results shown in **Fig. 19a** given the knowledge obtained in **Fig. 19b**. Additional evidence has been found for this phenomenon from lab data on gas shales from two different labs.

Presented in **Fig. 20** are two different adsorption isotherm sets, each from a different commercial lab. The graph is a plot of G_{sL} vs. weight % total organic carbon (TOC) content. Because the TOC in a sample is considered as the main location for adsorbed gas storage, the storage capacity of organic shale is often a function of how

much TOC it contains. In order to see the dependence of gas storage on TOC, these plots are often useful in shale gas analysis. One of the laboratories clearly states their protocols and it is known that the moisture equilibrates their samples. The other lab, the protocols are unknown, but as the above figure suggests, one reason might be that the samples are allowed to desiccate. If the clays in the shale are maintain hydrated, one would expect nearly zero storage capacity at reservoir temperatures, due to the clay surface being occupied by water. The small dark blue points represent a nearly 20 scf/ton sorption value at 0% (by weight %) TOC values. If the data from **Fig. 19b** is used and we have roughly 40% illite in this shale, one would expect very low values of clay sorbed gas, using linear extrapolation it should be less than 5 scf/ton (or an intercept near zero on this graph). It is for this reason that the traditional nitrogen adsorption studies to investigate the pore size distributions (PSD) of gas shale cannot be used by themselves. In nitrogen adsorption, the system is brought to very low temperatures, typically the boiling point of nitrogen, 77 K, and very high vacuums. This will in essence desiccate the shale and change the PSD that is obtained (Bustin *et al.*, 2008). However, this method might still be applicable for a comprehensive PSD of the shale.

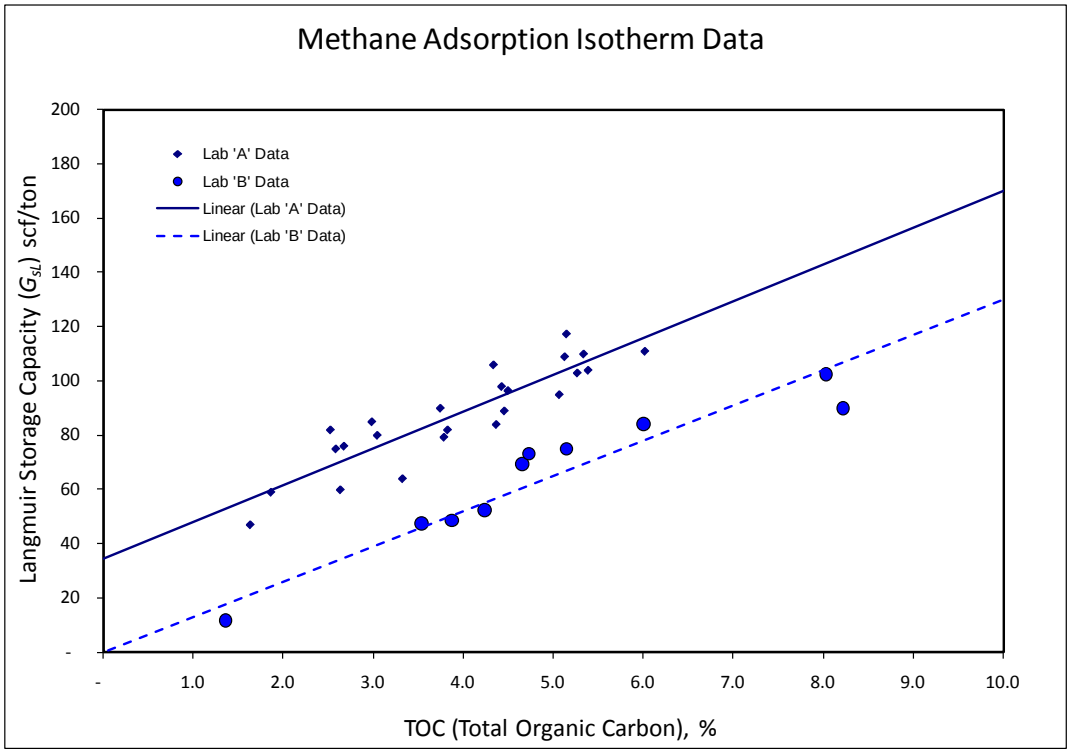

Fig. 20 – Langmuir volume data of organic shale evaluated by two different labs. This data might be an indication of shale sample handling having a large effect on the isotherm.

Adsorbate selection is another important consideration when evaluating sorption isotherms in gas shales. Looking in **Table 2**, the area per molecule is similar for methane, nitrogen, and argon. Utilizing a gas with a larger diameter might preclude the investigation of small micropores. If the proper analysis technique is utilized the choice of adsorptive should not have a large effect on the isotherm analysis, as long as the molecular diameter is similar to reservoir conditions (Bustin *et al.* 2008). Therefore, choice of an adsorbate should not be a large issue. The main issue with adsorbate selection is adsorbate purity. Gases with at least 99.9% purity, preferably purer, should be used (Gregg and Sing, 1982).

The void volume measurement must be considered for an isotherm experiment. Since the void volume changes, by the addition of the sorbed molecular layer(s), this

volume must be well known and accounted for. Ross and Bustin (2007) discussed the negative sorption observations on zeolites with known pore sizes. They noted that since helium has a smaller kinetic diameter (0.26 nm) than the gases that are typically used in the sorption experiment (~0.38 nm) helium might be over estimating the void volume available to the free gas phase. The overestimation of the void volume will have two effects, first, it will overestimate the sorption at low pressures and it will underestimate the sorption at higher pressures (Ross and Bustin, 2007). Additionally, this effect will be amplified at smaller values of TOC. From the theory of gas attaching to the smallest pores first (Gregg and Sing, 1982), this could shift the PSD to slightly smaller pores. Since the experiment itself might introduce this error, more investigation is recommend to see if there is a mechanism to remove this inherent error.

Equilibrium considerations are another important factor in obtaining good isotherm data to obtain quantitative PSD's. As stated earlier, the large surface area to volume ratio provides sites where the dispersive forces become much stronger than the repulsive forces. Therefore, to bring the fluid into equilibrium, some of the fluid must adsorb to the surface until the Gibbs free energy in minimized. Good data depends on equilibrium occurring at every pressure step in the adsorption isotherm experiment. In gas shales, due to the low diffusion rates, the ability for gas to penetrate the system could take a long time. Another item to consider is the time for temperature equilibrium as well. These times must be considered when obtaining data for an adsorption isotherm.

Finally, equipment must be considered in order to obtain good data in an adsorption isotherm. As the term isotherm suggests, the experiment must be temperature

controlled. In methane isotherms at reservoir conditions this is ideally done in an oil bath, where there is a large thermal mass that can compensate for temperature fluctuations. If nitrogen isotherms are to be used, the ability to maintain low temperatures (77 K) must be considered (typically a bath of boiling nitrogen). Additionally, the dead-space should be minimized (Anderson and Pratt, 1985). Dead-volume minimization is achieved by having reference cell and sample cell volumes much larger than the tubing that connects them.

In this work, we use data from adsorption isotherms and simple arithmetic, not to determine a pore size distribution, but to determine a volumetric average pore size. Many assumptions go into this estimate, so the results should be used for qualitative purposes only, however, it lends further evidence to support the values that are obtained by MICP, NMR and image analysis.

3.2 Estimation of Pore sizes within Kerogen Network from Langmuir Isotherm Data

The simplified model approach will assume a monomolecular layer that is attached to the surface of a number of organic pores. All of the pores in the shale will have the same shape: either spherical or cylindrical, since both shapes will be investigated. The adsorbed molecular area for methane is given in Table 2 and it will be used as the area occupied by one molecule. Schettler *et al.* (1989) utilized the BET method for Devonian shales to obtain an average pore throat radius of 5.5 nm, if slit type pore geometry was assumed. The shale analyzed has the physical characteristics shown in **Table 3**.

Parameter	Symbol	Value
Porosity	ϕ	6%
Water Saturation	S_w	35%
Bulk Density	ρ_b	2.5 g/cm^3
Langmuir Volume	G_{sL}	50 scf/ton

Table 3 – Shale Parameters for Effective Pore Size Determination from a Langmuir Isotherm

First, the total volume available for gas sorption must be calculated. It is assumed that the pores containing water will not have any surfaces where gas adsorption can occur and that volume of gas that can dissolve in the water is negligible. The units conversion and math is outlined below, the basis is 1 ton of rock:

$$\text{Gas filled pore space of 1 ton of rock} = \frac{\text{mass of rock}}{\text{bulk density}}\phi(1 - S_w)$$

$$1\,\text{ton} \times \frac{907184.75\,\text{g}}{\text{ton}} \times \frac{\text{cm}^3}{2.5\,\text{g}} \times 0.06 \times (1 - 0.35) = 14{,}152\,\text{cm}^3 \text{ of pore space}$$

$$\text{Number of lb - moles in 1 scf of gas}$$

$$n = \frac{p_{std}V}{RT} = \frac{14.69\,\text{psi} \cdot 1\,\text{scf}}{10.73159\,\frac{\text{scf psi}}{^{\circ}\text{R lb - mol}}(60 + 459.67)^{\circ}\text{R}} = 2.634 \times 10^{-3}\ \text{lb - mol}$$

$$\text{Number of molecules in 50 scf of gas}$$

$$50 \cdot 2.634 \times 10^{-3}\ \text{lb - mol} \cdot 453.59237\,\frac{\text{g}}{\text{lb}} \cdot 6.02214 \times 10^{23}\,\frac{\text{molecules}}{\text{g - mol}} = 3.5976 \times 10^{25}\,\text{molecules}$$

Given the area that one molecule covers from **Table 2**, we can calculate how much area is covered by the above number of molecules of methane.

$$3.5976 \times 10^{25}\,\text{molecules} \times \frac{0.16\,\text{nm}^2}{\text{molecule}} = 5.7562 \times 10^{24}\,\text{nm}^2 \quad \text{(for monomolecular coverage)}$$

We can use the volume to surface area ratio to calculate the radius of molecules needed to cover a uniform size for a sphere and a cylinder; this is shown in **Eq. 8** and **Eq. 9**. For the cylinder we will assume that it is a cylinder without any flat ends so only the curved surface area will be calculated.

For a sphere:

$$\therefore \frac{nV}{nA_s} = \frac{n\frac{4}{3}\pi r^3}{n4\pi r^2} = \frac{r}{3} \qquad \textbf{(8)}$$

For a cylinder with no ends:

$$V = \pi r^2 L \text{ and } A_S = 2\pi r$$
$$\therefore \frac{nV}{nA_S} = \frac{nL\pi r^2}{nL2\pi r} = \frac{r}{2} \quad \textbf{(9)}$$

Using the gas volume of 1.4152 x 10^{16} nm^3 (14,152 cm^3) and different ratios of the porosity in the organic from 10% to 100%, we can calculate the pore size assuming spherical or cylindrical pores. An example of this calculation is shown below for spherical pores and 50% of the effective pore volume in the organics noted by the factor *f*.

$$\frac{nVf}{nA_S} = \frac{r}{3}$$
$$\therefore r = 3\frac{nVf}{A_s}$$
$$r = 3\frac{1.41562\times10^{16}\ \text{nm}^3 \times 0.5}{5.7562\times10^{24}\ \text{nm}^2} = 3.69\ \text{nm}$$

Table 4 and **Fig. 21** show the computed values of pore throat radius if there is monomolecular coverage of methane in the organics as a function of *f*, for both spherical and cylindrical pores.

Fraction of Porosity in Organic	Spherical Pore Radius	Cylindrical Pore Radius
	r nm	*r* nm
0.1	0.74	0.49
0.2	1.48	0.98
0.3	2.21	1.48
0.4	2.95	1.97
0.5	3.69	2.46
0.6	4.43	2.95
0.7	5.16	3.44
0.8	5.90	3.93
0.9	6.64	4.43
1	7.38	4.92

Table 4 – Computed Pore throat radii from monolayer isotherm analysis

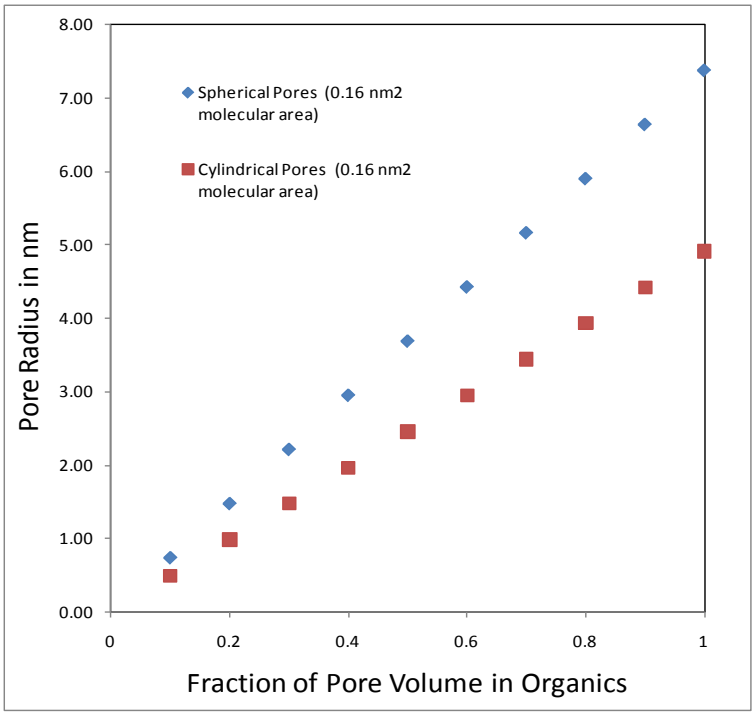

Fig. 21 – Graph of computed pore throat radii from monolayer isotherm in a gas shale using a 0.16 nm^2 per methane molecule for molecular area.

The values computed from this method are very close to the ones obtained from 3-D SEM analysis. In fact if you combine the data, it would suggest that between 20-70% of the gas pore volume in shale is associated with the kerogen. The density of this single layer (assuming a thickness of 0.4 nm) can be calculated because we have the volume of the area of one molecule and the molecular weight. In the system above, the density of the single layer is calculated as 0.415 g/cc, however, as shown in chapter four, the density will be shown to be less than this.

Possibility of a multiple layer thickness has been observed in methane adsorption. Ambrose *et al.*, (2010) and Tan and Gubbins (1990) to name a few, noted a damped oscillation in the density profile. Molecular dynamics (MD) simulation was utilized to determine these values. More on MD simulation will be discussed in chapter four of this

dissertation. This is shown in **Fig. 22**. From this profile, the first layer has a density between 0.28 g/cm^3 and the second layer has a density of ~0.16 g/ cm^3. Converting this density to a single layer density, different results are obtained. The single layer density

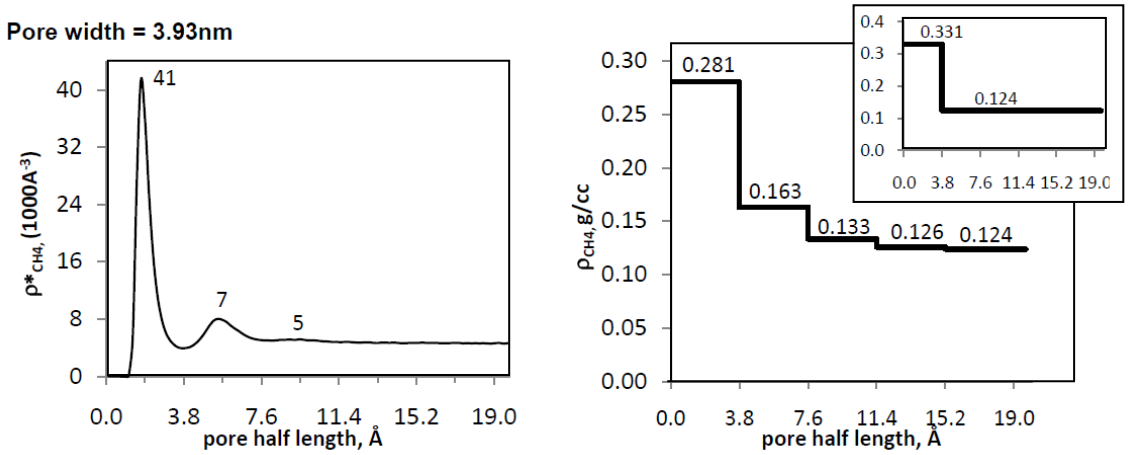

Fig. 22 - Number density (left) and discrete density (right) profiles for methane as a function of pore size at 176oF (80oC). Density values are estimated at each 0.2 Å interval for the continuous density profile. Discrete density corresponds to molecular layer density for methane across the pore. The estimated pore pressure at the center of the pores is 3,043 psi. Insert graph in right upper hand corner is the equivalent density using a Langmuir single layer adsorption model. (From Diaz-Campos, 2010)

value determined from MD is 0.331 g/ cm^3 for the sorbed phase (Diaz-Campos, 2010 and Ambrose *et al.*, 2010). Utilizing this data a slightly different pore size will be determined from MD. This is because one molecule will take up more area than the theoretical values suggest. From theory, one molecule of methane has the volume of 0.064 nm^3. This is determined by taking the cube of the square root of the area (assuming the molecule takes up a box shaped space). Since the density of this value determined previously was 0.415 g/ cm^3, but from simulation it needs to be 0.331 g/ cm^3, we can just simply divide the previous density by the new density, and use this factor to determine a better volume for one molecule. This volume is 0.0803nm^3. By taking the square of the cube root of this value, an area per unit molecule of 0.186 nm^2 per molecule was

determined. This value was then used in the equations above and the results are shown in **Fig. 23**. A comparison between the values is shown in **Fig. 24**.

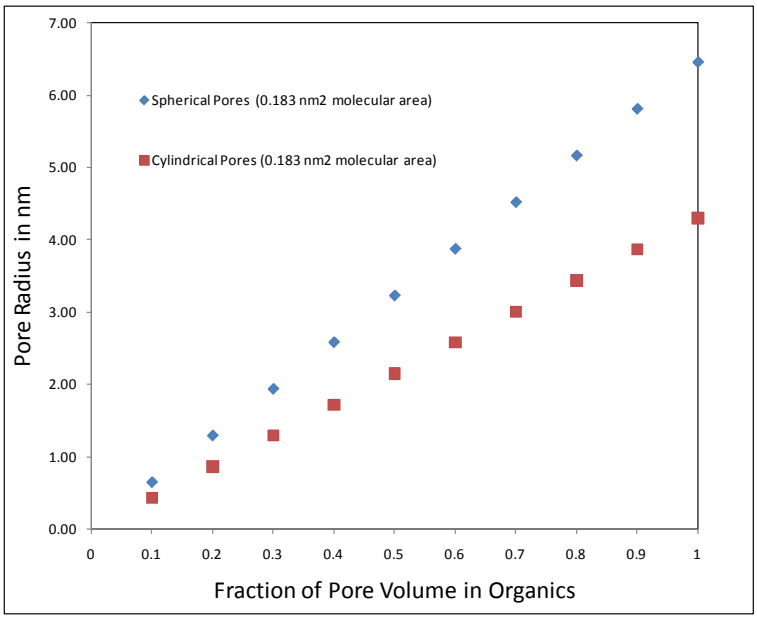

Fig. 23 – Estimated Pore size as a function of fraction of pore volume in the organics using a greater area per molecule from lower sorbed phase density 0.183 nm2 per molecule.

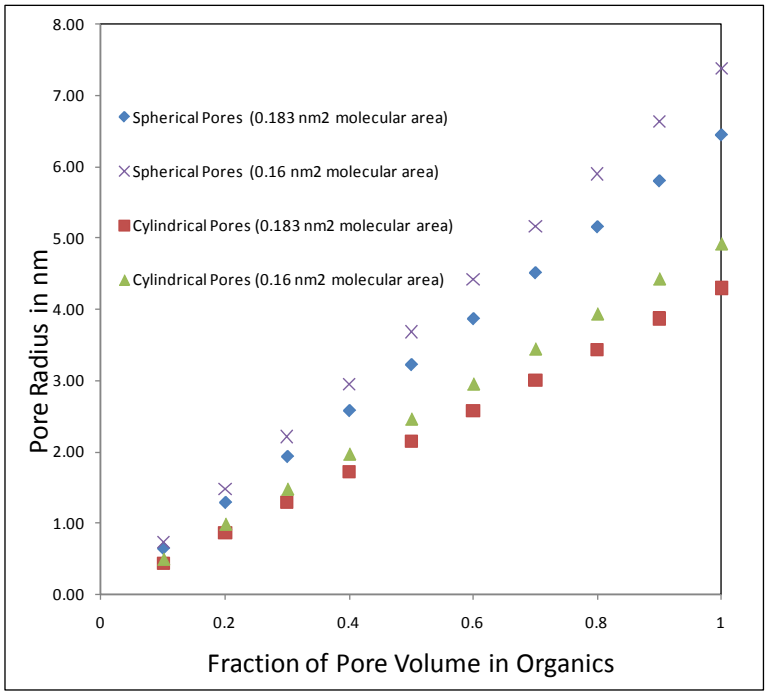

Fig. 24 – Estimated Pore size as a function of fraction of pore volume in the organics comparing different areas (and therefore densities) per unit molecule.

In this figure, it can be seen that for a sample with 50% of the gas pore volume in the organics, the pore radii are expected to range between 2.1 and 3.8 nm. This is consistent with the MICP data as discussed in Chapter 2.

CHAPTER IV
ADSORPTION EFFECT ON GAS STORAGE IN SHALES - SINGLE COMPONENT MODEL

The amount of gas produced from a shale gas reservoir is a function of many parameters including but not limited to volume of the stimulated reservoir created, total fracture area, drawdown, and gas-in-place. For reservoir studies on these types of fields, one of the critical concerns is the proper estimation of the original gas-in-place (OGIP). Its value is the foundation of the estimation of gas reserves and critical in reserves forecasts. Many different types of models are used for this estimation including volumetric method, tank-type models using material balance, multi-dimensional (finite-difference and finite-element) simulation-based models, some analytical models, and empirical performance-based models. All of these methods must use OGIP as model constraints. The volumetric method is the most widely used approach due to its simplicity; however, it heavily relies on the knowledge of key reservoir parameters such as water saturation, porosity, formation compressibility and fluid properties. These parameters are often estimated from core, transformed from log data and modeled from well tests. Furthermore, these volumetric parameters enable the prediction and estimation of the gas-in-place in a reservoir. Often, a deterministic method is employed for the estimation of gas-in-place and is the most common method utilized in North America. Recently, probabilistic methods have become more popular due to the limited amount of data that is collected compared to the size of the reservoir.

A simple volumetric petrophysical model of the shale matrix is illustrated in **Fig. 25**. There is an inorganic component consisting of clays and other inorganic particles, an

organic constituent which can include kerogen and an associated bitumen or oil, a water phase typically associated with the clay particles, and void space. The void space is where the free gas resides, while the sorbed phase is typically associated with the organic portion. The gas-in-place in this model is, in general, quantified using methods developed specifically, for tight, low permeability formations (Luffel and Guidry, 1992; Luffel *et al.*, 1993; and GRI, 1997). In these methods, the effective pore volume is not directly determined; rather a total porosity, total water saturation and total oil volume (by weight difference and an assumed oil density of 0.8 g/cm^3) are determined.

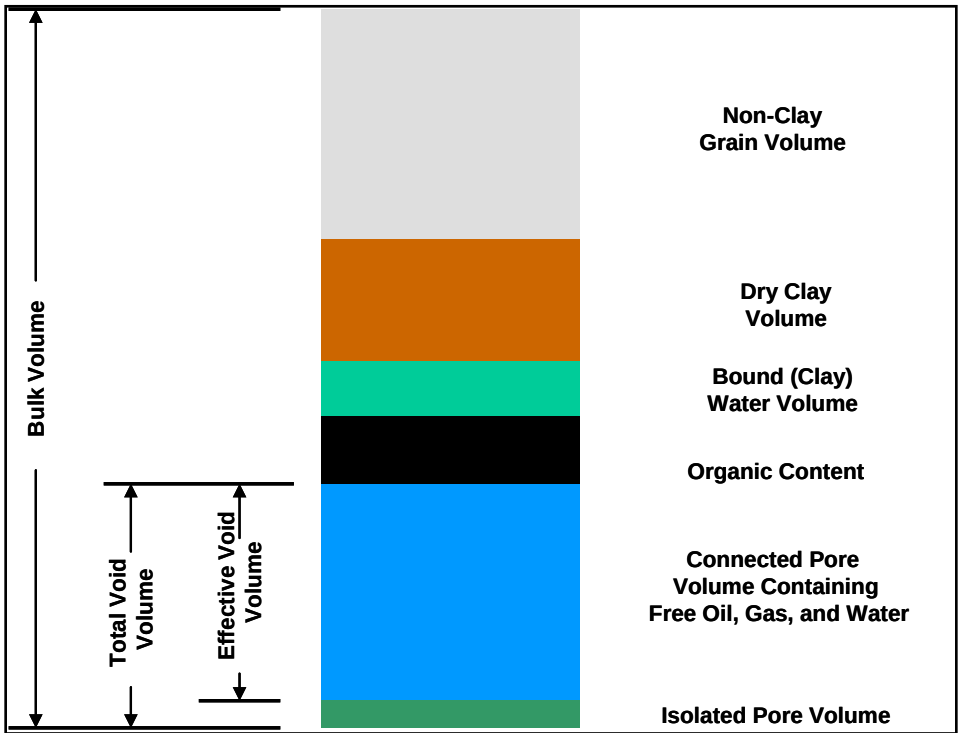

Fig. 25. - Petrophysical model showing volumetric constituents of a typical gas-shale matrix.

For the total gas stored in shale, the gas-in-place volume is considered to have four components:

- A volumetric component, G_f, involving hydrocarbons stored in the pore space as free gas. The free gas volume is quantified by modifications of standard reservoir evaluation methods.
- A surface component, G_s, with the gas physically adsorbed on large surface area of the micro- and mesopores. The adsorbed gas amount has generally been quantified from the sorption isotherm measurements by establishing an equilibrium adsorption isotherm.
- A volumetric component, G_{so}, involving gas dissolved into the liquid hydrocarbon. This volume is usually combined with adsorbed gas capacity in reservoirs that contain a large fraction of liquid hydrocarbon in the pore space.
- A volumetric component, G_{sw}, involving gas dissolved in the formation water. The amount of dissolved gas is estimated from bulk solubility calculations. Although it has traditionally not been considered important, a recent study is available discussing significant enhancement in gas solubility in formation liquids when confined to small pores (Diaz-Campos and Akkutlu 2011).

Therefore these volumes can be summed using the following **Eq. 10 (a-d)**.

$$G_{st} = G_f + G_s + G_{so} + G_{sw} \qquad \textbf{(10)}$$

where:

$$G_f = 32.0368 \frac{\phi(1 - S_w - S_o)}{\rho_b B_g} \qquad \textbf{(10a)}$$

$$G_s = G_{sL}\frac{p}{p + p_L} \tag{10b}$$

$$G_{so} = \frac{32.0368}{5.6146}\frac{\phi S_o R_{so}}{\rho_b B_o} \tag{10c}$$

$$G_{sw} = \frac{32.0368}{5.6146}\frac{\phi S_w R_{sw}}{\rho_b B_w} \tag{10d}$$

In current industry methods, solution gas in hydrocarbons and gas dissolved in water are measured combined with the adsorption isotherm. Therefore **Eq. 10** is reduced to:

$$G_{st} = G_f + G_s \tag{11}$$

The main issue with this approach is that the terms on the right-hand-side of **Eq. 11** must be measured independent of one another. This comes from the previously held thought that the free gas pore space was in the inorganic portion of the rock, while the adsorbed gas was held in the organic portion of the rock, and hence were unrelated. However, if the petrophysical model is changed to one where the porosity for the free gas can be additionally associated with the pore space within the organic portion of the matrix, it can then have an effect on how gas-in-place is determined in these types of unconventional reservoirs. Abundant evidence has now been discussed where at least a portion of the free gas pore space has been associated with the organic fraction of the matrix (Loucks *et al.*, 2009; Wang and Reed 2009; Sondergeld *et al.*, 2010a, Ambrose *et al.*, 2010). This simple observation has a direct effect on the porosity available for the free gas storage.

4.1 Sorbed Phase Void Volume Correction

Sorbed gas estimation in shale is determined through an adsorption isotherm experiment. A void volume is first measured typically using helium in this experiment. Helium pycnometry techniques identical to that used for grain density are utilized for the void volume determination. Helium is used as a gas at low pressures because it is essentially non-sorbing, although some authors have raised the issue of molecular size of the fluid used (Bustin *et al.*, 2008, Kang *et al.*, 2010) as a source of error; this error will not be discussed here. Sorption data are collected after the void volume has been measured. Typically five to ten pressure steps are performed where the sample chambers must reach equilibrium. In this part of the experiment after equilibrium is achieved, the mass of adsorbent sorbed into the sample is measured by material balance and determined by a thermodynamic equation-of-state. At each pressure step in the adsorption experiment the volume of gas sorbed onto the adsorbate reduces the void volume. As a result, the initially determined void volume V_{v0} must be corrected at the beginning and at the end of the pressure step as described in **Eq. 12** and **Eq. 13** (Menon, 1968).

$$V_{v1} = V_{v0} - \frac{n_1 \hat{M}}{\rho_s} \tag{12}$$

$$V_{v2} = V_{v0} - \frac{n_2 \hat{M}}{\rho_s} \tag{13}$$

The void volume must be reduced at each pressure step. During the measurement of an adsorption isotherm it is often more practical to determine the number of moles of

gas adsorbed onto a sample. Often, a Gibbs isotherm is measured due to the practicality. In a Gibbs isotherm, the number of moles of adsorbed gas is measured and volume corrections are performed using **Eq. 14**. The Gibbs isotherm is then converted to volumes using an equation of state. The volumes are then corrected to Langmuir volumes using the Gibbs correction factor ρ_f/ρ_s, the ratio of the two fluid phase densities. This correction is shown in **Eq. 15**, where the measured sorbed volume G'_s is corrected to the sorbed Langmuir volume G_s. An example of a correction from a Gibbs isotherm to a

$$n'_2 = n'_1 + V_r\left(\frac{p_{r1}}{z_{r1}RT_{r1}} - \frac{p_{r2}}{z_{r2}RT_{r2}}\right) + V_{v0}\left(\frac{p_{s1}}{z_{s1}RT_{s1}} - \frac{p_{s2}}{z_{s2}RT_{s2}}\right) \quad \textbf{(14)}$$

$$G_s = \frac{G'_s}{1 - \frac{\rho_f}{\rho_s}} \quad \textbf{(15)}$$

Langmuir isotherm is shown in **Fig. 26**. In this figure, it can be seen that the volume determined by the Gibbs isotherm begins to decrease as pressure increases. This is due to the Gibbs correction factor in the denominator of **Eq. 15**. This factor is typically considered a constant, but later in this dissertation, will be shown that it might need to be a function of pressure specifically in reservoirs at higher pressures, or dominated by micropores.

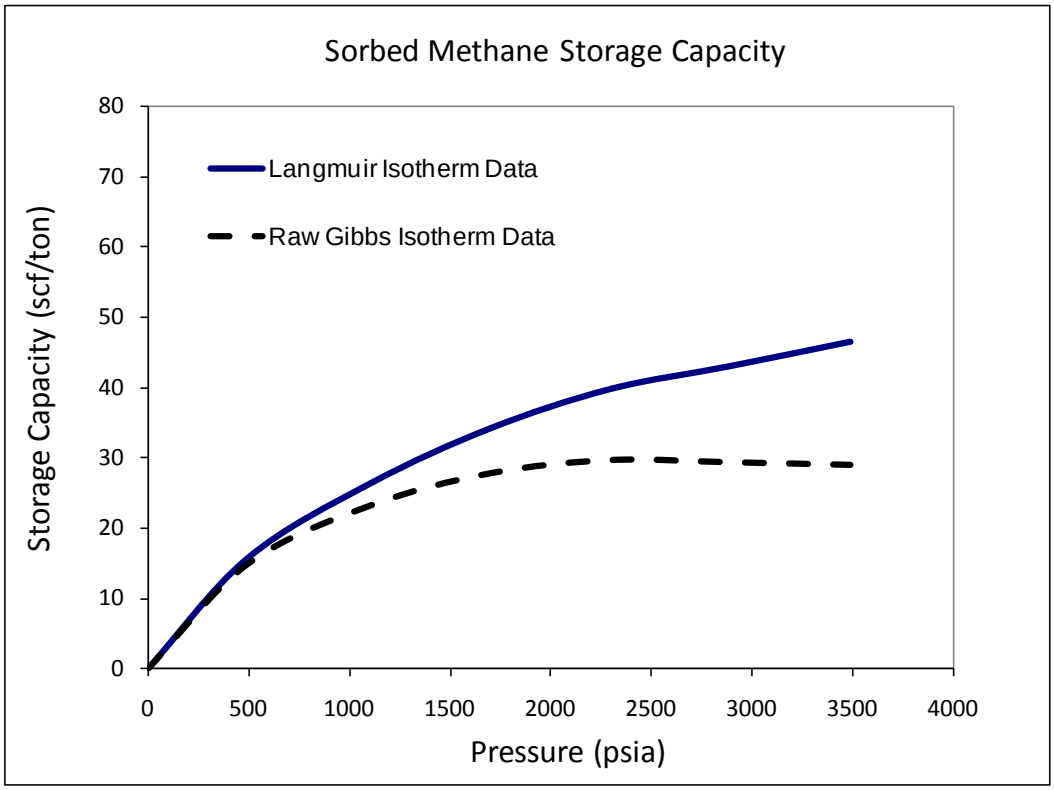

Fig. 26 - Methane isotherms with and without Gibbs correction.

The sorbed phase void volume correction can also be expressed in terms of porosity. Since sorbed volumes are often a function of a Langmuir model, and are reported in typical units of scf/ton, they can actually be thought of in terms of a mass. This is convenient, since if the density of the material is known, then the mass can be turned into a volume. **Appendix A** goes through the conversion of a sorbed gas mass conversion to a volume (on a porosity basis). It is important to note that two densities are critical in this conversion. The first, the bulk density (ρ_b), is a matter practicality and determined from a mercury displacement measurement. The second, the sorbed phase density (ρ_s), is much more difficult to determine. Since the temperatures and pressures associated with sorption in gas shales are often above the critical values, it is difficult to determine the values through experimentation. We therefore resort to theoretical

considerations to determine these values. In addition, since the gas-in-place determination for shale gas reservoirs came from methods taken from coal-bed methane studies, they are often reported on an scf/ton basis. Therefore, some conversion factors are needed; these are provided in **Appendix A**. **Eq. 16** is the porosity fraction occupied by the sorbed gas as a function of pressure. Since the Langmuir model is a function of pressure it conveniently fits into the sorbed gas porosity equation.

$$\phi_a = 1.318\times10^{-6}\hat{M}\,\frac{\rho_b}{\rho_s}\left(G_{sL}\,\frac{p}{p+p_L}\right) \qquad \textbf{(16)}$$

One can also think of the sorbed phase as having saturation units much like oil, water or gas. The basis of saturation units is that it is a fraction (or percentage) of the pore space occupied by a particular phase. Typically, within shales, there is a water and gas saturation (S_w and S_g respectively) along with a possible oil saturation (S_o). The basis of their value is that of a dry sample. However, the sum of all the saturation fractions must equal one. Adsorbed phase saturation is simply the sorbed phase porosity fraction divided by the total porosity of the system.

$$S_a = \frac{\phi_a}{\phi} \qquad \textbf{(17)}$$

4.2 New Petrophysical Pore Volume Model for Gas Shales and Implications on Modeling

The fact that the sorbed phase takes up actual pore volume is an important consideration in modeling these types of reservoirs. Without the proper foundational physics, models will give erroneous answers and forecasts will become unreliable. A new petrophysical model for gas shale reservoirs is shown in **Fig. 27**. In this figure, the

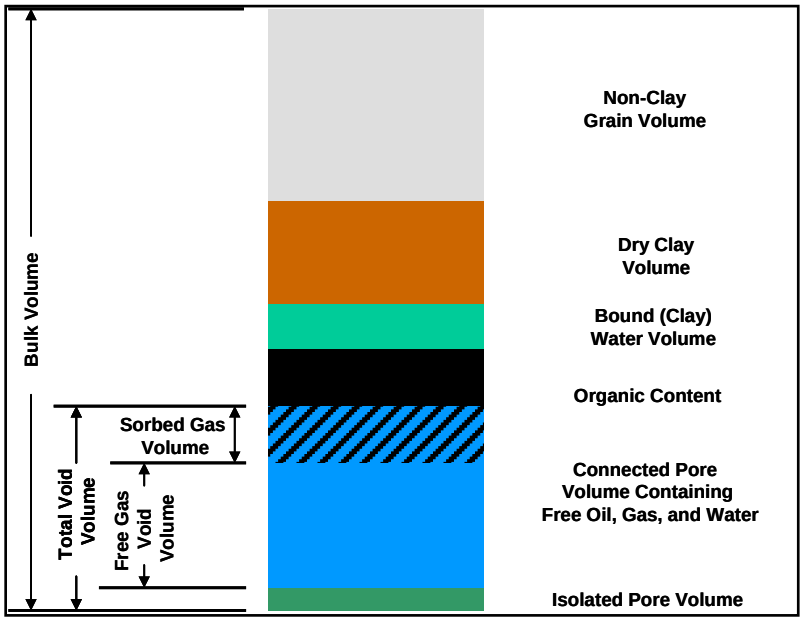

Fig. 27 - New petrophysical model showing volumetric constituents of gas-shale matrix. The hashed region describes the interplay between the sorbed phase and total porosity (void volume).

sorbed phase occupies part of the total void volume in shale. Depending upon the method used for determining the void volume, volume occupied by clay bound water can also be considered part of the total void volume (Passey *et al.* 2010). Utilizing this conceptual petrophysical model showing that the sorbed phase takes up a volume and is a function of pressure as displayed in **Eq. 16**, a new equation for gas-in-place is shown in the following section.

4.3 New Equation for Single Component Gas-in-place for Reservoirs with a Significant Sorbed Phase

Since the sorbed phase takes up a volume and, hence, has saturation, a new equation for the free gas portion of a reservoir with a significant sorbed phase is required. By simply adding a sorbed phase saturation (S_a) to **Eq. 10a** a new equation for the free gas in a system with a significant sorbed phase is shown in **Eq. 18**. This equation is also given in complete form in **Eq. 19**, where **Eq. 16** is substituted for S_a.

$$G_f = 32.0368 \frac{\phi(1 - S_w - S_a)}{\rho_b B_g} \tag{18}$$

$$G_f = \frac{32.0368}{B_g}\left[\frac{\phi(1 - S_w)}{\rho_b} - \frac{1.318 \times 10^{-6} \hat{M}}{\rho_s}\left(G_{sL}\frac{p}{p + p_L}\right)\right] \tag{19}$$

This equation can be modified to other forms, since it is pressure dependent (both in the sorbed phase correction and in the gas formation volume factor). It can be used in analytical equations, material balance equations, or simulation models to better handle the storativity portion of the models. Additionally, due to the basis of the water saturation values, the volume occupied by the sorbed phase must be accounted for after the correction for water saturation. The next question that must be answered is "How do we estimate the density of the sorbed phase, when it is a critical fluid?"

4.4 Single Component Sorbed Phase Density Model

The volume occupied by the sorbed phase is primarily a function of three items. First, the amount of the sorbed phase needs to be known. This has been largely addressed by the Langmuir adsorption model and sorption experiment. Second, the composition of the sorbed phase is considered. This question will be answered in Chapter 5 of this dissertation. Finally, the density of the sorbed phase needs to be predicted. Although, it does depend on composition, the density will first be investigated in this chapter for a single-component case.

Measurement of the sorbed phase is not an easy laboratory experiment. Since the sorbed phase is considered a critical fluid, its density cannot be directly measured, but must be inferred from a model. Additionally, the local density of methane would be expected to vary across a pore due to the vapor-surface interactions. Also, when the pore is small, the density would be expected to vary as a function of pore size as well. Several researchers have studies and made suggestions to determine the density of the sorbed phase. These appear in chemistry literature.

Dubinin, (1960) suggested that the adsorbate density is related to the van der Waals co-volume constant, *b*. Independently, Haydel and Kobayashi, (1967) used an experimental method and found the density values for methane and propane to be nearly equal to the van der Waals co-volume constant. Later, it was argued that the sorbed gas density is equivalent to the liquid density, (Menon, 1968), and to the critical density, (Tsai *et al.* 1985), of the sorbed gas. Ozawa *et al.* (1976) considered the adsorbed phase as a superheated liquid with a density dependent upon the thermal expansion of the

liquid. Recently Ming *et al.* (2003) compared all previously stated methods to a Langmuir-Freundlich adsorption model and found that there exists a temperature-dependence to the sorbed phase density, but the value approaches that proposed by Dubinin (1960). These studies, although fundamentally important to our understanding of gas adsorption in shale, do not show a clear and accurate path to estimate the adsorbed phase density of shale gas, hence, gas-in-place.

Diaz-Campos (2010) recently utilized a numerical molecular modeling and simulation approach to determine the adsorbed phase density of a fluid in a model pore under thermodynamic equilibrium conditions from the first principles of Newtonian mechanics. Molecular modeling and simulation is a form of computer simulation that enables us to study thermodynamic and transport properties of many-particle systems, in which particles (atoms and molecules that make up the natural gas and pore-walls) with initially-known and instantaneously-predicted positions and momenta are allowed to interact for a period of time giving a view of the motion of the particles as trajectories in space and time. Numerical integration of the Newton's equations of motion make up the core of the simulation, therefore, special algorithms (e.g., Verlet, Leap Frog, or Beeman algorithms) have been developed and commonly utilized during a molecular simulation study. Readers who are interested in details of molecular simulation are encouraged to visit textbooks by Frenkel and Smit (2002), and Allen and Tildesley (2007) for deterministic and stochastic treatment of the numerical integration process. Diaz-Campos (2010) performed MD simulations for a molecular-level investigation. Methane was considered at some supercritical condition under thermodynamic equilibrium in three-

dimensional periodic orthorhombic pore geometry consisting of upper and lower pore-walls made of graphene (carbon) layers. She compared thermodynamic state of methane in various slit-like pores in terms of the predicted methane density across the pore. The model pores used in her simulations had pore width varying from 3.73 nm, for the large pore, to 2.08 nm, for the small pore.

Density profiles for methane confined to the large and small model pores are shown in **Fig. 28**. It is clear that the predicted density is not uniform across the pores; its value is significantly greater near the wall, where adsorption takes place, and decreases with damped oscillations as the distance from the pore wall increases. The oscillations are due to presence of adsorption in the pores and involve structured distribution of molecules, i.e., molecular layers. The layers indicate the existence of thermodynamic equilibrium in the pore. The number of molecules is the largest in the first layer near the wall indicating physical adsorption. The wall effect becomes significantly less in the second layer, indicating that desorption of some methane molecules is allowed due to equilibrium adsorption. The molecules in the second layer are still under the influence of pore walls although intermolecular interactions among the methane molecules begin dominating, not allowing locally high methane densities. In this layer, the density of methane is slightly larger than the bulk gas density of methane (at the center of the pore). The bulk density can be independently obtained using NIST-SUPERTRAPP®. The pore pressures are around 3,000 psia for these runs which is a quantity predicted using number of the free gas molecules and the free gas volume at the center of the pore. The observed density profiles show that the assumption of Langmuir adsorption theory with monolayer

is reasonable to describe equilibrium adsorption dynamics of natural gases in the organic pores.

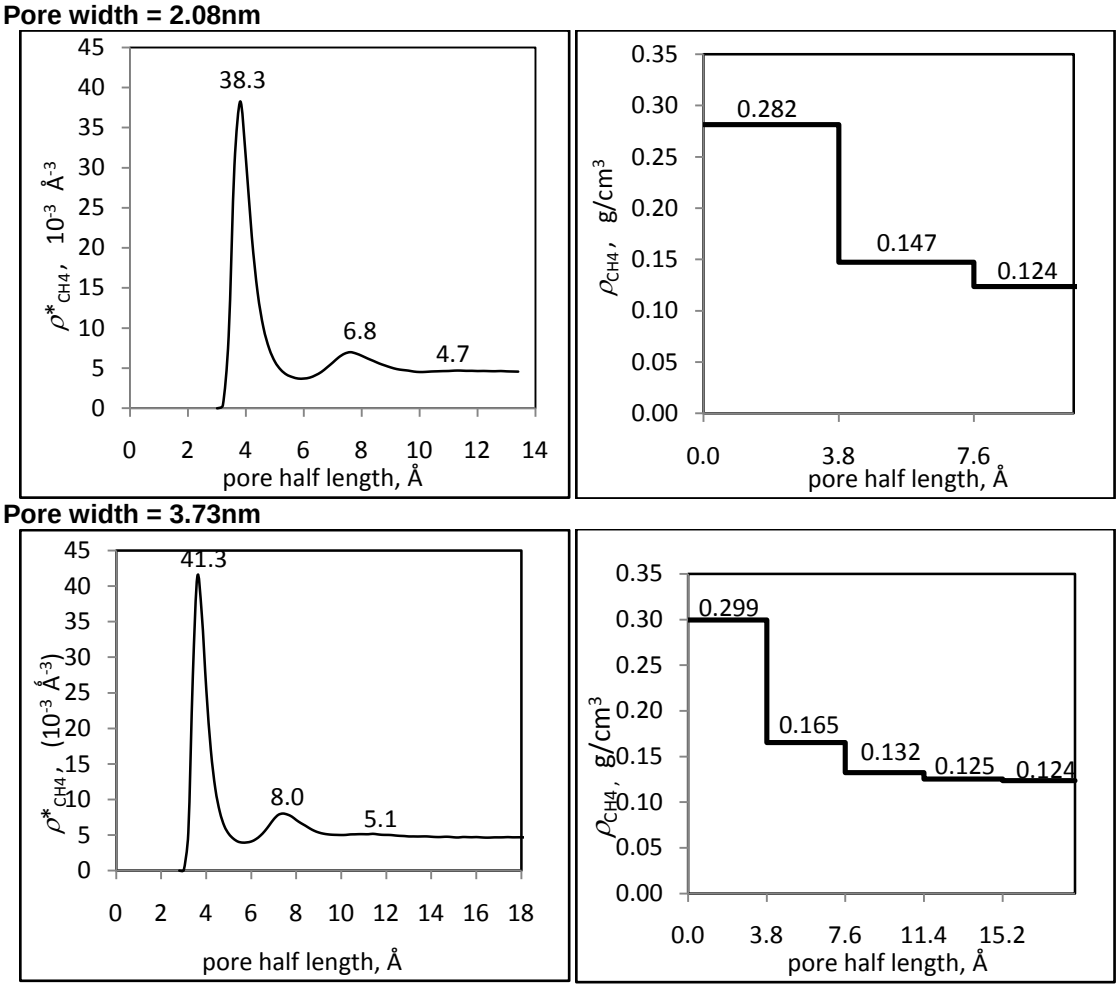

Fig. 28 - Number density (left) and discrete density (right) profiles for methane as a function of pore size at 176 °F (80°C). Density values are estimated at each 0.2 Å interval for the continuous density profile. Discrete density corresponds to molecular layer density for methane across the pore. The estimated pore pressure at the center of the pores is 3,043 psi.

Using a Langmuir model and the free phase density determined from NIST-SUPERTRAPP®, an equivalent monolayer density is calculated. Results are shown in **Table 5** and **Fig. 29** as a function of pressure in a 2.31 nm pore. Additionally, **Fig. 30**

shows the multilayer profile and equivalent single layer density for a 2.31 nm pore. The inclusion of this effect will be discussed later in the chapter.

$$\rho_s = 0.282 + (0.147\text{-}0.122) + (0.124\text{-}0.122) = 0.309 \text{ g/cm}^3.$$

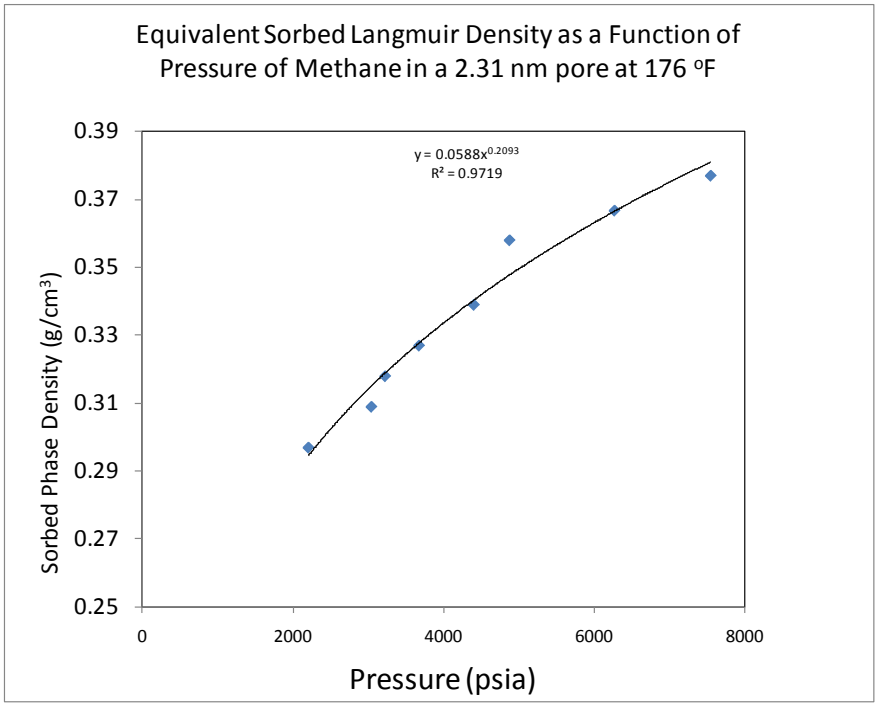

Fig. 29 - Equivalent sorbed phase density of methane using a single layer model as a function of pressure for a 2.31 nm pore at 176 °F. The sorbed phase density could be included in Eq. 19. Effects of this inclusion will be shown later in the chapter.

Pressure (psia)	Gas Phase Density (g/cm^3)	Equivalent Sorbed Phase Density (g/cm^3)
2206	0.0895	0.297
3043	0.122	0.309
3226	0.129	0.318
3676	0.144	0.327
4404	0.167	0.339
4878	0.179	0.358
6272	0.211	0.367
7550	0.233	0.377

Table 5 - Equivalent sorbed phase density of methane using a single layer model as a function of pressure for a 2.31 nm pore at 176 °F. The sorbed phase density could be included in Eq. 19. Effects of this inclusion will be shown later in the chapter.

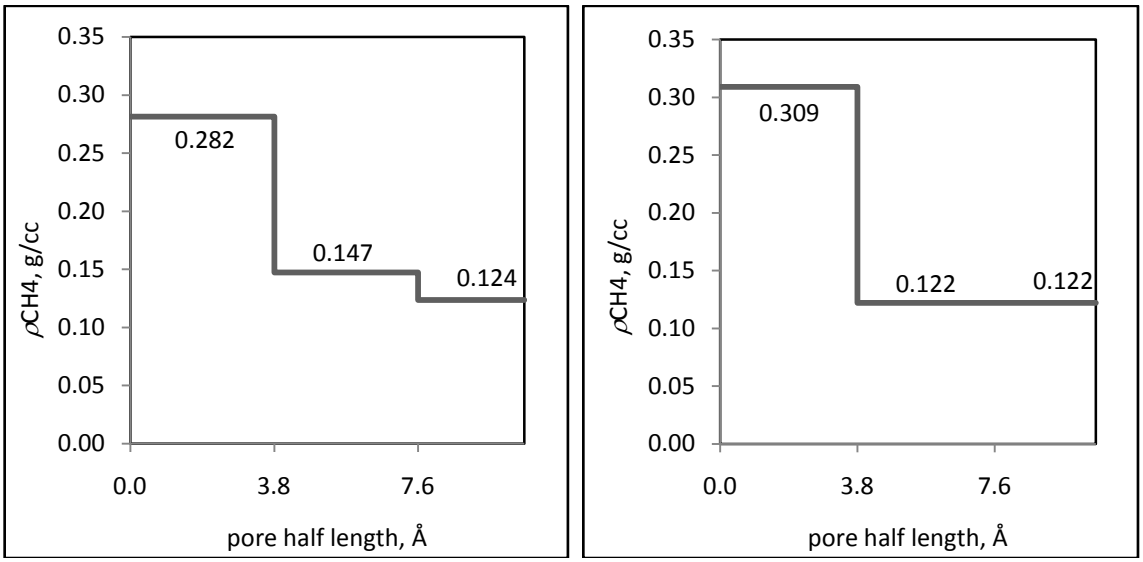

Fig. 30 - Discrete density (right) and equivalent monolayer (Langmuir) density (left) profile for methane at 176°F (80°C) in a 2.31 nm pore. The estimated pore pressure at the center of the pores is 3,043 psi.

The values determined for the sorbed phase density match well with the van der Waals co-volume constant at higher pressures, although it can be seen that the true density value is much more complicated because it is clearly a function of pressure and pore size. Diaz-Campos (2010) also performed simulations at different temperatures. **Fig. 31** shows some results for runs at three different temperatures; clear temperature dependence is displayed, however, temperature has less of an influence than pressure.

From **Fig. 29** a power relationship was used to correlate the sorbed phase density to the pore pressure. This relationship is shown in **Eq. 21**. The effects of using this equation along with the gas formation volume factor as a function of pressure will be investigated later in this chapter. This equation is only valid up to 8000 psia (the limits of the modeled data).

$$\rho_s = 0.0588\, p^{\,0.2093} \qquad \textbf{(21)}$$

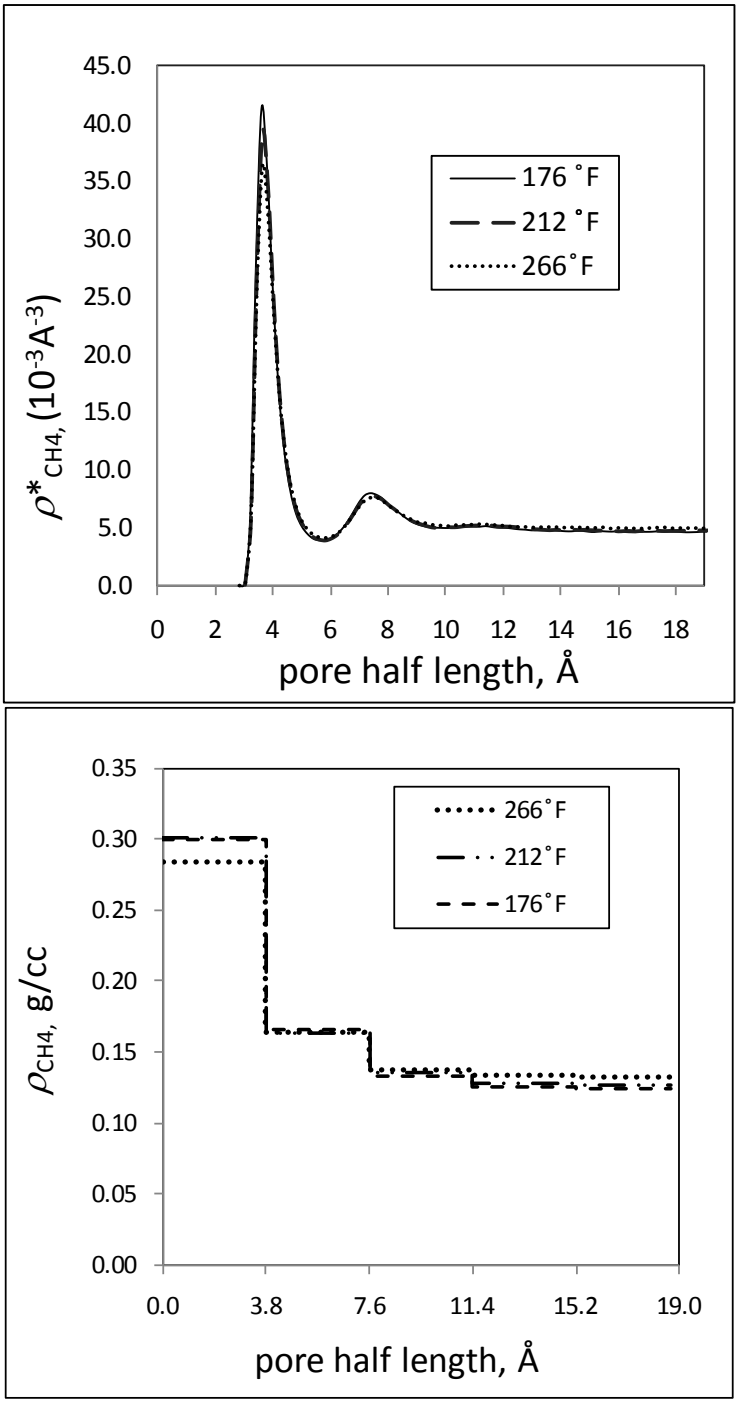

Fig. 31 - Number density (above) and discrete density profile (below) for methane at three different temperatures. A small temperature dependence was determined by Diaz-Campos (2010).

4.5 Results and Discussion

In order to quantify the pore-scale effects using the new methodology, the results of the old method is compared to the new method (both pressure dependent and constant model) on two shales. The first shale has a low sorbed gas volume while the second has a relatively high sorbed gas volume. Comparisons between multiple different sorbed phase densities are shown. Additionally, an example is shown as a function of pressure, where the sorbed phase density is kept constant compared to a value that is allowed to vary as **Eq. 21**. The rest of the parameters for the two shales are shown in the **Table 6** below. **Table 7** shows the different sorbed phase densities that will be used.

	Shale A: (low sorption capacity)	**Shale B: (high sorption capacity)**
ϕ	0.06	0.06
S_w	0.35	0.35
S_o	0	0
$\hat{M}$	16 lb/lb-mol	16 lb/lb-mol
G_{sL}	50 scf/ton	120 scf/ton
p	4000 psia	4000 psia
T	180 ^{o}F	180 ^{o}F
p_L	1150 psia	1800 psia
ρ_b	2.5 g/cm^3	2.5 g/cm^3
ρ_s	see Table 7	see Table 7

Table 6 - Shale properties for example gas-in-place calculation

Method	Sorbed Phase Density, ρ_s (g/cm^3)
van der Waals *b*	0.375
MD Simulation	0.33
f(p) from MD Simulation	**Eq. 21**

Table 7 - Sorbed phase density properties for example gas-in-place calculation

Results of applying and not applying the correction are shown in **Table 8** and **Table 9**. As can be seen there is not much difference between the various estimates of adsorbed densities, however, the absolute difference between applying the model and not applying the model is between 15% and 17% for a reduction in free gas pore space and 11% and 12% for total gas in place for Shale 'A' and 30-34% free gas pore space and 18-20% total gas-in-place for Shale 'B'. These are significant reductions and highlight the importance of the volumetric balance and correcting for the volume of pore space occupied by the adsorbed gas. It has been reported that some shales have S_w percentages lower than 10%, in these types of systems the sorbed phase may be a more important volumetric correction than water saturation.

		van der Waals	Molecular Simulation	MD Pressure Dependant	Old
ρ_s	g/cm^3	0.375	0.330	0.334	
G_f	scf/ton	99.0	96.8	97.0	115.1
Percentage of Uncorrected		86.0%	84.1%	84.3%	
G_s	scf/ton	38.8	38.8	38.8	38.8
G_{st}	scf/ton	137.8	135.6	135.8	153.9
Percentage of Uncorrected		89.5%	88.1%	88.2%	

Table 8 - Gas-in-place and percentage compared to the old method of determining gas-in-place for Shale 'A'.

		van der Waals	Molecular Simulation	MD Pressure Dependant	Old
ρ_s	g/cm^3	0.375	0.330	0.334	
G_f	scf/ton	80.8	76.1	76.5	115.1
Percentage of Uncorrected		70.2%	66.1%	66.5%	
G_s	scf/ton	82.8	82.8	82.8	82.8
G_{st}	scf/ton	163.5	158.8	159.3	197.9
Percentage of Uncorrected		82.6%	80.3%	80.5%	

Table 9 - Gas-in-place and percentage compared to the old method of determining gas-in-place for Shale 'B'.

Plots showing the free gas-in-place both corrected and uncorrected (G_f), sorbed gas-in-place (G_s), and total gas-in-place corrected and uncorrected (G_{st}) for both Shale 'A' and Shale 'B' are shown in **Fig 32** and **Fig 33**. In the plot for Shale 'A', it can be clearly seen that the model is consistent in that at very low pressures, where the effect of sorbed gas density should be negligible, the models overlay. Therefore, it is suggested that this model could be used in simulation or other analytical models where gas-in-place as a function of pressure is needed. **Fig. 34a** and **Fig. 34b** show the absolute differences as a function of pressure between the corrected and uncorrected volumetrics. For these examples the molecular simulation density of 0.330 g/cm^3 was used.

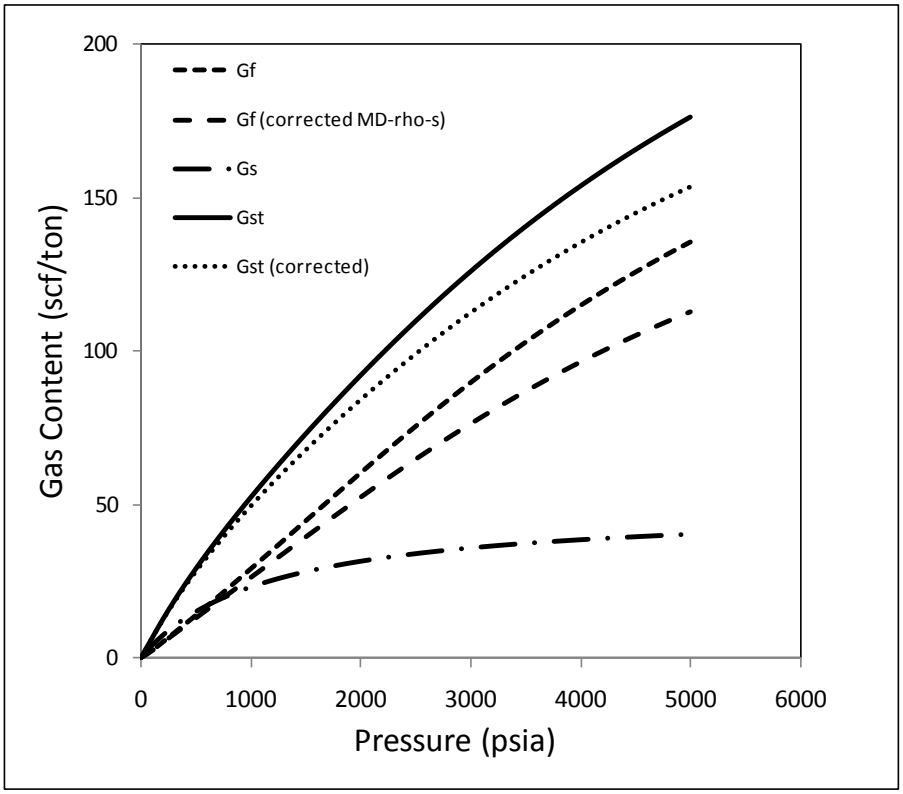

Fig. 32 - Shale 'A' corrected and uncorrected free, sorbed and total gas contents as a function of pressure.

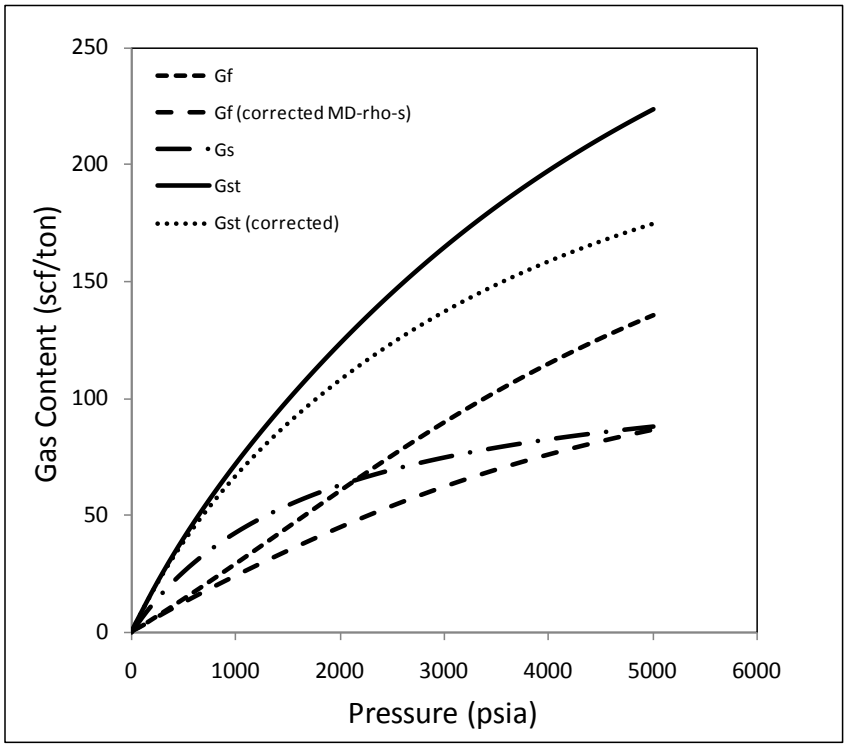

Fig. 33 - Shale 'B' corrected and uncorrected, free, sorbed and total gas contents as a function of pressure.

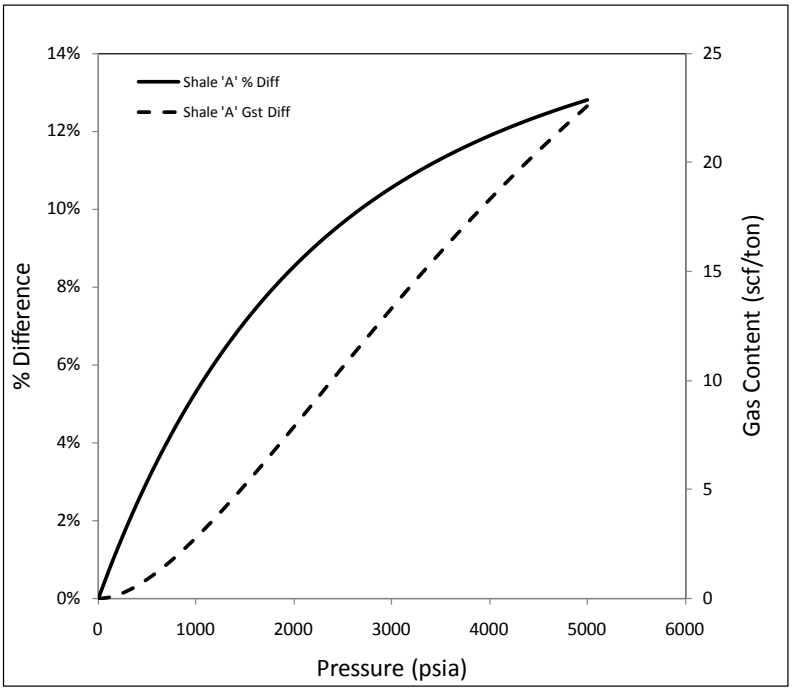

Fig. 34a - Shale 'A' percentage and absolute difference between the corrected and uncorrected gas-in-place calculations.

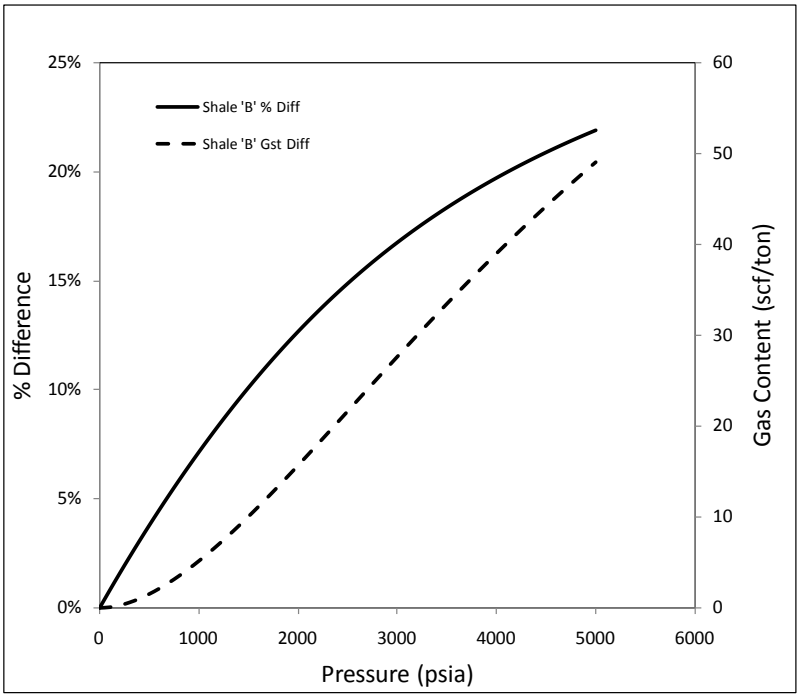

Fig. 34b - Shale 'B' percentage and absolute difference between the corrected and uncorrected gas-in-place calculations.

Additionally, the empirical relationship of sorbed density as a function of pressure (**Eq. 21**) was compared to the constant determined from molecular simulation. As can be seen in **Fig. 35** the difference is relatively small (+/- 1.5 scf/ton) compared to the size of correction shown if **Fig. 34a** and **Fig. 34b**.

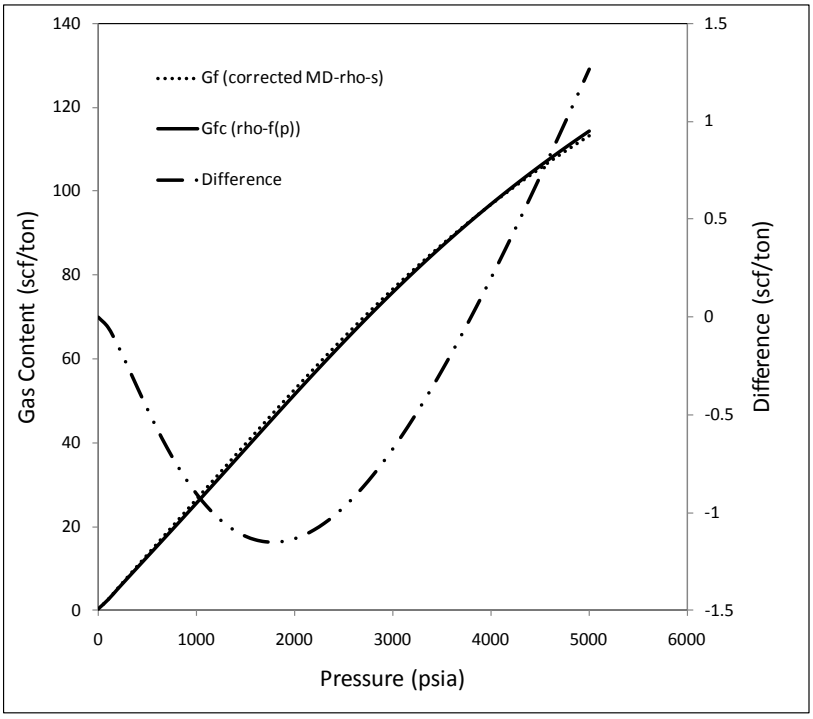

Fig. 35 - Shale 'A' corrected free gas content determined with a constant sorbed phase density and pressure dependent sorbed phase density. Notice there is not much difference in values compared to Fig. 34a.

In this chapter the following issues were addressed in regards to the volume available for free gas in organic shales.

- The sorbed phase follows Langmuir theory for most of the pores and that it takes up one-molecule thick portion of a pore, although there is a damped oscillation density profile with an increased density in the second layer. For a 100 nm pore, the volume is fairly insignificant; however, for pores on the order of a 1 nm, it is quite large.
- The current industry standard disregards the volume consumed by the sorbed phase, thus inadvertently overestimating the pore-volume available for free-gas storage. It was shown that **Eq. 19** is a more correct gas volume is calculation. Through MD simulation and Langmuir theory it was shown that the density for adsorbed methane typically equals to 0.33 g/cm^3. This value is based on numerical work using simple flat

organic pore wall surfaces. In small pores the adsorbed layer thickness will be affected by the roughness and curvature of the solid surface and the density will increase due to increased surface area of the wall. Further analysis using more complex pore wall structures is necessary. Additionally, an empirical relationship for the sorbed phase density as a function of pressure was shown.

- In the calculation of the gas in-place a dramatic change in the estimated gas in-place values due to volume adjustments was determined. This change in gas in-place persists even when the sorbed density values reported by other researchers, such as the liquid methane density of 0.4223g/cc corresponds to 1 atm and -161^{o}C (Mavor *et al.*, 2004) and of 0.374 g/cc (Haydel and Kobayashi, 1967).

In conclusion, a robust method that matches the local physics is presented to determine an estimate of the gas-in-place in organic-rich gas shale. In the next chapter a multi-component version of the model is developed and a thermodynamically consistent model is also evaluated.

4.6 A Note on Isotherm Correction

One assumption the method proposed in this section is that the density used to correct for the sorbed phase in the gas filled porosity is the density used to correct the raw Gibbs isotherm data to the Langmuir isotherm data. If the densities are not the same, then the Langmuir isotherm needs to be corrected back to the original data using **Eq. 15** with the original sorbed phase density used, and then re-corrected using the appropriate sorbed phase density. In the examples shown in section 4.4, the assumption is the isotherm

parameters and the correction use a consistent density. If the density is not consistent an overcorrection can occur.

For example, if the shale 'A' Langmuir isotherm was corrected from the raw Gibbs isotherm using a density of 0.4233 g/cm^3 and the appropriate density should have been 0.375 g/cm^3, the Langmuir isotherm parameters would be too low and the sorbed gas storage capacity would be low as well. Using a least squares fit to correct the isotherm parameters rather than a G_{sL} of 50 scf/ton and a p_L of 1150 psia, the new parameters after re-correcting the raw data would be a G_{sL} of 57.75 scf/ton and a p_L of 1490 psia. Using these parameters and **Eq. 19**, the new G_{st} would be 139.7 scf/ton rather than 137.8 scf/ton. This results in a 9.2% reduction in gas-in-place, rather than a 10.5% reduction. As one can see, the net change is more a function of just making the correction, rather than density correction value, although it is recommended to use consistent values to ensure accuracy. The details behind these calculations are presented in **Appendix B**.

CHAPTER V
ADSORPTION EFFECT ON GAS STORAGE IN SHALES - MULT-COMPONENT MODEL

Chapter IV showed that for gas reservoirs with a significant sorbed-phase component, the resource in place has often been overestimated due to a lack of material and voidage balance in the calculation of gas-in-place. In the example the overestimation was shown to be as high as 30%; however, it is theoretically possible to have even larger overestimations. Referring to the simple conceptual model that shows the pore and matrix system of shale is shown in **Fig 27**, the hashed region represents the effect that the sorbed phase on porosity. For the free gas and the sorbed portion of a fluid system, a single-component isotherm model was developed in chapter IV as shown in **Eq. 16** and **Eq. 19**. This is an oversimplification of the fluid system because in reality the natural gas is a multi-component fluid, i.e. consisting of a number of chemical species each with a distinct sorption affinity and varying contributions to the phase densities.

5.1 Multi-component Sorbed-phase Correction for the Void Volume

Shales have varying composition and phases within the reservoir. The type of fluid has been shown to vary from dry gas where the composition is fairly simple to areas where the fluid is a liquid within the reservoir. In dry gas areas, two or three components often account for more than 99% of the composition. In areas where the fluid is a liquid in the reservoir, more than 40 components are often seen. In many unconventional reservoirs there is a large transition zone between the dry gas and liquid areas. It is in this transition area, sometimes labeled as the wet gas window where a multi-component model is

specifically critical in order to better determine the resource in place and in what phase it resides in.

A multi-component adsorption model can be used to determine the composition and amount of an adsorbed phase. There are many multi-component adsorption models in the literature. The Extended Langmuir (EL) model is often the easiest to employ, although it is not thermodynamically consistent (Ritter and Yang, 1987). Other models include the Ideal Adsorbed Solution (IAS) and the 2D equation-of-state (2D EOS) models, which both are thermodynamically consistent (Zhou and Hall, 1994). Another model built primarily for coal is a combination of the Dubinin-Polanyi and vacancy solution methods (Clarkson, 2003). In this chapter the EL model will be utilized due to its wide usage across the petroleum industry, although any other adsorption model could be substituted in its place.

Previously the pore volume taken up by the sorbed phase, ϕ_a, for a single component fluid system has been defined by **Eq. 16** in shale gas units. In this equation, the single-component isotherm could be replaced by any of the multi-component isotherms (placed into proper units) to yield a multi-component gas-in-place. **Eq. 22** is the EL model equation and for a single component can be shown to be equal to **Eq. 10b**.

$$G_s = \sum_{i=1}^{n} G_{sLi} \frac{y_i p}{p_{Li}\left(1+\sum_{j=1}^{n} y_j \frac{p}{p_{Lj}}\right)} \qquad \textbf{(22)}$$

Here the Langmuir parameters G_{sLi} and p_{Li} are measured in the laboratory using pure *i*-component. Substituting **Eq. 22** into **Eq. 16** yields **Eq. 23a** and **Eq. 23b**, which is the

sorbed phase porosity of the mixture and sorbed phase saturation of the mixture respectively:

$$\phi_{a,mix} = 1.318 \times 10^{-6} \hat{M} \frac{\rho_b}{\rho_{s,mix}} \left[\sum_{i=1}^{n} G_{sLi} \frac{y_i p}{p_{Li} \left(1 + \sum_{j=1}^{n} y_j \frac{p}{p_{Lj}} \right)} \right] \quad \textbf{(23a)}$$

$$S_{a,mix} = \frac{\phi_{a,mix}}{\phi} \quad \textbf{(23b)}$$

In this equation the apparent molecular weight, $\hat{M}$, and the adsorbed-phase density, $\rho_{s,mix}$, of the mixture needs to be calculated using mixing rules. The calculation of the adsorbed-phase density is difficult, however, because the fluids are typically supercritical. In this chapter it will be shown that the recommended method is to use the van der Waals co-volume constant *b*, for the liquid phase density values. Here the mixing is based on mole fraction-weighted arithmetic averaging also widely-known as Kay's mixture rule.

5.2 Estimation of Sorbed-phase Gas Content of a Gas Mixture

Sorbed phase content of a mixture is estimated using **Eq. 22**, i.e., EL model. As stated earlier, although this model is not thermodynamically consistent it yields satisfactory results and is easy to implement since there are no iterations involved in the calculations. An example calculation is presented next. **Table 10** contains the gas phase mole fraction of an example shale gas. **Table 11** contains the standard shale petrophysical and reservoir parameters that are used in calculating the gas-in-place.

	units	methane	carbon dioxide	ethane	propane	butane +	mixture
yi	fraction	0.86	0.01	0.10	0.02	0.01	1.0000

Table 10 - Example gas phase mole fraction of a liquid rich gas shale.

Parameter	Value	Unit
Sw	0.35	
ϕ	0.055	
Pressure	4000	psia
Temperature	180	^{o}F
Free Gas Gravity	0.74	
z	0.891008	
Bg	0.00403	r-vol/vol
ρ_b	2.5	g/cm^3

Table 11 - Example shale petrophysical and fluid properties for gas-in-place determination.

In order to calculate the EL isotherm, the individual component isotherms are also needed. Isotherms of methane are available and measured for most gas shales. Higher order carbon isotherms such as C_2, and C_{O2} are also fairly common. However, measurements of the single-component C_{3+} isotherms are often difficult to measure due to very low dew points of the fluid systems. For the examples here, the C_3 isotherms were available, although, C_4+ isotherms were estimated based on C_1, C_2, and C_3 carbon number trends of G_L and P_L. **Fig. 36** shows the trends of the carbon number values on a

100% carbon basis. In this example, isotherms were grouped within a +/- 15 ^{o}F temperature window in order to get a statistically significant sample. **Table 12** contains the single component Langmuir isotherm model values for the example shale. These values along with the mole fractions given in **Table 10** are used in **Eq. 22** for the determination of the Extended Langmuir isotherm.

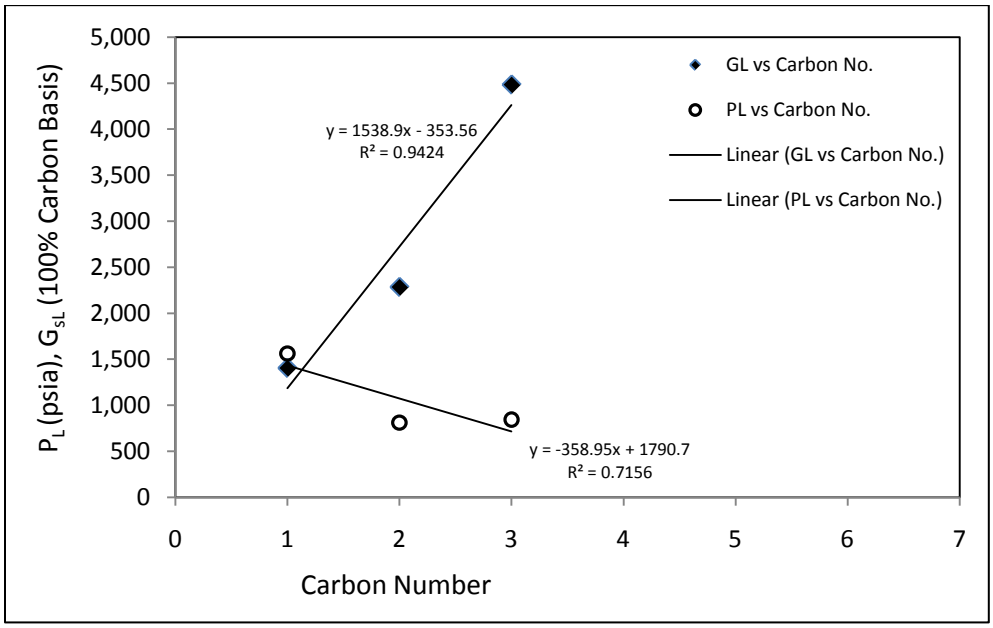

Fig. 36 – Trends of Langmuir Constants (G_{sL} and p_L) on a 100% carbon basis compared to carbon number.

		C1	C2	C3	C4+ *	CO_2
G_{sL}	(scf/ton)	56	91	179	232	145
P_L	(psia)	1,562	811	844	355	836

As Received Basis with 4% TOC content (*modeled)

Table 12 – Trends of Langmuir Constants (G_{sL} and p_L) on a 100% Carbon basis compared to Carbon number.

Fig. 37 shows the adsorption model curves for the single-component Langmuir and the multi-component Extended-Langmuir models. It is important to note that the gas content of the EL isotherm is 37% greater than the single-component methane isotherm.

For shale gas reservoirs where there exists a rich gas, EL, or other multi-component adsorption model, should be utilized to best estimate the sorbed amount and the nature of the gas-in-place.

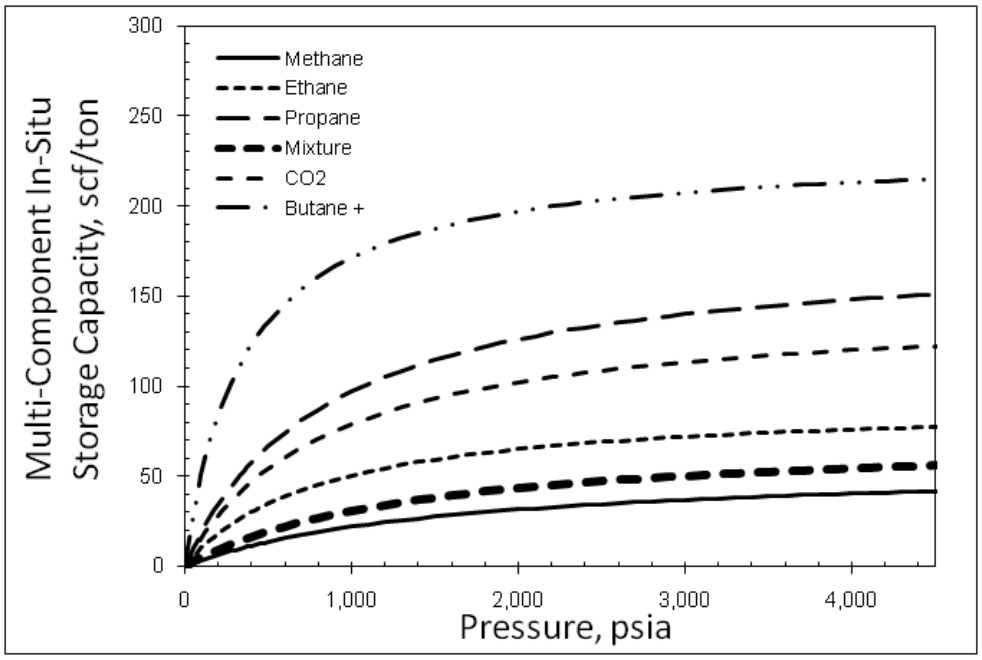

Fig. 37 – Laboratory measured single-component and EL isotherms for typical naturally occurring gases. Notice that considering natural gases as methane only greatly underestimates the sorbed storage capacity of the shale samples.

Additionally, the EL model gives the sorbed phase mole fractions which is needed to calculated the sorbed-phase average molecular weight and sorbed phase density values. The sorbed-phase mole fractions are shown in **Table 13**.

	units	methane	carbon dioxide	ethane	propane	butane +	mixture
xi	fraction	0.5654	0.0317	0.2058	0.0776	0.1195	1.0000

Table 13 - Example sorbed phase mole fraction of a liquid rich gas shale.

As stated earlier, even though the EL model is the most extensively used for coalbed methane and shale gas systems due to its ease of use and utility, it is not

thermodynamically consistent. Thermodynamic consistency requires that the sorption limit (Langmuir Volume) be equal for all components, which is clearly not the case for most shale gas systems. Because the approach developed here for shale gas-in-place calculations is general and any adsorption model may be used, a thermodynamically consistent adsorption model was investigated. In the literature there is a variety of adsorption models that have been applied, including, but limited to, the Ideal Adsorbed Solution (IAS) Theory (Myers and Prausnitz, 1965), 2-D Equation-of-State approaches (Hall *et al.*, 1994) and the hybrid Potential Theory/Vacancy Solution approach (Clarkson, 2003). For this work a comparison of the EL and IAS models was performed on a simpler binary system of gases.

The IAS theory (Myers and Prausnitz, 1965) was derived using the assumption that the adsorbed mixture behaves like an ideal adsorbed solution. This is analogous to Raoult's law for bulk solutions. Activity coefficients of the adsorbed solution are assumed to be unity, although this assumption can be relaxed for strongly non-ideal mixtures. The equilibrium between the gaseous and sorbed fractions is given by:

$$p y_i = p_i^{\circ}(\pi) x_i \qquad \textbf{(24)}$$

where p_i° is the gas (vapor) pressure of the pure component adsorbed at the same temperature and spreading pressure as the solution. Fugacities may be substituted for pressures in **Eq. 24** to account for gas phase non-idealities. The spreading pressure for the pure components may be determined through integration of the Gibbs adsorption isotherm to the vapor pressure of the pure component by **Eq. 24b**, p_i°:

$$\pi_i^* = \frac{\pi_i A}{RT} = \int_0^{P_i^\circ} \frac{n(p)}{p} dp \qquad \textbf{(24b)}$$

where *n(p)* is the pure component adsorption isotherm. The spreading pressure (π) may be defined as the reduction in surface tension of a surface due to the spreading of the adsorbate over the surface (Ruthven, 1984). Any pure component isotherm equation may be used to evaluate **Eq. 24b**, which is a desirable feature of the IAS approach. In this work, the Langmuir isotherm for the individual components was utilized to allow for direct comparison with the EL model, but it should be noted that IAS fits to experimental data may be improved if more accurate single component isotherms are applied (Clarkson and Bustin, 2000). Using the Langmuir model for single component modeling has the advantage that the integral in **Eq. 24b** yields a simple algebraic equation, whereas application of other pure component adsorption models may require **Eq. 24b** to be evaluated numerically (Clarkson and Bustin, 2000). Mole fraction constraints include:

$$\sum_{i=1}^{nc} x_i = 1 \quad ; \quad \sum_{i=1}^{nc} y_i = 1 \qquad \textbf{(24c)}$$

The total amount of adsorbed gas in the mixture (for an ideal solution) is given by:

$$\frac{1}{n_t} = \sum_{i=1}^{nc} \frac{x_i}{n_i^o} \qquad \textbf{(24d)}$$

The actual amount of each component adsorbed in the mixture is given by:

$$n_i = n_t x_i \qquad \textbf{(24e)}$$

The prediction of the sorbed phase compositions determined by IAS was compared to that determined by EL. This was performed on binary mixtures of components; they are C1:C2, C1:CO_2, C1:C3 and C1:C4+. Methane is the primary component in all cases. **Fig. 38** shows a series of four comparison plots of phase equilibrium compositions of the binary mixtures using both the IAS and EAL models. Predictions were made at both 4,000 psia and 1,000 psia for the IAS model. It should be noted that the two models for all mixtures differ significantly and better agreement is seen at low pressures. In general, the EL model predicts more methane (weakly adsorbing component) in sorbed phase than the IAS model. The EL model predicts that the compositions do not change with pressure (therefore the reason for only one pressure on each plot). This phenomenon is believed to be inaccurate.

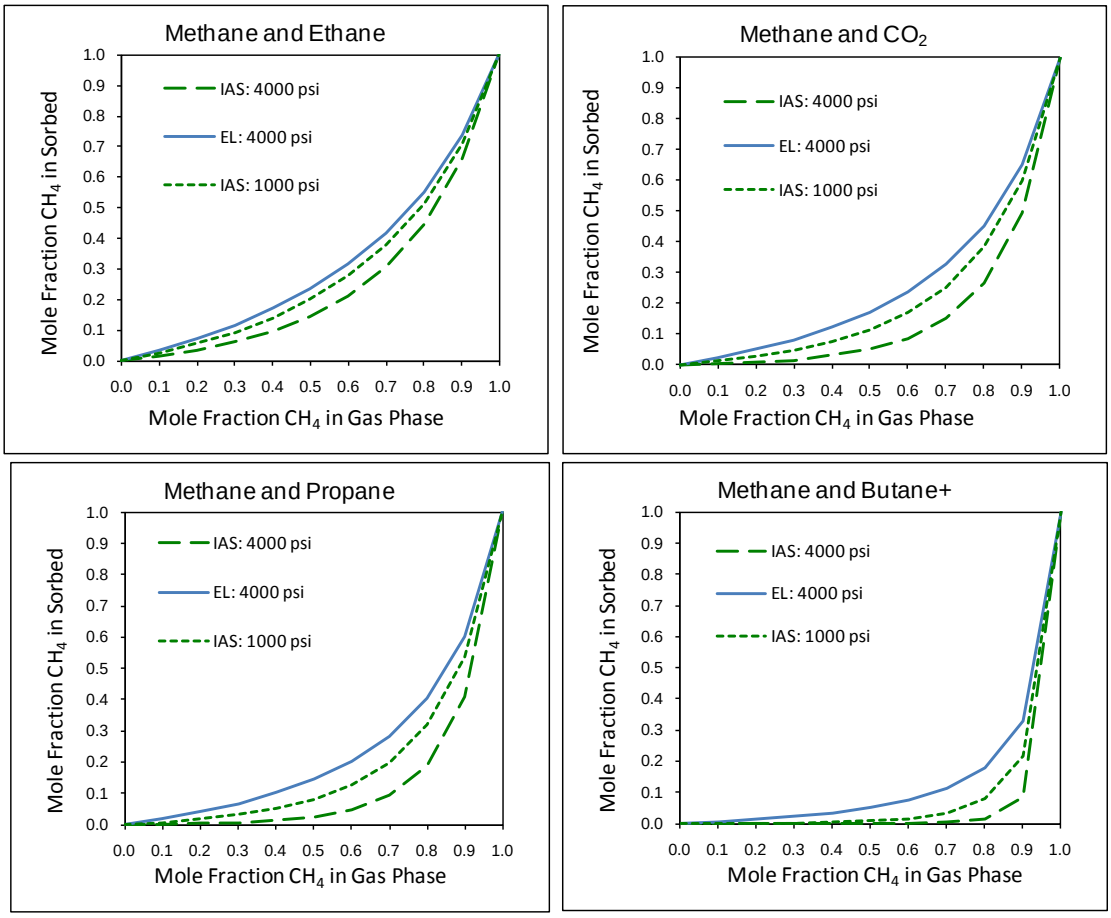

Fig. 38 - Equilibrium composition diagrams for the various binary mixtures showing predictions of EL and IAS models. IAS predictions for two different total pressures are compared.

A useful way to express the relative adsorption of components in an adsorption system is through the calculation of a separation factor (Ruthven, 1984). The separation factor, or selectivity ratio, is shown in **Eq. 24f** for a binary gas adsorption system.

$$\alpha_{ij} = \frac{(x/y)_i}{(x/y)_j} \qquad \textbf{(24f)}$$

The separation factor of the EL model is simply the ratio of the adsorption equilibrium constants for the pure component isotherms (Ruthven, 1984) and is independent of pressure or composition. **Fig. 39** shows the separation factor calculations for each of the

mixtures. It is clear that C4+ exhibits much stronger relative adsorption compared to the other components as would be expected due to its greater molecular weight.

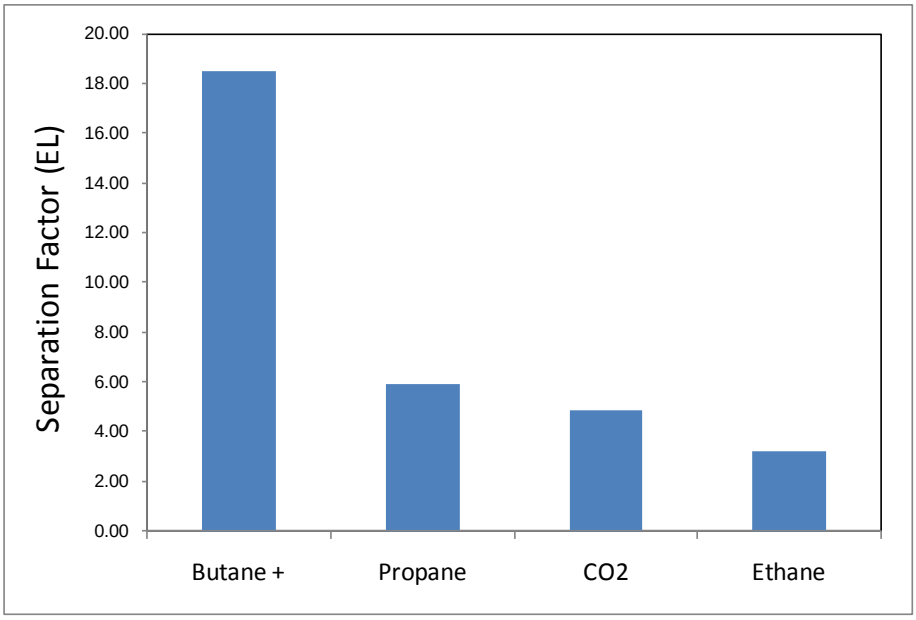

Fig. 39 - Separation factor calculations for each binary mixture using the EL model. The separation factor of an EL model is not a function of pressure or composition.

The assumption of a constant separation factor shown in the EL model is not, however, necessarily accurate for all systems (Ruthven, 1984). An increasing selectivity for the most strongly adsorbed component with decreasing concentration of that component is generally observed (Myers, 1968). In contrast and shown in **Fig. 40**, the IAS model does predict a pressure- and composition-dependent separation factor. However, it must be noted that the trend in predicted separation factor is uncertain without comparison to actual measured multi-component isotherm data. Clarkson and Bustin (2000) noted that trends in predicted separation factor for CBM varied depending on the selection of pure component isotherm in the IAS calculations.

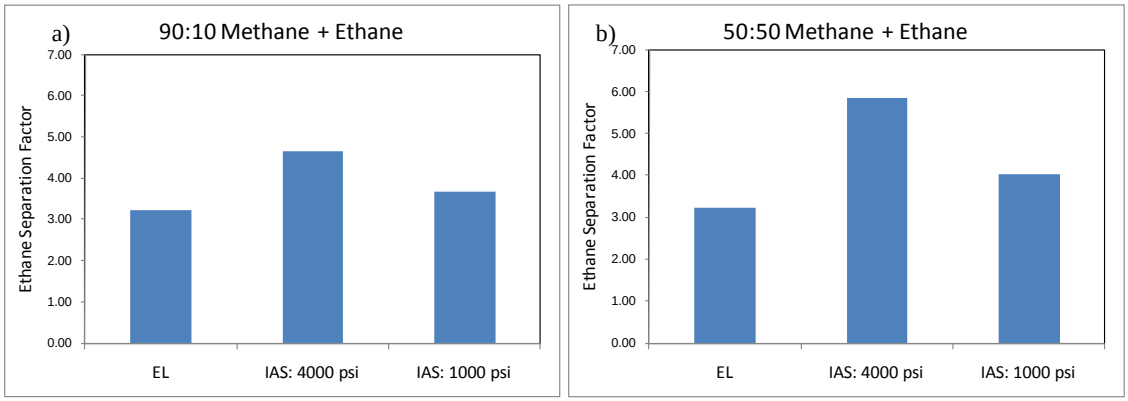

Fig. 40 - Separation factor calculations for methane-ethane binary mixture using the EL and IAS models. (a) is for 90% methane in free-gas phase, (b) is for 50% methane in free-gas phase.

Fig. 41 compares the predicted total adsorption of the EL and IAS models for C1:C2 and C1:C4. Two different gas compositions were calculated and compared; first a 90:10 free-gas concentration and second, a 50:50 free-gas concentration. Additionally, the calculations were performed at 4000 psi and 1000 psi. The greatest differences in predictions occur at 4000 psi. Furthermore, the differences become greater with the C1:C4 compositions. Looking at **Fig. 38**, explains this observation as the greatest differences in the model predictions occur at the higher pressures. In general, the IAS model appears to consistently predict higher total adsorption when compared to the EL model.

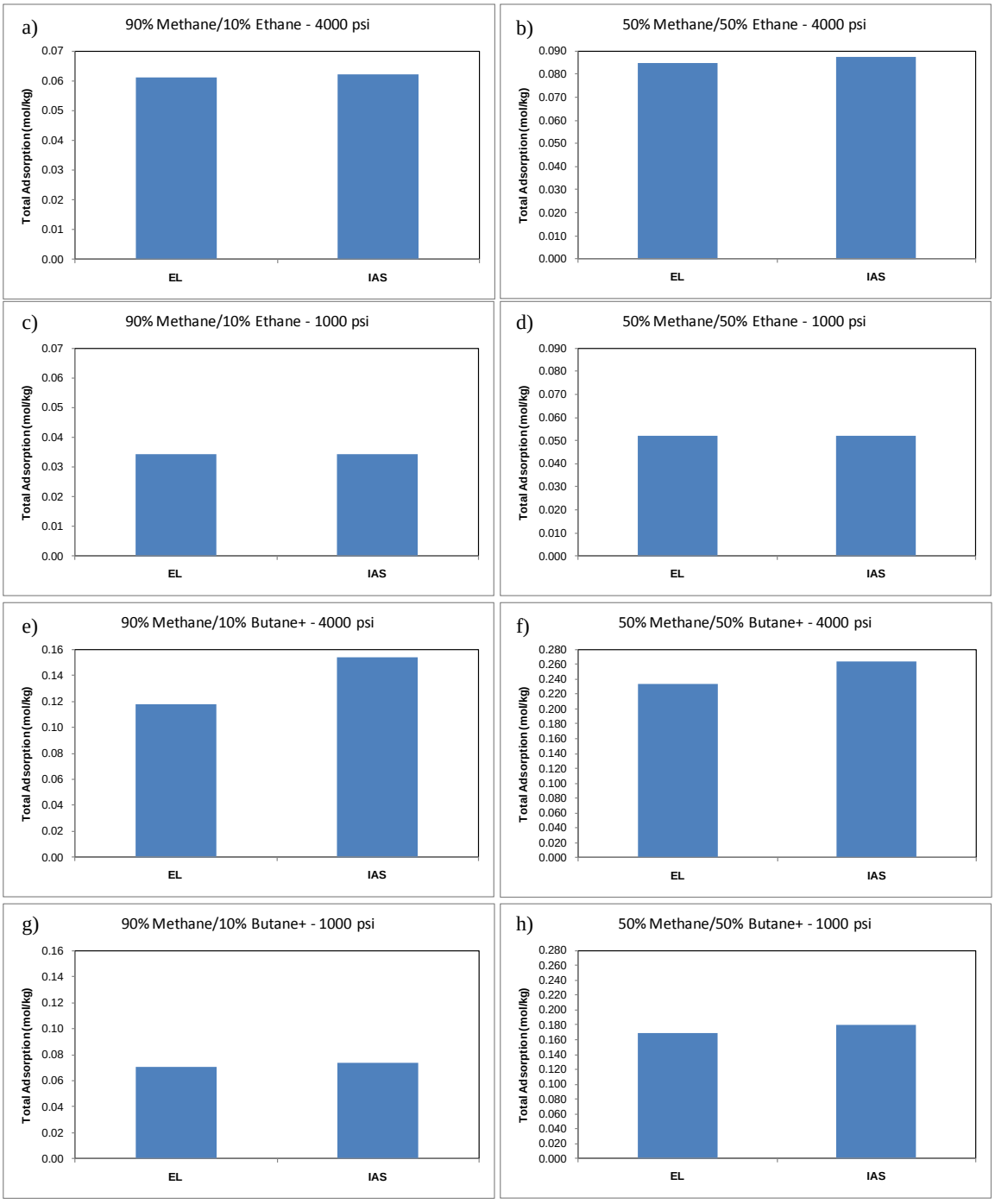

Fig. 41 - Model-predicted total adsorption (n_t) for C1:C2 [(a) - (d)] and C1:C4 [(e) - (h)]mixture assuming 90:10 and 50:50 free-gas concentrations respectively at 4000 psia and 1000 psia. It is important to note the large difference in sorption capacity of the 90:10 C1:C4 mixture at 4000 psia determined by the models. However, experimental matching should be performed to confirm the difference.

5.3 Estimation of Sorbed Phase Density of a Gas Mixture

van der Waals equation of state was one of the earliest attempts to investigate deviations from ideal gas and to predict the behavior of real gases:

$$\left(p + \frac{a'}{V^2}\right)(V - b') = RT \qquad \textbf{(25)}$$

In **Eq. 25,** V represents molar volume of the real gas. Subtraction of co-volume constant b' from the molar volume is the attempt to account for the small but finite volume of gas molecules which has been ignored in the ideal gas theory. Dubinin (1960) suggested that the adsorbate density is related to this co-volume constant, and in chapter 4 it was shown that as the pressure increased the sorbed gas density approached this value. Here, a methodology is introduced to predict the constant for natural gas mixtures. It is experimentally shown for a pure substance at the critical point (p_c, T_c), that the first and second order derivatives of gas pressure with respect to molar volume are equal to zero (McCain, 1990):

$$\left(\frac{\partial p}{\partial V}\right)_{T_c} = 0 \qquad \textbf{(26)}$$

$$\left(\frac{\partial^2 p}{\partial V^2}\right)_{T_c} = 0 \qquad \textbf{(27)}$$

These two empirical relationships can be used to derive expression for the co-volume constant (as well as constant a', which accounts for the intermolecular forces associated with real gases) of a particular chemical species in terms of the critical temperature and critical pressure of that species. At the critical point, the following are true:

$$\left(p_c + \frac{a'}{V_c^2}\right)\left(V_c^2 - b'\right) = RT_c \tag{28}$$

$$\left(\frac{\partial p}{\partial V}\right)_{T_c} = \frac{RT_c}{\left(V_c - b'\right)^2} + \frac{2a'}{V_c} = 0 \tag{29}$$

$$\left(\frac{\partial^2 p}{\partial V^2}\right)_{T_c} = \frac{2RT_c}{\left(V_c - b'\right)^3} - \frac{6a'}{V_c^4} = 0 \tag{30}$$

These three equations can be solved for the van der Waal's constants *a* and *b*, which results in:

$$b' = \frac{RT_c}{8p_c} \tag{31}$$

$$\rho_s = \frac{\hat{M}}{b'} \tag{32}$$

The obtained co-volume constant, *b'*, has the units of ft^3/lb-mole and as shown previously its reciprocal value multiplied with the molecular weight of the chemical species will be used as the value of the sorbed-phase density of that chemical species **Eq. 32**. **Table 14** shows the estimated values of sorbed-phase density for naturally occurring gases. Note

	methane	ethane	propane	n-buthane	iso-butane	carbon dioxide	mixture
Pc, psia	666.4	706.5	616.0	550.6	527.9	1071.0	668.4
Tc, F	-116.67	89.92	206.08	305.62	274.46	87.91	5.9918
a, psia (cu-ft)^2/(lb mole)^2	8594.8	20798.5	34995.9	51729.2	49651.2	13619.9	15786.5
b, cu-ft/lb mole	0.6911	1.0442	1.4506	1.8654	1.8664	0.6863	0.9353
M, lbm/lbm mole	16	30	44	58	58	44	26.96
$\rho_{s,mix}$, g/cc	0.371	0.460	0.486	0.498	0.498	1.027	0.434
$\rho_{s,mix}$, g/cc	-	-	-	-	-	-	0.462

Table 14 - Thermodynamic and adsorption properties of pure gases.

that the density increases with the molecular weight. In order to estimate the sorbed-phase density of a mixture of gas, it is first recommend to estimate the pseudo-critical

properties (p_{pc}, T_{pc}) of the mixture using Kay's mixing rule, where the sorbed-phase mole fractions are used in place of the gas phase mole fractions:

$$p_{pc} = \sum_{i}^{n} x_i p_{ci} \tag{33}$$

(34)

Then, these pseudo-properties are used in **Eq. 31**, where the T_c and p_c are substituted with the T_{pc} and p_{pc} respectively. As an alternative, if the composition data is available for the sorbed phase, then mixture density could be obtained directly from the pure sorbed-phase density values using the Kay's mixture rule as given by **Eq. 35**:

$$\rho_{s,mix} = \sum_{i}^{n} x_i \rho_s \tag{35}$$

The last column of **Table 14** compares the estimated values of sorbed phase density for a typical shale gas mixture using **Eq. 31** and **Eq. 32** and compared to the pure component method using **Eq. 35**. The composition of the gas mixture used in the calculations is given in **Table 15**.

	units	methane	carbon dioxide	ethane	propane	butane +	mixture
yi	fraction	0.86	0.01	0.10	0.02	0.01	1.0000
xi	fraction	0.5654	0.0317	0.2058	0.0776	0.1195	1.0000

Table 15 - Composition of the gas mixture used in the calculations.

5.4 Estimation of Gas-in-place Considering Multi-component Adsorption Layer Effects using Extended Langmuir

In this section the previously calculated and modeled parameters will be used to estimate the gas-in-place using the EL model. **Eq. 22**, **Eq. 23a**, and **Eq. 18b** will be used to predict the free gas-in-place, the sorbed porosity fraction and the sorbed gas-in-place, respectively. The result is the generalized equation for gas-in-place in a system with both sorbed and fee gas.

$$G_{st} = 32.0368\frac{\phi(1-S_w)-1.318\times10^{-6}\hat{M}\dfrac{\rho_b}{\rho_{s,mix}}\left[\displaystyle\sum_{i=1}^{n}\frac{G_{sLi}y_i p}{p_{Li}\left(1+\displaystyle\sum_{j=1}^{n}y_j\frac{p}{p_{Lj}}\right)}\right]}{\rho_b B_g} + \sum_{i=1}^{n}\frac{G_{sLi}y_i p}{p_{Li}\left(1+\displaystyle\sum_{j=1}^{n}y_j\frac{p}{p_{Lj}}\right)} \quad \textbf{(36)}$$

Gas shales are the most common form of this type of system. Again, the first term on the right-hand-side represents the adsorption layer corrected free gas volume, whereas the second term corresponds to the sorbed-gas volume. One of the convenient results of the EL equation is that with a given y_i, mole fraction of component i in the gas phase, a given x_i, mole fraction of component i in the sorbed phase is calculated. **Table 16** shows the mole fraction of both free and sorbed phases.

	units	methane	carbon dioxide	ethane	propane	butane +	mixture
yi	fraction	0.86	0.01	0.10	0.02	0.01	1.0000
xi	fraction	0.5654	0.0317	0.2058	0.0776	0.1195	1.0000
zi	fraction	0.7343	0.0193	0.1451	0.0446	0.0567	1.0000

Table 16 - The vapor, sorbed and total mole fraction of the fluid in the reservoir.

Additionally, a total mole fraction z_i is shown. The total mole fraction of the system was then put into a standard PVT package at reservoir pressure and temperature. The phase diagram in **Fig. 42** is the result. In this phase diagram, due to the uncertainty in physical properties of the C4+ (pseudo-component) fraction, it has been modeled in three different ways. The three cases give average properties of the C4+ fraction values of an average C5, an average C6 and an average C7. It can clearly be seen from this phase diagram that the reservoir fluid should be completely in the vapor phase for all three cases only as the crichondotherm and crichondobar (with the exception of the C7 fluid) are well below the reservoir conditions.

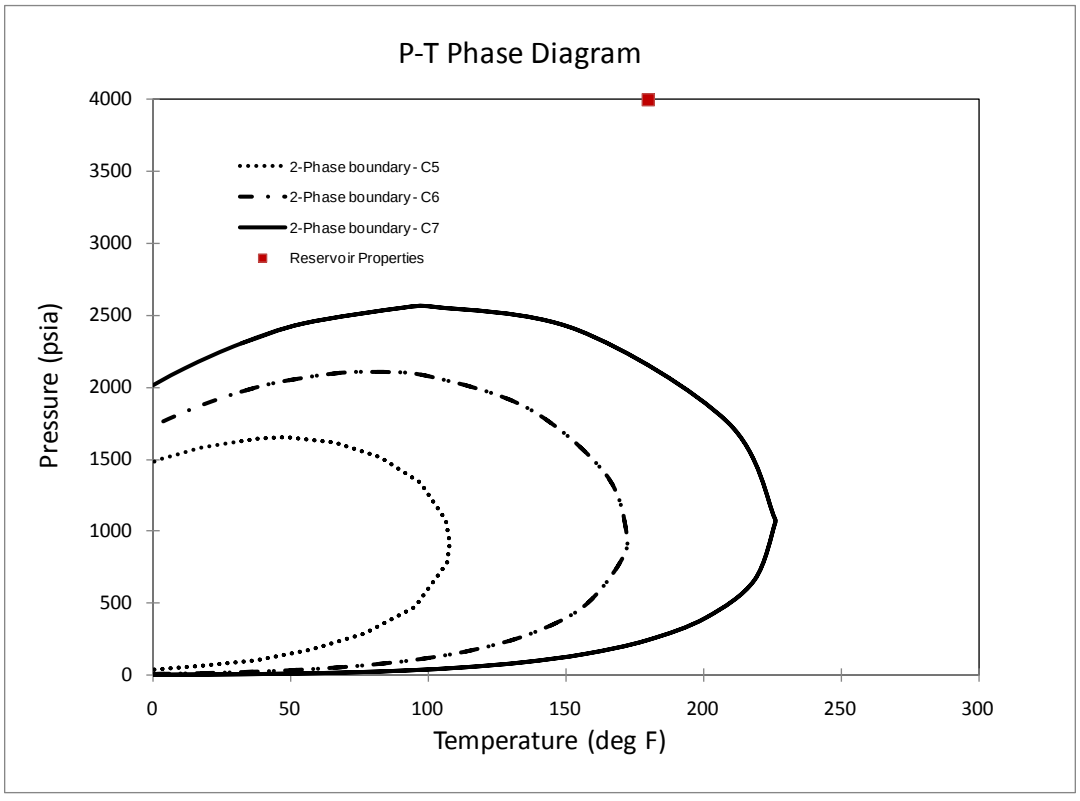

Fig. 42 - Phase envelope of the fluid used in the example calculations. The diagram shows that the bulk fluid used is gas under the reservoir pressure and temperature conditions. Three different C4+ fraction models were tested. Characterizing the C4+ with equivalent C5, C6 and C7 physical properties.

5.5 Comparisons of Adsorbed Gas Storage, Adsorbed Fractional Gas Composition, and Adsorbed Gas Density Estimates Between EL and IAS Multi-component Adsorption Models

A comparison was performed in order to bracket the differences between the IAS and EL models. Two different gas combinations (C1:C2 and C1:C4) each with two different compositions (90:10 and 50:50) were compared at 4000 psia and 1000 psia. Given the results in **Fig. 41**, the total adsorbed gas storage capacity values were determined for each gas mixture and pressure using both the EL and IAS models. Adsorbed gas storage capacity values were converted to scf/ton for standard comparison. As previously discussed and shown in **Fig. 39** the EL adsorbed mole fractions are not pressure dependent. This is different than the calculated IAS adsorbed mole fractions which vary based on free gas pressure. Using van der Waal's co-volume constants, calculated adsorbed mole fractions of each gas species, and Kay's mixing rules the adsorbed phase density of the gas mixtures at both 1000 and 4000 psia were determined for the gas mixtures. The results are presented in **Tables 17-20**.

Gas Species	IAS Total Adsorbed Gas Storage Capacity	EL Total Adsorbed Gas Storage Capacity	IAS Adsorbed Gas Mole Fraction	EL Adsorbed Gas Mole Fraction	van Der Waal co-Volume Constant Pure Fluid Adsorbed Density	IAS Adsorbed Gas Density	EL Adsorbed Gas Density
-	scf/ton	scf/ton	-	-	g/cc	g/cc	g/cc
90% CH_4 : 10% C_2H_6 Gas Mix, 1000 psi							
CH_4	25.92	25.85	0.710	0.742	0.371	0.397	0.394
C_2H_6			0.290	0.258	0.460		
90% CH_4 : 10% C_2H_6 Gas Mix, 4000 psi							
CH_4	47.09	46.28	0.659	0.742	0.371	0.401	0.394
C_2H_6			0.341	0.258	0.460		

Table 17 - Comparison of the total adsorbed gas storage capacity, adsorbed gas mole fractions, and multi-component adsorbed phase densities for the EL and IAS mixed gas adsorption models based upon a 90:10 gas mixture of methane and ethane, respectively.

Gas Species	IAS Total Adsorbed Gas Storage Capacity	EL Total Adsorbed Gas Storage Capacity	IAS Adsorbed Gas Mole Fraction	EL Adsorbed Gas Mole Fraction	van Der Waal co-Volume Constant Pure Fluid Adsorbed Density	IAS Adsorbed Gas Density	EL Adsorbed Gas Density
-	scf/ton	scf/ton	-	-	g/cc	g/cc	g/cc
50% CH_4 : 50% C_2H_6 Gas Mix, 1000 psi							
CH_4	39.39	39.14	0.199	0.242	0.371	0.442	0.438
C_2H_6			0.801	0.758	0.460		
50% CH_4 : 50% C_2H_6 Gas Mix, 4000 psi							
CH_4	65.97	63.89	0.146	0.242	0.371	0.447	0.438
C_2H_6			0.854	0.758	0.460		

Table 18 - Comparison of the total adsorbed gas storage capacity, adsorbed gas mole fractions, and multi-component adsorbed phase densities for the EL and IAS mixed gas adsorption models based upon a 50:50 gas mixture of methane and ethane, respectively.

Gas Species	IAS Total Adsorbed Gas Storage Capacity	EL Total Adsorbed Gas Storage Capacity	IAS Adsorbed Gas Mole Fraction	EL Adsorbed Gas Mole Fraction	van Der Waal co-Volume Constant Pure Fluid Adsorbed Density	IAS Adsorbed Gas Density	EL Adsorbed Gas Density
-	scf/ton	scf/ton	-	-	g/cc	g/cc	g/cc
90% CH_4 : 10% C_4H_{10} Gas Mix, 1000 psi							
CH_4	54.54	51.91	0.199	0.242	0.371	0.442	0.438
C_4H_{10}			0.801	0.758	0.460		
90% CH_4 : 10% C_4H_{10} Gas Mix, 4000 psi							
CH_4	113.39	87.05	0.146	0.242	0.371	0.447	0.438
C_4H_{10}			0.854	0.758	0.460		

Table 19 - Comparison of the total adsorbed gas storage capacity, adsorbed gas mole fractions, and multi-component adsorbed phase densities for the EL and IAS mixed gas adsorption models based upon a 90:10 gas mixture of methane and butane+, respectively.

Gas Species	IAS Total Adsorbed Gas Storage Capacity	EL Total Adsorbed Gas Storage Capacity	IAS Adsorbed Gas Mole Fraction	EL Adsorbed Gas Mole Fraction	van Der Waal co-Volume Constant Pure Fluid Adsorbed Density	IAS Adsorbed Gas Density	EL Adsorbed Gas Density
-	scf/ton	scf/ton	-	-	g/cc	g/cc	g/cc
50% CH_4 : 50% C_4H_{10} Gas Mix, 1000 psi							
CH_4	135.47	127.31	0.710	0.742	0.371	0.397	0.394
C_4H_{10}			0.290	0.258	0.460		
50% CH_4 : 50% C_4H_{10} Gas Mix, 4000 psi							
CH_4	197.92	175.55	0.659	0.742	0.371	0.401	0.394
C_4H_{10}			0.341	0.258	0.460		

Table 20 - Comparison of the total adsorbed gas storage capacity, adsorbed gas mole fractions, and multi-component adsorbed phase densities for the EL and IAS mixed gas adsorption models based upon a 50:50 gas mixture of methane and butane+, respectively.

5.6 Results and Discussion

It has been shown that the composition of the reservoir fluid has an effect on the amount of gas stored in the reservoir. However, there are uncertainties in the sorption model. The primary reason for the uncertainties is the lack of experimental data. This is an area that should be investigated further and is beyond the scope of this dissertation. In this section there are two main comparisons. First, comparisons of the estimated gas-in-place values and expected recoveries were performed using the petrophysical and reservoir data shown in **Table 10** and **Table 11** and the more widely used EL model. The following cases were considered:

1. No sorbed phase density
2. Single-component fluid (methane) case with Langmuir isotherm and adsorption layer effects included using **Eq 19**.
3. Multi-component fluid case with EL and the adsorption layer effects included using **Eq. 36** and using different sorbed density values (from **Eq. 32** and **Eq. 35**)

Second, a comparison between the IAS and EL models for GIP in a reservoir is performed with a binary system with 90:10 ratio of C1:C4 in the free phase. Values are taken from **Table 19** and a comparison of gas-in-place is performed at 4000 psia. This table was shown because of the four examples shown in **Tables 17-20**, it showed the greatest difference in sorbed gas storage capacity prediction between the EL and IAS models.

The results, tabulated in **Table 21**, show that the gas-in-place is overestimated significantly if adsorption volume is not considered. It can also be seen that in this case

whether the single- or multi-component composition is used, the total gas in place is fairly close (within 2% of each other). However, where the gas is stored is greatly different. The percentage of sorbed to free gas changes significantly depending upon if a multi-component or single component isotherm is used. This has potentially large impacts on the recoverable gas-in-place, since sorbed gas requires abandonment pressures to be much lower in order to recover. The difference between the free gas-in-place for this case when a single component isotherm is used compared to a multi-component isotherm is used changes by nearly 20%. This effect must be considered when determining the recoverable reserves within reservoirs where there is a significant amount of gas contained in the higher molecular weight (stronger adsorbing) hydrocarbons.

ϕ_a - single component isotherm	0.0065
ϕ_a - EL isotherm (ρ_s = 0.434 g/cc)	0.0113
ϕ_a - EL isotherm (ρ_s = 0.462 g/cc)	0.0107
G_f - EL isotherm (ρ_s = 0.434 g/cc)	77.61 scf/ton
G_f - EL isotherm (ρ_s = 0.462 g/cc)	79.80 scf/ton
G_f - single component methane isotherm	93.14 scf/ton
G_f - sorbed phase density of 0.0 g/cc	113.68 scf/ton
G_s - EL isotherm	55.41 scf/ton
G_s - single component isotherm	40.42 scf/ton
G_{st} - EL isotherm (ρ_s = 0.434 g/cc)	133.02 scf/ton
G_{st} - EL isotherm (ρ_s = 0.462 g/cc)	135.21 scf/ton
G_{st} - single component methane isotherm	133.56 scf/ton
G_{st} - sorbed phase density of 0.0 g/cc	154.10 scf/ton

Table 21 - Sorbed phase porosity, free, sorbed and total gas-in-place.

A plot showing recovery in terms of scf/ton as a function of average abandonment pressure is shown in **Fig. 43**. As can be seen in this graph, although both gas-in-place determination methods yield similar in-place volumes at 4000 psia of nearly133 scf/ton, the recovery as a function of pressure is different. The maximum difference of nearly 8 scf/ton, which is almost 6% of the in-place volumes occurs at around 1200 psia. Coincidently this happens to be near the abandonment pressure. Therefore, the recovery factor could be estimated 6% high, strictly as a function of gas composition.

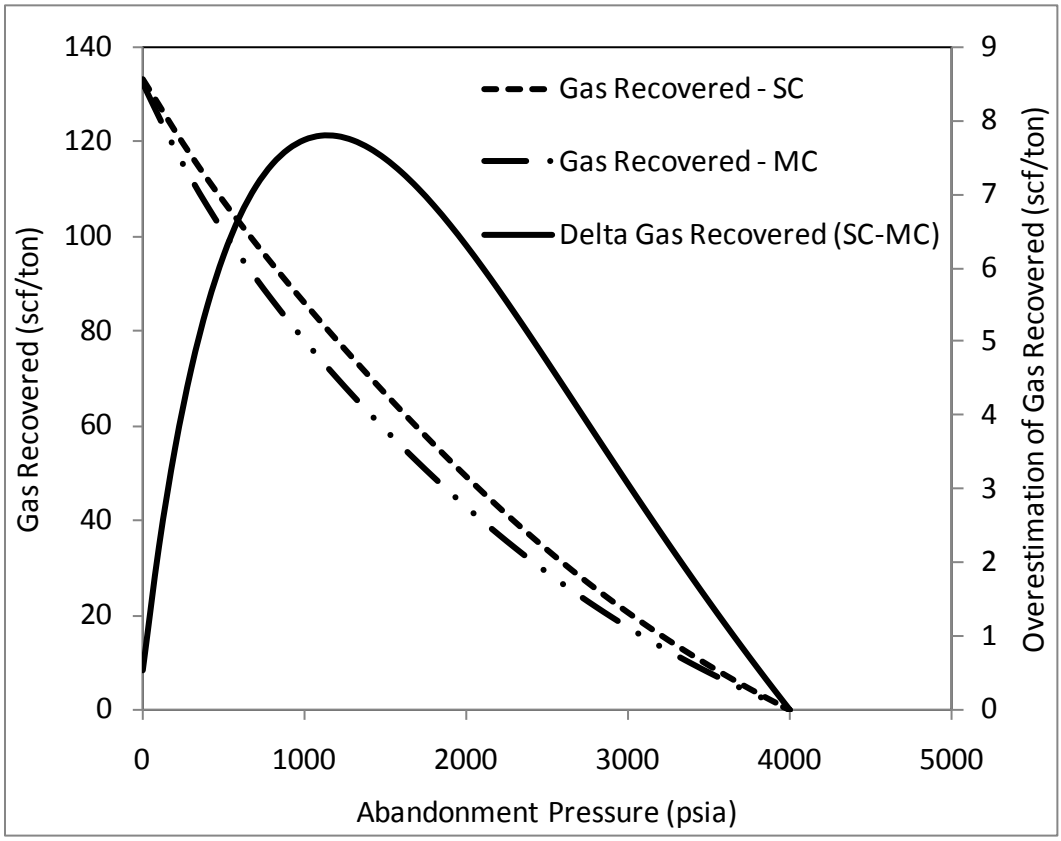

Fig. 43 -Recovery as a function of abandonment pressure. The multi-component model (MC) predicts a lower recovery by up to 8 scf/ton (or 6% recovery factor) compared to the single-component model.

Next a comparison was performed using a 90:10 gas composition of a simple C1:C4 binary system. **Table 22** shows the reservoir properties used in the comparison.

Variable	Unit	Value
Reservoir Properties		
Pressure	psia	4000
Temperature	°F	180
Net Thickness	feet	300
Drainage Area	acres	640
Rock Properties		
Total Porosity	fraction of bulk volume	0.06
Water Saturation	fraction of porosity	0.35
Oil Saturation	fraction of porosity	0.00
Total Organi Carbon	weight fraction	0.04
Bulk Density	g/cc	2.50
z Factor		0.91
Bg	rcf/scf	0.00410

Table 22 - Reservoir properties used for the comparison utilizing the IAS and EL models of total gas-in-place with 90:10 ratio of C1:C4 in the free gas.

As can be seen due to differences in the predicted value of sorbed gas storage capacity of the binary system shown in **Table 19**, **Table 23** actually shows in increase, even given the previously mentioned corrections due to the increase in predicted adsorbed gas storage capacity using the IAS model. This helps to highlight the fact that experimental work needs to be performed, specifically, for richer gases.

Pressure	Free Gas Storage Capacity	Adsorbed Storage Capacity	M of Adsorbed Gas	Adsorbed Gas Porosity	Gas Corrected Free Gas Storage	Un-corrected Total Storage Capacity	Corrected Total Storage Capacity	Un-corrected GIP	Corrrected GIP
psia	scf/ton	scf/ton	lbs moles	fraction	scf/ton	scf/ton	scf/ton	Bcf/Section	
IAS Model With a Free Gas Composition of 90% Methane : 10% Butane									
4000	121.77	113.39	20.2	0.0068	100.69	235.16	214.07	153.41	139.65
EL Model With a Free Gas Composition of 90% Methane : 10% Butane									
4000	121.77	87.05	20.2	0.0053	105.27	208.83	192.32	136.23	125.46

Table 23 - Estimations of gas-in-place using both the EL and IAS models of a simple 90:10, C1:C4 binary system. Note that the corrected gas-in-place estimation using the IAS model predicts more gas-in-place than the uncorrected value using the EL model. This highlights the need for more research into the storage capacity and the models used to predict storage capacity.

In conclusion, it is found that the multi-component nature of the shale gas introduces new implications into the gas-in-place estimations. Results indicate that, the total gas storage capacity predictions are influenced by the gas mixture composition. Additionally, it was shown that the models used to predict storage capacity can lead to uncertainty in the predictions, in the example the estimations are different by nearly 8% at the expected abandonment pressure. Therefore, more research, specifically, experimental and modeling research is needed in the light of these findings.

CHAPTER VI
MACRO-SCALE FULL-CYCLE DECLINE CURVE MODEL

This chapter presents a new methodology to accurately forecast future production in a tight/shale gas reservoir. Decline curve analysis (DCA) has been a handy tool for reservoir engineers to predict the future performance of a well. In general, DCA methods fall into three different categories: analytical, empirical or a combination of the two ("hybrid").

The empirical method described in the classic work by Arps (1945) is still the standard tool used by reservoir engineers to determine future reservoir behavior. Two new empirical methods have been introduced by Ilk *et al.* (2008) and Valkó (2009), Valkó and Lee (2010), the Power-Law (PL) and The Stretched Exponential Decline (SEPD), respectively. The main difference between Arps' method and the PL/SEPD methods is that the new methods allow the *b* factor to vary in time and decline with the production.

Analytical methods for DCA have also been discussed. Significant advances have been made in the development of analytical methods for analyzing pressure- and rate-transient behavior of multi-fractured, horizontal-wells (MFHW), for both conventional and unconventional; select examples include the work of van Kruysdijk and Dullaert (1989), Larsen and Hegre (1991), and Raghavan *et al.* (1997) for conventional reservoirs, and Medeiros *et al.* (2008), Ozkan *et al.* (2009), and Bello and Wattenbarger (2009) for unconventional reservoirs.

Recently, the use of "hybrid" forecasting techniques, which combine analytical methods for forecasting transient and transitional flow, with empirical methods for

forecasting boundary-dominated flow, have been investigated for MFHW. Fetkovich (1980) was the first to create a hybrid method for analyzing oil well production. He combined analytical solutions for constant pressure transient (radial) flow of liquids with the empirical Arps decline curves for boundary-dominated flow. The results were dimensionless type-curves. The seminal work of Fetkovich in the 1980's and 1990's provided guidance on the appropriate *b*-value to apply during boundary-dominated flow, depending on drive mechanism, reservoir fluid, reservoir heterogeneity and operating conditions (drawdown). However, the Fetkovich type-curves are only strictly applicable for slightly-stimulated wells exhibiting radial flow, which usually is not the case for MFHW. Carter (1985) later expanded this to hydraulically fractured wells. Recognizing that transient linear flow is the dominant flow-regime for MFHW, Bello and Wattenbarger (2010) and Nobakht *et al.* (2010) used the slope of the square-root time plot to yield a forecast for transient linear flow, and then applied the Arps hyperbolic decline forecast for boundary-dominated flow. The method described by Nobakht assumed that the reservoir width is defined by the length of the hydraulic fracture. In his work an innovative method for estimating the start of boundary-dominated flow was provided. The methodology does not rely on an estimate of matrix permeability (often elusive for tight formations because of the difficulty in measurement), fracture half-length (x_f), or fracture half width. It will be shown in this chapter that this is true for a system where all hydraulic fractures are the same length.

Bello and Wattenbarger (2009) developed a method for forecasting transient linear flow in shale gas reservoirs that also includes skin. The drawdown correction

introduced by Ibrahim and Wattenbarger (2006) was used to “correct” the slope of the square-root of time plot. The Bello and Wattenbarger (2009) method was used by Al-Ahmadi *et al.* (2010), combined with an analytical method (using material balance) for forecasting boundary-dominated flow, in order to history-match and forecast shale gas wells. Nobakht and Mattar (2010) introduced a slightly different methodology to account for skin. In their methodology skin can be early-time deviation from linear flow behavior, due to flow convergence, multi-phase flow in the fracture or low fracture conductivity.

In this chapter, the use of hybrid methods for forecasting MFHW, for cases where the hydraulic fractures are of equal and unequal length is investigated. For fractures of equal length, i.e. a homogeneous system, the method of Bello and Wattenbarger (2009) for forecasting transient linear flow combined with Arps decline for late-time (boundary dominated flow), using a procedure similar to Nobakht *et al.* (2010) is shown. This method is extended to that of heterogeneous cases (unequal fracture lengths). Then it is compared to a simple "hybrid" DCA method to understand the impact on b-value after fractures have interfered. Finally, we discuss a workflow for the optimization of development of a tight/shale gas reservoir.

6.1 Hybrid Model - Analytical and Empirical Model Foundation

Bello and Wattenbarger (2010) suggested that the dominant linear flow period associated with MFHW completed in shale gas reservoirs is matrix linear flow to the induced/natural fracture system. It is assumed in this work, and similar to assumptions in previous studies of tight gas reservoirs (Wattenbarger *et al.*, 1998, Ibrahim and Wattenbarger, 2006), that all flow is perpendicular to the fracture and does not extend beyond the tips of the fractures. The reasoning behind this is that when the reservoir permeability is very small, the fracture length defines the drainage area (Carlson and Mercer, 1989; Mayerhoffer *et al.*, 2006; Bello and Wattenbarger, 2008). It is further assumed that the transient within the fracture (bi-linear flow period of flow) should not be the focus of analysis (although deviation from pure linear flow is accounted for with skin) and that the well has constant flowing pressure.

A diagram of the flow model is shown in **Fig. 44**, where 3D map and cross-sectional views are shown. The Linear Flow Analysis plot (LFA) [i.e., a plot of pseudo-pressure normalized reciprocal rate ($[p_{pi} - p_{pwf}]/q_g$) versus the square root of time ($t^{1/2}$)] yields a straight line on Cartesian paper during the transient (infinite acting flow) period for the reservoir geometry shown in **Fig. 44**. The slope of this line can be analyzed to determine the product of fracture half length (x_f) and square root of matrix permeability ($k_m^{1/2}$). The proper straight line for this purpose is drawn during the period that the log-log plot of $q_g/(p_{pi} - p_{pwf})$ versus t forms a half-slope. Real data will often appear to form a straight line with a positive intercept that can be associated with an additional pressure drop due to skin (a combination of a finite-conductivity fracture, fracture-face

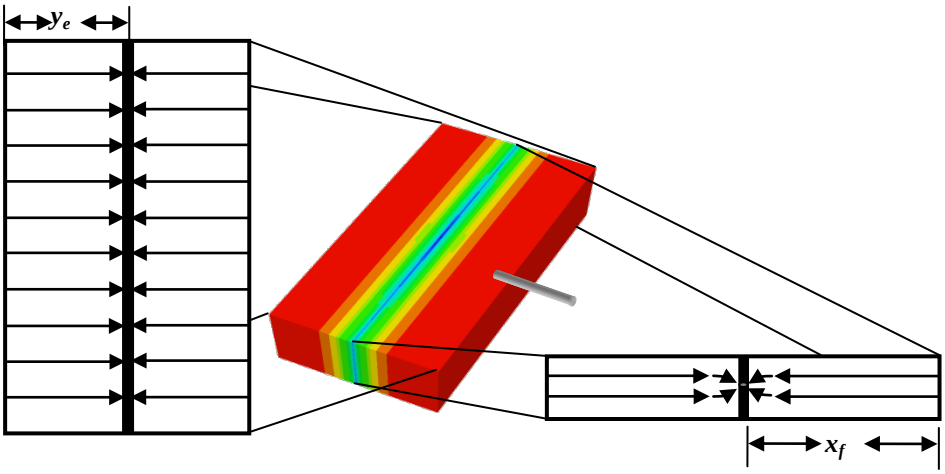

Fig. 44 – Map, 3D, and Cross-sectional view of analytical and numerical model. This model accounts for an additional pressure drop due to skin, whether that be convergence, multiphase flow or fracture face damage. Also, a main assumption of the model is there is no flow from beyond the fracture tips. Definitions for x_f and y_e are shown, where x_f is the fracture half length distance and y_e is the distance between the fracture and the boundary.

skin, or multi-phase flow). This additional pressure drop may cause the log-log plot of $q_g/(p_{pi} - p_{pwf})$ versus t to not form a half slope during linear flow (Nobakht and Mattar, 2010).

Assuming that the well is producing under constant flowing pressure condition, the equation describing the straight line on the square root time plot can be represented by **Eq. 37** (Ibrahim and Wattenbarger, 2006).

$$\frac{\left|p_{pi} - p_{pwf})\right|}{q_g} = \tilde{m}\sqrt{t} \qquad \textbf{(37)}$$

The observed slope is related to rock and completion properties by **Eq. 38** (Ibrahim and Wattenbarger, 2006).

$$\sqrt{k_m}A_{cm} = f_{cp}\frac{1262T}{\sqrt{(\phi\mu c_t)_m}}\frac{1}{\tilde{m}} \qquad \textbf{(38)}$$

where:

$$f_{cp} = 1 - 0.0852 D_D - 0.0857 D_D^2$$

and

$$D_D = \frac{\lfloor p_{pi} - p_{pwf} \rfloor}{p_{pi}}$$

Ibrahim and Wattenbarger (2006) incorporated the empirically derived drawdown correction (f_{cp}) to adjust the slope of the curve to give the correct reservoir parameters determined from analyzing reservoir simulation runs.

If a skin is present, Bello and Wattenbarger (2009) showed that the LFA plot can be described by **Eq. 39** below.

$$\frac{\lfloor p_{pi} - p_{pwf} \rfloor}{q_g} = \tilde{m}\sqrt{t} + \frac{Int}{1 + \frac{0.45\tilde{m}\sqrt{t}}{Int}} \qquad \textbf{(39)}$$

This equation describes early-time behavior for transient linear flow in the presence of skin. However, at large times, **Eq. 39** reduces to **Eq. 37** and the interpretation technique embodied in **Eq. 38** can still be employed.

The linear flow model described by **Eq. 39** is valid for the infinite acting portion of flow. The end of the infinite acting time, when the pressure transient reaches a boundary can also be determined. The assumption is that the boundary is at the distance halfway between the fractures. Section 6.3 of this chapter discusses the reasoning behind this assumption through the use of a "mine-back" image log experiment to see the evidence of a bi-wing hydraulic fracture system. The boundary time is a function of reservoir diffusivity and the distance between fracture clusters. The distance between clusters is noted as y_e and is pictured in **Fig. 44**. One can assume reservoir diffusivity (or

more simply reservoir permeability) then determine the time at which transient flow ends. This time is denoted as t_{ehs}, or the time at the end of half slope, where there is a deviation from a straight line on the LFA plot and is shown in **Eq. 40**.

$$t_{ehs} = \left(\frac{y_e}{0.159}\right)^2 \mu c_t \left(\frac{\phi}{k}\right) \quad \textbf{(40)}$$

In this model, boundary-dominated flow begins immediately after t_{ehs}. The results of Nobakht *et al.* (2010) and the simulation results found here indicate that gas rates after t_{ehs} can be approximated by the Arps equation with a *b* factor of approximately 0.5. Rates after t_{ehs} can therefore be described by **Eq. 41** and **Eq. 42** (Nobakht *et al.*, 2010). It must be noted that the skin in Nobakht's equation and that of Bello and Wattenbarger (2009)

$$D_{ehs} = \frac{1}{\tilde{m}\sqrt{t_{ehs}} + b''} \times \frac{\tilde{m}}{2\sqrt{t_{ehs}}} \quad \textbf{(41)}$$

$$q_g = \frac{q_{ehs}}{\left[1 + bD_{ehs}\left(t - t_{ehs}\right)\right]^{1/b}} \quad \textbf{(42)}$$

are not the same. In Nobakht's method, *b'* is a constant on the LFA plot, whereas in Bello and Wattenbarger (2009) it is a decreasing function with time. The differences beyond this observation will not be discussed in this dissertation. In the next step, a number of numerical simulations were conducted. The numerical model is similar to the one shown in **Fig. 44**. This is a single layer (2D), element of symmetry model with a single hydraulic fracture. The hydraulic fracture has a constant conductivity (infinite) and is filled with water. The reservoir is a homogenous, single mobile phase system with constant permeability. The reservoir properties are shown in **Table 24**. In this model, the y_e parameter was varied from 25 feet to 250 feet (50 feet to 500 feet fracture perforation

cluster). Straight-line relative permeabilities were used for the fluids in the hydraulic fracture. **Fig. 45** shows the LFA plot for the same reservoir with varying y_e's. **Table 25** shows the model varying y_e's, and the associated t_{ehs}'s.

Model Properties		
y_e	25 to 250	ft
Depth	7,000	ft
ϕ	0.06	
S_w	0.30	
p_i	3,500	psi
p_{wf}	300	psi
k_m	0.0001	md
h	300	ft
x_f	500	ft
$k_f w$	10	md-ft

Table 24 – Numerical and analytical model properties.

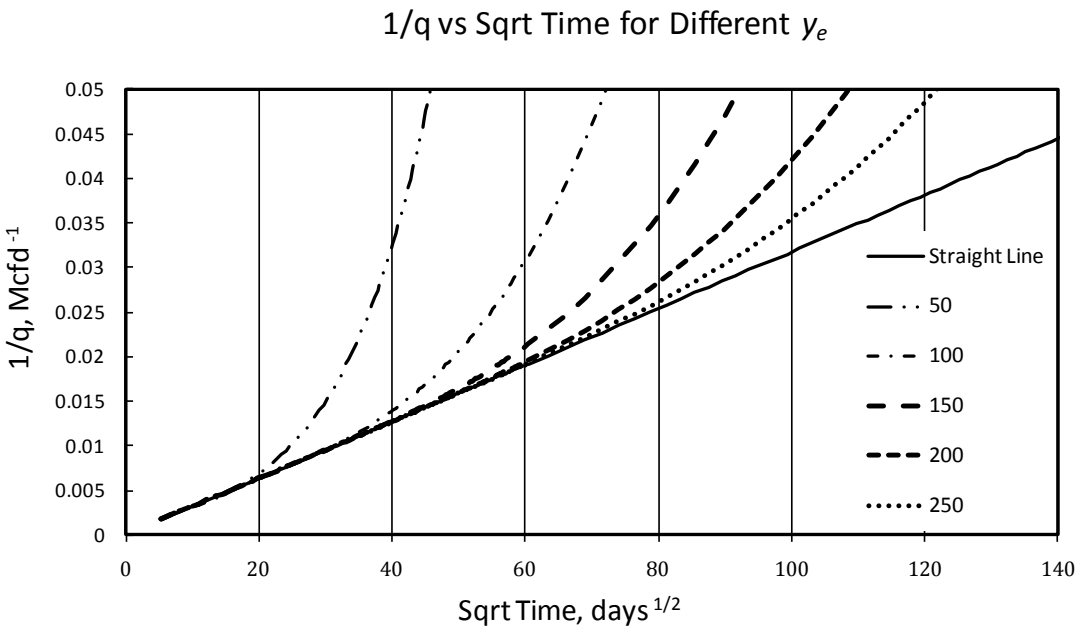

Fig. 45 - LFA plot showing the numerical model with different values of y_e.

Analytical Results			
Frac Spacing	y_e	t_{ehs}	$t_{ehs}^{1/2}$
ft	ft	days	$days^{1/2}$
50	25	52	7
100	50	207	14
150	75	466	22
200	100	828	29
250	125	1,293	36
300	150	1,862	43
350	175	2,535	50
400	200	3,311	58
450	225	4,190	65
500	250	5,173	72

Table 25 – Corresponding values for y_e and t_{ehs} for different values of fracture spacing.

A plot comparing the produced gas rates from the numerical model and the two-segment model proposed by the Nobakht *et al.* (2010) for y_e = 150 ft is shown in **Fig. 46**. The results of the numerical model are very similar to the results of the two-segment model. In the numerical model, the presence of multiphase flow explains the small difference in rates at the beginning. Although, there is a good match between the rates obtained from numerical simulation and those calculated from Nobakht *et al.* (2010) method, this two segment model (Nobakht *et al.*, 2010) can be used to describe a homogeneous completion. This will be explained in further details in the following sections.

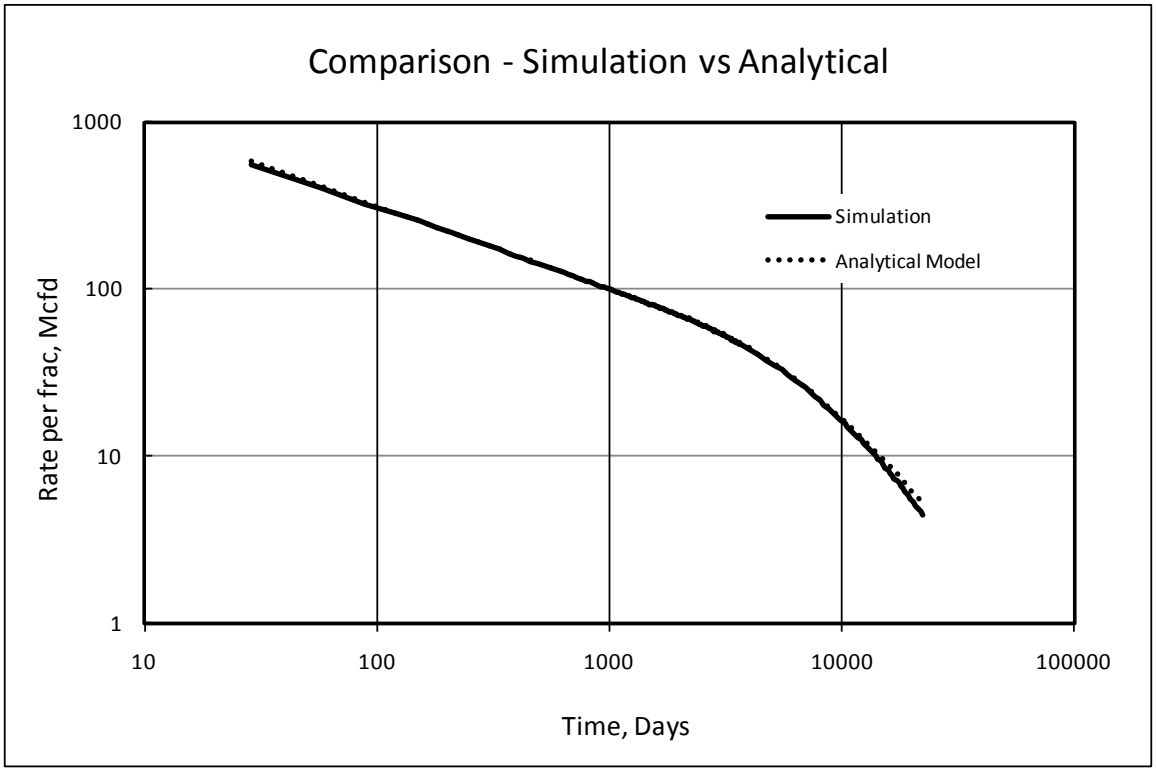

Fig. 46 – Log-log rate time plot showing comparison of numerical model and the two-segment model proposed by Nobakht *et al.* (2010) for y_e=150 ft.

6.2 Bi-Wing Fracture Evidence in Shales

Many authors (Warpinski, 1991; Warpinski *et al.*, 2008; Warpinski *et al.*, 2009; Cipolla *et al.*, 2008a and 2008b; Cramer, 2008; Fisher *et al.*, 2002; King *et al.*, 2008; Olsen *et al.*, (2009); and King, 2010) have tried to describe conceptually the "complexity" that is created during the fracturing process of a shale gas well. The "complexity" concept is the result of trying to interpret the differing microseismic pattern response in wells. In this section, a new conceptual model is discussed in regards to how a hydraulic fracture is created in a shale gas reservoir.

In nearly every shale there exists a fabric of natural fractures that is the result of burial environment and historic tectonic activity on the formation. This tectonic activity

creates natural fractures; for example, in the Barnett Shale these natural fractures form en echelon arrays and these natural fractures are typically mineral filled (Gale *et al.*, 2007; and Selleck, 2011). Natural fractures in these systems provide planes of weakness (Jacobi *et al.*, 2008; and Gale and Holder, 2008). Gale and Holder (2008) measured that the breakdown pressure of these closed and mineralized fractures to be 50% of that of non-fractured rock. Overbey *et al.* (1988a and 1988b), Nearing and Startzman (1988) and Gale *et al.*, (2007), Gale and Holder (2008) and Gale and Laubach (2009) described the preferential opening of natural fractures in these systems and lab work places the width of these fractures in the range of less than 0.002" (King, 2010). These fractures typically form primary, secondary or tertiary fracture sets when present (King, 2010) and have been photographed in outcrops (Engelder and Lash, 2008; Lash 2008). The main belief throughout the industry is that these fractures provide additional surface area when propped or opened and this additional surface area provides the incremental production performance needed for economic development (King, 2010). This hypothesis is primarily a result of microseismic event interpretation (Maxwell *et al.*, 2002). King (2010) also states that the natural fracture systems provide leak-off and the fractures are very small. Therefore it is the author's hypothesis that the water from the stimulation remains in the "opened" natural fracture system and is held there by capillary forces. Further, the water in the natural fracture system does not greatly increase the productivity of the well. Therefore, a simple bi-wing model can be utilized to explain the production behavior of a shale gas system. The evidence for the bi-wing model was obtained using a "mine-back" experiment.

A "mine-back" experiment is one where a well is drilled through the completion interval of a previously producing offset well. Cipolla *et al.* (2008b) discussed an actual "mine-back" experiment to investigate fracture complexity. In the 22 mine-back experiments conducted on CBM reservoirs new hydraulic fractures were seldom created. The "mine-back" discussed here is slightly different, since these wells are deeper and cannot be accessed via shaft. In another work by Moschovidis *et al.*, (2000), actual core was taken. In the core that was taken, a series of fractures was found, however, the intervals were much shallower, and this width of the created fracture system was less than 50 ft. In addition the goal of Moschovidis *et al.* was to dispose drilling cuttings. In the example shown here, when the new well (or wells) is drilled, an image log is run (either via wireline or logging while drilling) in order to create a micro-resistive "image" of the borehole. The image of the borehole can then be interpreted to yield information about the well and reservoir. Information typically obtained from a borehole image log includes location of faults, fractures (both natural and artificial), bedding and borehole breakout. **Fig. 47** shows a map-view schematic of a "mine-back" experiment.

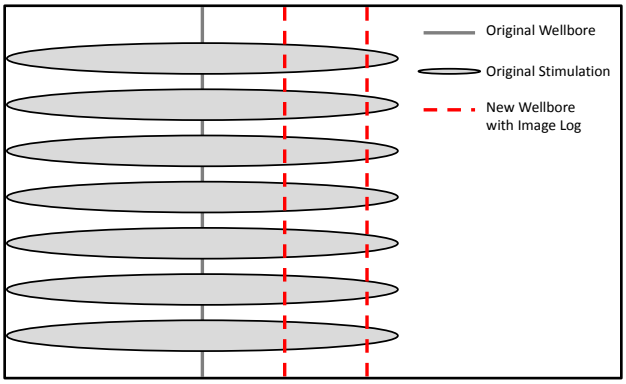

Fig. 47 – Diagram of a "mine-back" experiment. The gray well on the left would be drilled and completed prior to drilling the red wells. The red wells would be image logged and are approximately spaced at 250 ft and 500ft away from the original wellbore.

The example shown below, in **Fig. 48,** is a map-view of a mine-back experiment. The original well, shown in green, was drilled and completed approximately one year prior to the drilling and image logging of the red and yellow wells. The green well was stimulated at each light-blue bar (approximately 300' intervals) with one perforation cluster. The red and yellow wells were drilled approximately 300 ft and 600 ft away from the original green well. The yellow and green wells are on the same approximate horizon, while the green well is drilled at a horizon approximately 60-90 ft deeper. The image log interpretation of the red and yellow wells (shown with black arrows) showed interpreted open fractures at the green and yellow bars respectively (shown with white arrows). The image log of the red well is shown in **Fig. 49**.

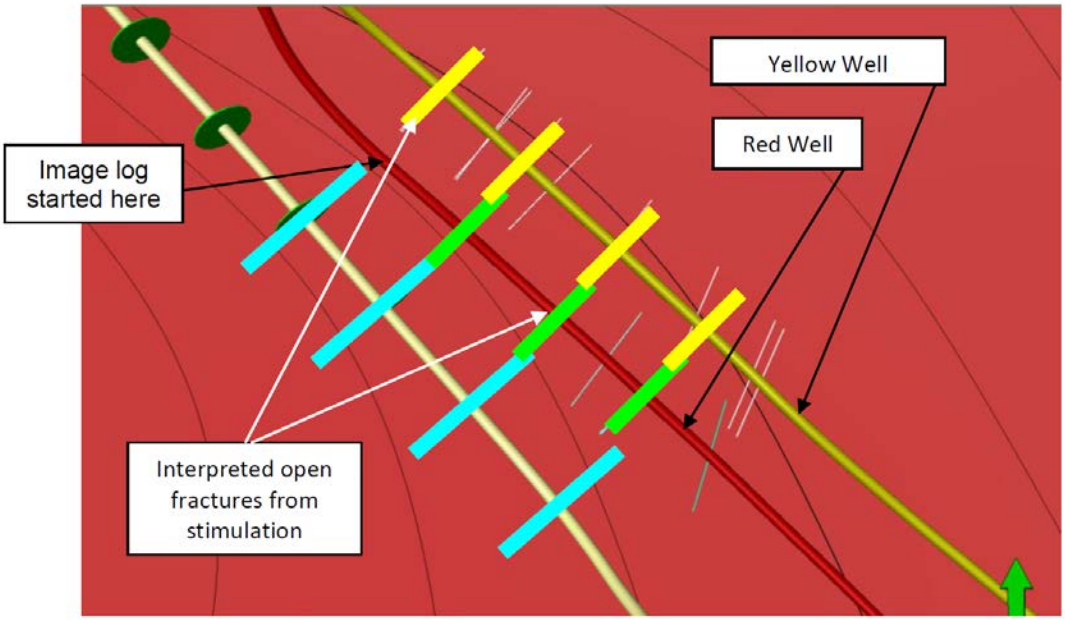

Fig. 48 – Map-view of a "mine-back" experiment. The green wellbore was drilled and hydraulically fractured approximately one year before the red and yellow wellbores (noted in picture by black arrows) were drilled and logged. The blue bars are the hydraulic fracture initiation points in the green well. The green bars are the interpreted hydraulic fractures in the red well and the yellow bars are the interpreted hydraulic fractures in the yellow well.

In this figure, there are multiple tracks that contain data and interpreted data. The bottom tracks contain histograms and orientation information of the fractures interpreted from the image log. The main items to focus on in the interpreted information are the conductive fractures (highlighted with arrows in the figure). Referring back to **Fig. 48**, these interpreted conductive fractures line up very well with the offset stimulation in the original well. Of additional note, is that there are many more fractures

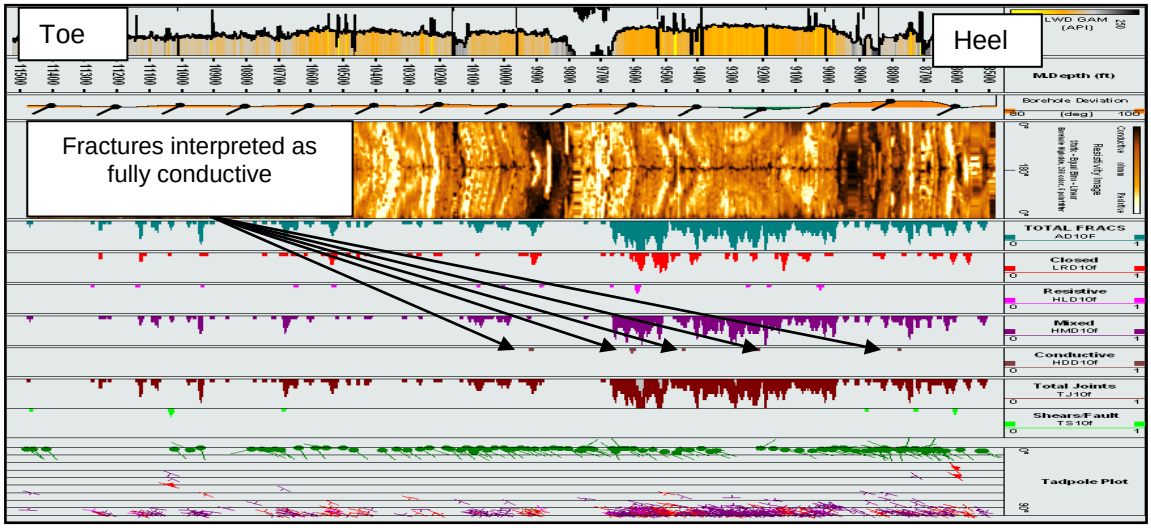

Fig. 49 – Interpretation and image log of the red well in Fig. 48. The top track is the gamma ray (GR). The image track is next. The turquoise track is a histogram of the total fracture per foot. The red histogram is that of interpreted closed fractures per foot. The pink histogram tack is fractures interpreted as resistive (or mineral filled). The purple track is fractures interpreted as partially conductive (they are interpreted to contain a conductive fluid and partial mineral fill). The brown track is that of fractures that are totally conductive (these are interpreted as fractures caused by the hydraulic fracturing process highlighted by the arrows). The total joints are the next track; followed by shear faults in green. The last track is a tadpole plot showing bedding planes and the orientation of the interpreted fractures.

near the heel of the tow, when compared to the toe. The main possibility for this observation is that the heel of the well was next to the offset stimulation from the original (green) well, whereas the toe of the well was in reservoir rock not next to offset stimulation. The hypothesis is that the water from the stimulation of the original well

provides the fluid contrast in the mineral filled natural fracture system so that the tool is able to "image" the water/mineral filled natural fractures. As stated earlier, the width of these fractures is typically less than 0.002" and would be below the resolution of the tool (Baker Hughes, 2010) unless a fluid could provide a contrast to the measurement. It is believed that the same frequency of mineral filled fractures is present in the toe section. However, the fluid to provide the contrast for the measurement tool (micro-image logging tool) has not entered into the fractures because there has not been offset hydraulic fracture stimulation.

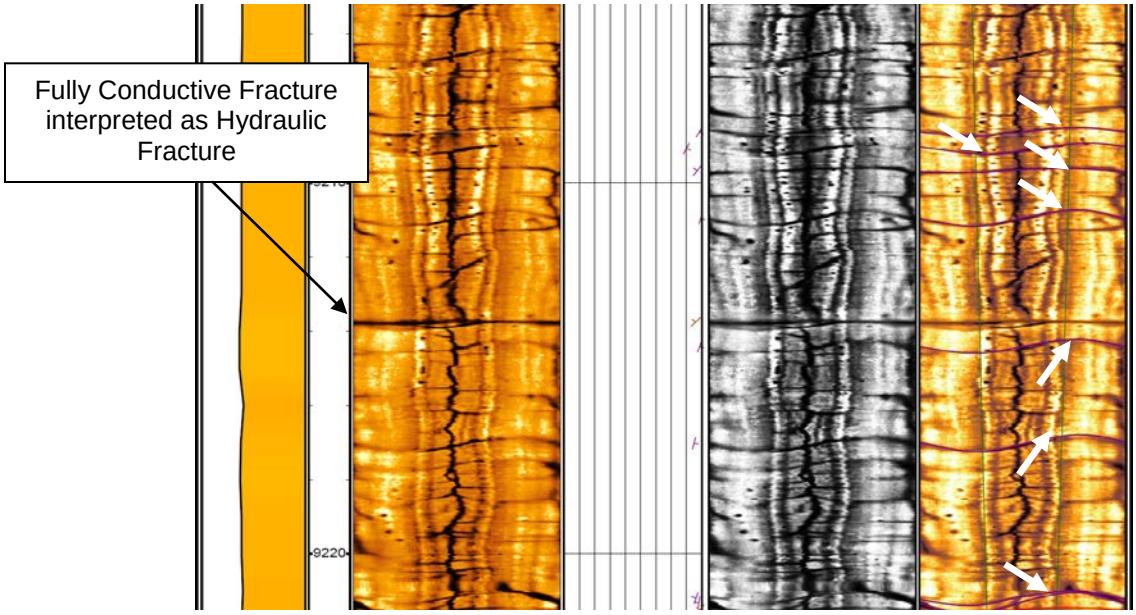

Fig. 50 – Close up of the image log of the red well in Fig. 48. The left image track is a raw or static image, where the color-scale maximum and minimum is set based upon the entire dataset. The center image is a gray-scale view of the image on the right. In these two images, dynamic scaling is used and the color-scale changes to provide greater image contrast for ease of interpretation. The large interpreted hydraulic fracture is highlighted with an arrow in this image. Also of interest is the partially conductive fractures interpreted in this image. These are highlighted with white arrows. It is believed that these fractures provide the leak-off and water trapping mechanism of much of the stimulation fluids. Additionally, the drilling induced fracture running the length of the wellbore can be clearly seen.

A close-up of an interpreted hydraulic fracture is shown in **Fig. 50**. In this figure there are many mixed conductive fractures that have been interpreted. These are interpreted as mixed conductive because the fracture does not span the entire wellbore. For orientation purposes, the center of the image track is the top of the wellbore and the edges of the image track are the bottom of the wellbore. The interpreted hydraulic fracture is clearly seen on this image as the dark fracture that spans the wellbore. The orientation of the fracture indicates its intersection angle with the wellbore. Additional information such as drilling induced fractures can also be seen as the fracture that spans the top and bottom of the wellbore. As can be seen from **Fig. 48**, the hydraulic fractures initiated at the red wellbore can be seen at 300 ft and 600 ft offsets. This is the primary indication that a simple hydraulic fracture or bi-wing type production model might be adequate to explain the production from this reservoir.

It is well known that in hydraulic fracturing stimulations performed in shale gas reservoirs that typically only a small fraction of the water that is used for stimulation is produced back to the wellbore (King, 2010). It is hypothesized here that the small openings created in the natural fracture system and the drawdown pressures in these reservoirs do not allow the stimulation water in these natural fractures to flow back. Rather, the high capillary forces hold the water in place and in effect trap it in the reservoir. As shown and discussed previously in Chapter 3, much of the system is hydrocarbon wet, due to some of the porosity being in the kerogen. Therefore, imbibition of the non-wetting phase (water in this case) cannot occur. **Fig. 51** shows the capillary threshold pressure as a function of pore radius and surface tension (from Tudor *et al*.,

2009). It is estimated that the fracture width of the re-opened natural fracture would be on the order of 0.1 to 1 micron. Therefore the capillary pressure threshold (or displacement pressure) of the water within this system would have to be in the 50-200 psi range. These kinds of pressure drops are not seen in shale gas reservoirs. It is believed that the stimulation water would be held in place by the natural fracture system and the lack of drawdown pressure on these systems. For these reasons, it is believed that a simple bi-wing model is an appropriate approach to predicting the performance of these systems. Throughout the rest of this chapter, these assumptions will be used to reveal reasonable results that are consistent with the observations and lab measurements.

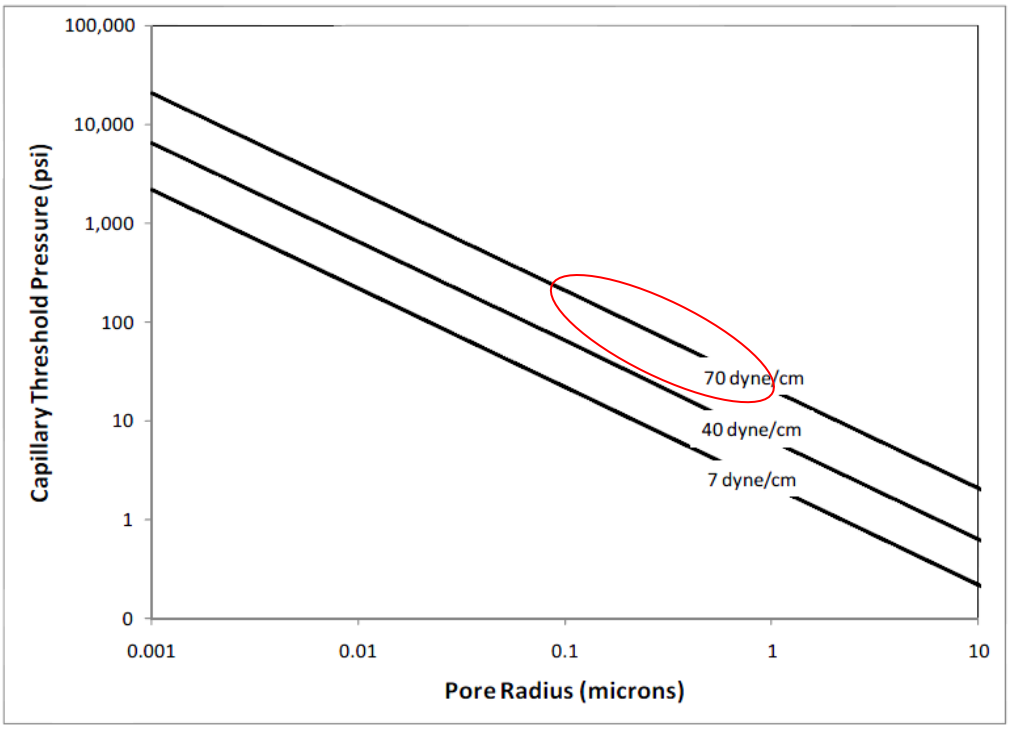

Fig. 51 – Capillary pressure threshold of rocks as a function of pore radius (distance between plates) and surface tension. The water in a opened natural fracture would have a surface tension near 70 dyne/cm. The estimated fracture width would be on the order of 0.1 to 1 micron, putting the capillary pressure or displacement pressure in the 50-200 psi range.

6.3 Homogeneous and Heterogeneous Completion Models

A homogeneous completion is defined as one where every hydraulic fracture connected to a perforation cluster is equal in length (and height). An example of a homogeneous completion is shown in **Fig. 52**. In this figure, the distance between any two adjacent fractures is $2y_e$ and the length of each fracture is $2x_f$. This system is fairly easy to analyze and forecast because of symmetry. As explained by Nobakht *et al.* (2010), the two-segment model explained in section 6.2 can be used to forecast rates for this completion. One can simply use **Eq. 38** to obtain $A_{\mathrm{cm}}\sqrt{k}$. The A_{cm} obtained is the entire fracture surface area of the system. Using the definition of A_{cm}, $A_{\mathrm{cm}} = \sum 4x_{\mathrm{f}}h$, $A_{cm}=4n_fx_fh$ for the geometry shown in **Fig. 52**, where n_f is the number of fractures. Additionally, if matrix permeability and fracture height are assumed, an estimation of x_f can be computed from **Eq. 43**.

$$x_f = \frac{A_{cm}}{4n_f h} \tag{43}$$

Fracture half length (x_f) calculated from this equation is the average fracture half length of the system. Although the homogeneous completion model is a good model to

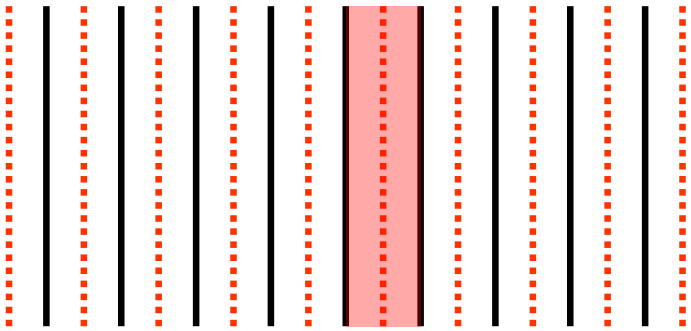

Fig. 52 - Schematic of a homogeneous completion. The fractures are represented by the black lines and the boundaries are represented by the dotted red lines. All fractures are exactly the same and are evenly spaced.

conceptualize the reservoir process, fracture lengths that are equal in length (or area) are never seen. This is due to multiple clusters in a hydraulic fracture stage, localized stress heterogeneities within the reservoir, differences in perforation effectiveness, and differences in localized leak-off (whether within the reservoir or upper or lower boundaries). Therefore, it is incorrect to believe that all fracture lengths (or areas) should be the same, which will lead to a heterogeneous completion model.

A heterogeneous completion is defined as a completion where not all the fracture lengths (or areas) are the same, hence heterogeneous. As mentioned earlier, this model is a more realistic representation of actual completions within a hydraulically fractured horizontal well. A schematic of a heterogeneous completion is shown in **Fig. 53**. In this figure, the fractures have different lengths and the dotted red lines represent the internal boundaries, which are first seen when fractures start to interfere from production analysis. Although the fractures are spaced evenly, there is not a length symmetry element for this completion as fractures have different lengths.

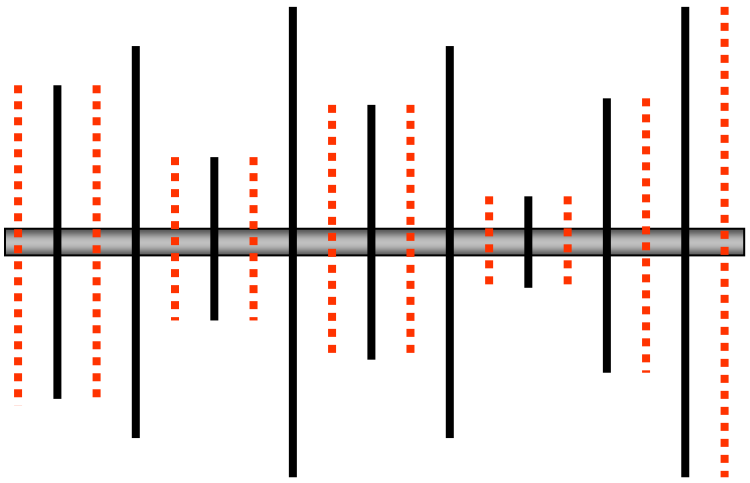

Fig. 53 - Schematic of a heterogeneous completion. The fractures are represented by the black lines and the boundaries that are first seen are represented by the dotted red lines.

Clarkson and Beierle (2011) used linear flow analysis prior to fracture interference to establish a total contributing fracture half-length, then used spinner surveys to allocate production to the individual hydraulic fracture stages, which in turn was used to infer individual hydraulic fracture half-lengths. Analytical vertical well (with hydraulic fracture) models were used to history-match production from the individual stages (if multiple spinners are available prior to fracture interference) to establish the individual hydraulic fracture lengths, with the total summed lengths equaling that obtained from linear flow analysis prior to fracture interference. They suggested the derived fracture geometries could then be input into a numerical simulator to generate a production forecast.

In this work, a simple analytical approach has been developed to model production prior to and after fracture interference for a heterogeneous completion case. In a heterogeneous completion, even though a symmetry element cannot be used, a two-segment model outlined for previously for a single fracture with the added complexity of different t_{ehs}'s can be utilized to determine when that portion of the reservoir contributing flow goes into boundary dominated flow. Rates from individual fractures are best determined from a production log. The production log data must be obtained while the entire well is still in transient flow. Additionally, the fractures should be infinite acting. It is easiest to assume that every fracture has the same height, so the flow from each fracture is just a function of its length (x_f). However, the model can be adjusted so that the fracture surface area is the variable and not the height. During infinite acting flow, **Eq. 37**

can be modified to **Eq.44**, assuming no skin and the addition of a α_{fj} term defined in **Eq. 45**.

$$\alpha_{fj}\frac{\lfloor p_{pi} - p_{pwf}) \rfloor}{q_g} = \alpha_{fj}\tilde{m}\sqrt{t} \qquad \textbf{(44)}$$

$$\sum_{j=1}^{n} \alpha_{fj} = 1$$

$$\frac{1}{q_g} = \sum_{j=1}^{n} \alpha_{fj}\frac{1}{q_g} \qquad \textbf{(45)}$$

At time t_{ehsj} the fraction of flow associated with that portion of the fracture length (or area) will transition into boundary dominated flow and a *b* factor from 2 to 0.5. Every well will have a different number (*j*) of boundary times depending upon the completion heterogeneity. **Fig. 53** shows different boundaries and **Fig. 54a** shows the associated drainage areas. Additionally, **Fig. 54b** shows the hydraulic well as a simpler vertical well with different boundary times. It is presented in two ways to help illustrate this concept. In this diagram there are six different boundary times (*j's*) seen. However, most of the fracture area is associated with boundary times one and three (i.e. red and green drainage areas). It can also be seen from **Eq. 40** and **Table 27** that the boundary times will quadruple when the distance between the boundaries doubles (i.e. fracture areas associated with the red and green boundaries).

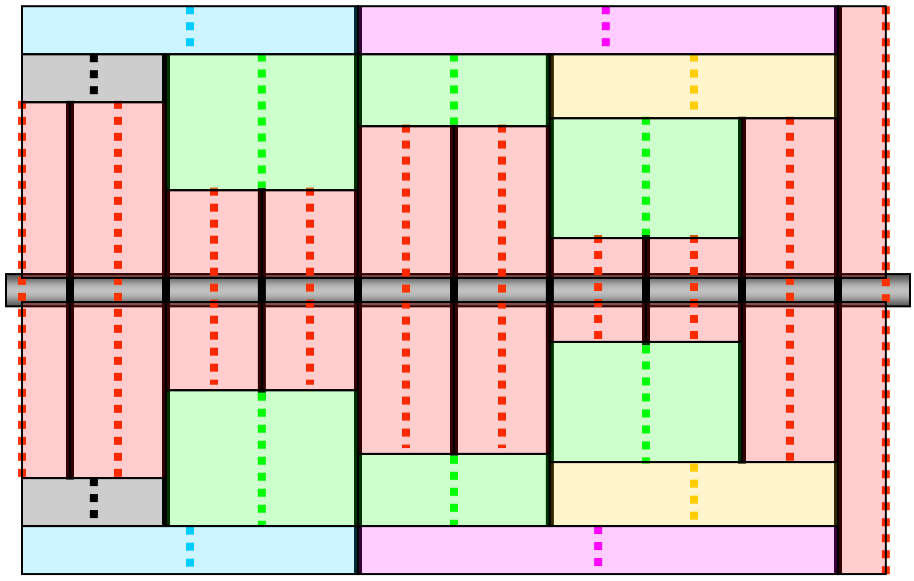

(a)

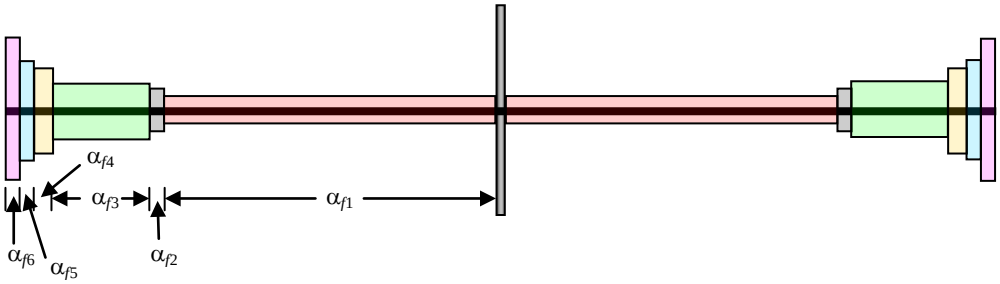

(b)

Fig. 54 – In these figures of a heterogeneous completion, each color represents a different fracture length (drainage area) associated with a different boundary time. In (a) the red dotted lines indicate the fracture length associated with the first boundary time (for example, t_{ehs} is seen in one year). The gray dotted lines, indicates the fracture length associated with the second boundary time and the green denotes the third and so on. Since the distance of the green boundary is double that of the red, the time to see the boundary for the red fracture surface area will be four times longer, or 4 years for this example. The yellow dotted line represents the fourth boundary, which is three times the distance (9 years), the blue represents the fifth boundary (3.5 times the distance or ~12.25 years) and finally the magenta represents the last boundary (5 times the distance or 25 years). In this example 62% of the flow is associated with boundary time 1, 3% with time 2, 25% with time 3, 4% with time 4, and 3% for times 5 and 6. In (b) the well is represented as a vertical well with a single fracture, with α, representing the fraction of fracture area (or half length) associated with the corresponding boundary time. In this example, the maximum area available for drainage is represented by the colored rectangles.

6.4 Analysis using the Heterogeneous Completion Model

A production log of a multi-fractured horizontal well with 14 completions is shown **Fig. 55**. An analytical model was made and log-log plot of production is shown in **Fig. 56**. The analytical model is the "hybrid" linear-flow model with the appropriate α_{fj} terms and corresponding boundary times. The LFA plot for this well is shown in **Fig. 57**. In this plot you can see the t_{ehs} estimated at $\sqrt{t}$ =19, or nearly one year. The perforations clusters in this well are spaced 100 feet apart ($2y_e$ = 100 ft) we can rearrange **Eq. 38** in the form of **Eq. 46** to determine the reservoir permeability (or diffusivity). For this example the

$$k = \left(\frac{y_e}{0.159}\right)^2 \mu c_t \left(\frac{\phi}{t_{ehs}}\right) \qquad \textbf{(46)}$$

permeability was calculated to be 57 nd (nanodarcies). It has been stated by several authors (King, 2010) that the contact area determined from microseismic interpretation is on the order of 100's of millions of ft^2, while the permeability is on the order of 100's of nd (King, 2010) . The area calculated contributing to flow for this example was 2 million square feet. It can be seen from this analysis for a well that had initial production around 2 MMscf/day (2 million standard cubic feet) that the area is nearly 100x's less than what is typically estimated from microseismic. Therefore, there is disagreement between the permeability reported by labs (on the order of 100's of nd rather than 10's of nd), the area determined stimulated from microseismic and well performance. This is another piece of evidence supporting a simpler bi-wing fracture rather than a fracture network model might be applicable in some shale gas systems.

In this example, seven different boundaries can be seen on this log and are differentiated with the colored regions in **Fig. 55**. In this figure, the top track with the colored regions is the fraction of flow interpreted from the production log associated with each perforation cluster. In the middle track a cumulative flow log for the entire well is shown. In the bottom track, a deviation survey with a superimposed hold-up log is shown. Hold-up is defined as the fraction of the cross-sectional area of pipe that contains a particular phase. From the interpreted production log data, 74.4% of the production is associated with the first boundary time, 12.5% is associated with the second boundary time, 6.1% is associated with the third boundary time and boundary times four through seven contribute 1%, 2%, 3% and 1%, respectively. Additionally, the modified simpler two segment analytical model, where the constant *b* factor of 0.8 rather than 0.5 is utilized after the first boundary is seen, is shown in **Fig. 56**. Excellent agreement between either the heterogeneous or the simpler two segment methods is seen, since the curves perfectly overlay each other.

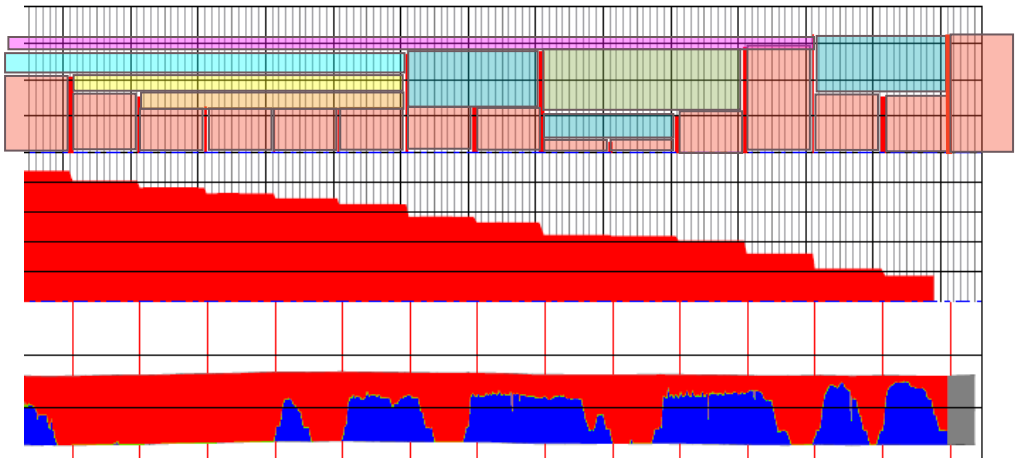

Fig. 55 - Production log of a multi-fractured (14 completions) horizontal well with seven different boundary times (α_{fj}'s) is shown. The flow area associated with the seven different boundary times is differentiated by the different colors in the top track.

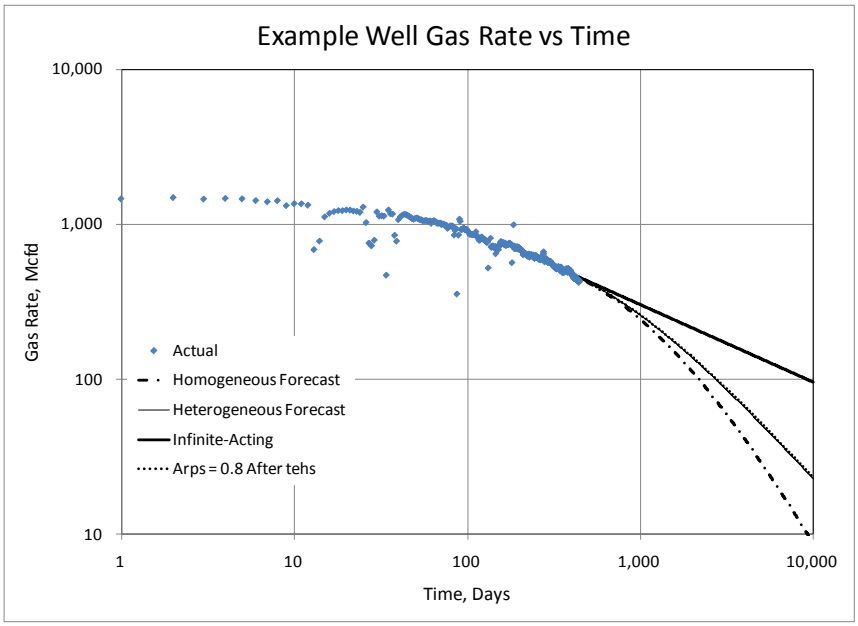

Fig. 56. Log-log production plot of a multi-fractured (14 completions) horizontal well with seven different boundary times (α_{fj}'s) is shown. There are 4 different forecasts shown. The Heterogeneous model and Arps *b* factor of 0.8 applied to the modified Nobakht model perfectly overlay each other.

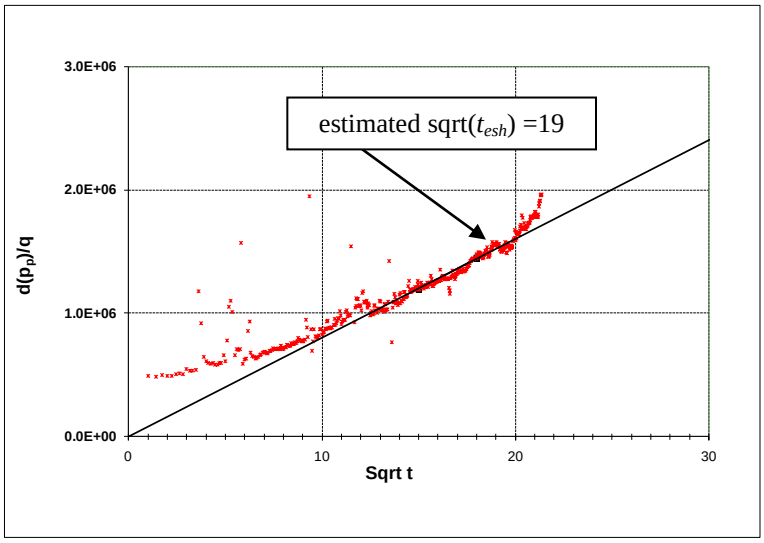

Fig. 57 - Square root time plot showing the deviation from straight line after almost one year.

The completion shown in **Fig. 55** is somewhat heterogeneous. However, wells with more heterogeneity in their completions are sometimes observed, specifically when multiple clusters per fracture stage are used (Miller *et al.*, 2011). An example of a very

heterogeneous completion is shown in **Fig. 58**. In this completion the large fracture located at x700 (and highlighted by the black arrow) accounts for nearly 40% of the production from this well. This creates a large surface area that has the potential to be under infinite acting flow for the entire production life of the well. The ten different boundary distances pictured in **Fig. 58** were modeled similarly as the example in **Fig. 55**. The resulting heterogeneous model is shown in **Fig. 59**. In the log-log production plot, four different forecasts can be seen. It is important to note that the well was interfered with around day 440 from an offset stimulation. The heterogeneous and Arps *b* factor model of 1.3 nearly overlay each other. **Fig. 60** shows the square root time plot for this well. In this plot you can see the t_{ehs} estimated at $\sqrt{t}$=15, with the perforation clusters around 85 feet apart the permeability is calculated at 70 nd.

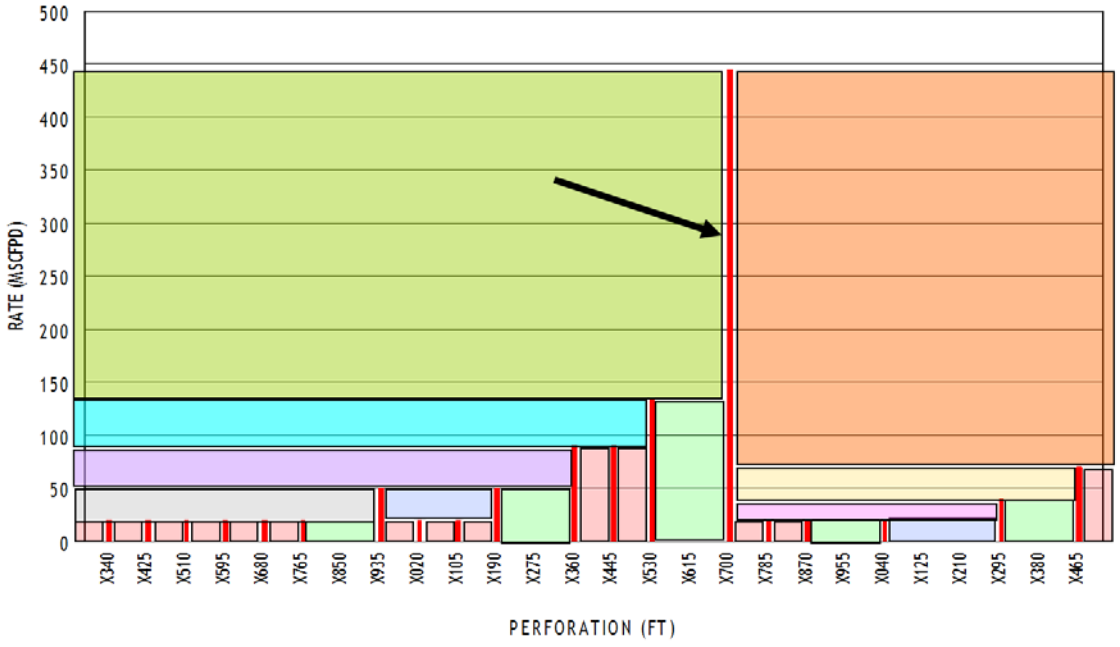

Fig. 58 – Simulated production log of a multi-fractured (26 completions) horizontal well with ten different boundary times (α_{fj}'s) is shown. The flow area associated with the ten different boundary times is differentiated by the different colors. In this completion, there is one dominant fracture that accounts for 38% of the production from this well.

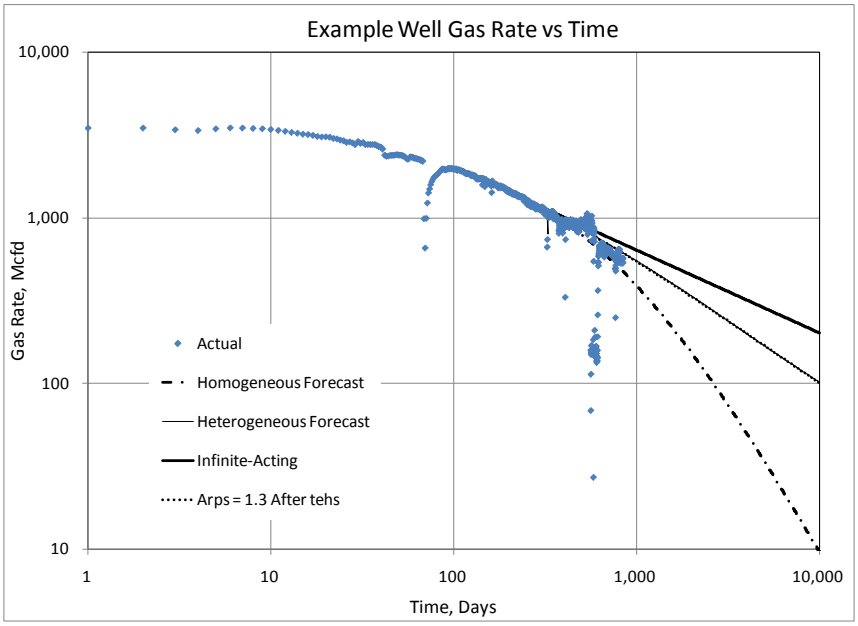

Fig. 59 - Log-log production plot of a multi-fractured (26 completions) horizontal well with ten different boundary times (α_{fj}'s) is shown. There are 4 different forecasts shown. The Heterogeneous and Arps *b* factor of 1.3 overlay each other. Of an additional note is that the well is already outperforming the Homogeneous reservoir forecast and underperforming the Infinite Acting forecast. The forecast carries forward from t_{ehs} of 225 days as seen on the plot in Fig. 60. This well was interfered with at around 440 days. The heterogeneous model and Arps model perfectly overlay each other.

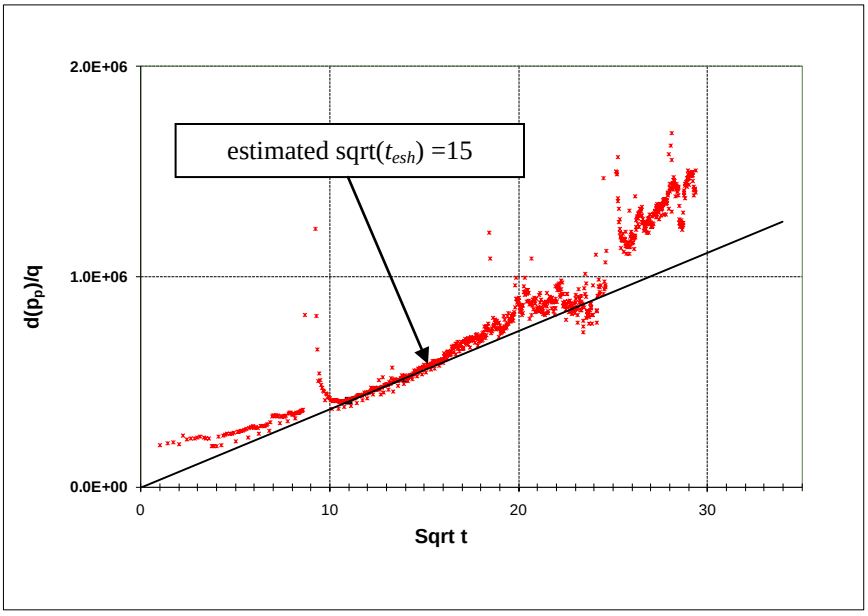

Fig. 60 - Square root time plot showing the deviation from half slope at $t^{1/2}$ of 15. An additional note is that this well was interfered with at $t^{1/2}$ of 21.

The final two examples show two wells that have been on production for 1600 days and 800 days, respectively. These wells are shown in **Fig. 61a-d**. **Fig. 61a** and **Fig. 61b** shows the well that has been producing for nearly 1600 days. This well is around 2000 ft long and has been completed with perforation clusters 500 ft apart. The well is still in infinite acting linear flow based upon it being on a negative half-slope on log-log rate-time and the LFA plot still being on a straight line going through the origin. The second well pictured in **Fig. 61c** and **Fig. 61d** is 4000 ft long, the greater length accounts for the greater initial production and has perforation clusters that are only 100 ft apart. This well reached fracture interference (or boundary dominated flow) at $t^{1/2}$ of 15 (or 225 days). The permeability calculated from **Eq. 46** is 45 nd for this example. Using 45 nd and a distance of 500 ft between clusters for the first well would put the time to boundary at nearly 15.4 years. Therefore, it is estimated to be infinite acting for the next 11 years. This example shows that the bi-wing model is consistent with well performance in these types of reservoirs.

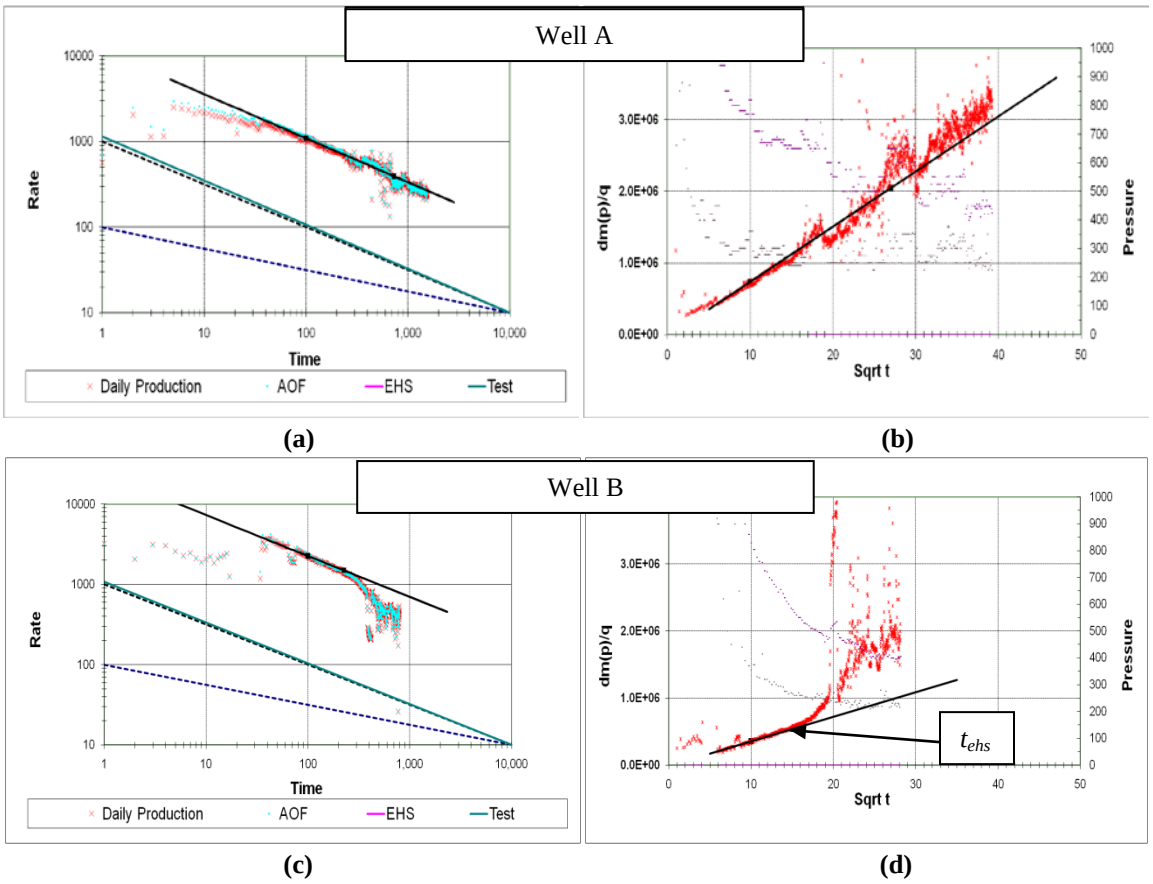

Fig. 61a-d – Decline curves for two wells are shown in this figure. Log-log rate-time plots [plots (a) and (c)] showing production rate (and pressure normalized rates depicted by AOF points), showing a clear negative half-slope. The negative half-slope is indicative of infinite acting linear flow. The well in (c) shows a deviation from this point at time near 225 days. Plots (b) and (d) show LFA plots of the data. The well in plot (b) is still in infinite acting conditions, while the well in plot (d) shows evidence of boundary dominated flow at $t^{1/2}$ of 15, or 225 days. The top well has perforation clusters 500' apart, while the bottom well has perforation clusters 100' apart. A bi-wing model is consistent with this type of well performance and helps explain the difference, i.e. it is a mainly a function of completion strategy. In the reservoir where these wells are from, this behavior is seen on over 500 wells.

With these four examples, if the reservoir parameters are consistent, it can be demonstrated that the future performance of a well is largely dependent upon the completion. The first two sets of examples show that future performance is a function of how heterogeneous the completion is. In these two examples, the modeled *b* factor varied from 0.5 (homogeneous completion) to 1.3 (very heterogeneous completion). This

change in *b* factor represents a potential large forecast difference. The change in predicted performance is shown in **Table 28**. It is also important to note that the greater the *b* factor, the less the recovery factor will be. However, the drainage area will typically be larger so ultimate recovery would be more, but efficiency would be less. The drainage area is defined by the length of the longest fracture, therefore by definition; the drainage area will be larger. Therefore, for these kinds of wells, you cannot have a high final *b* factor and a high recovery factor.

	10,000 day Cumulative MMSCF			
Forecast Method	Arps *b*	Well 1	Arps *b*	Well 2
Homogeneous Completion		910		1,552
Infinite Acting		1,824		3,873
Heterogeneous Completion		1,100		2,824
Arps forecast	0.8	1,109	1.3	2,822

Table 26 - Forecasted 10,000 day cumulative production (MMSCF), and single Arps *b* (single Arps applied after infinite acting linear flow period) for two example wells.

The second set of examples shows that the distance between the perforation clusters can greatly change the forecast and long term well performance of wells in these types of reservoirs. It can be clearly seen that although the second well had greater initial performance, that the first well is performing nearly the same at 800 days. Additionally, the first well should outperform the second well, for the remainder of the well lives.

6.5 Workflow for Determination of Optimum Fracture and Well Spacing

Determining an optimized development plan is critical in shale/tight gas plays due to their capital intensiveness and dependence upon commodity prices. Meyer *et al.* (2010) discussed how the number of fractures and the fracture spacing in a completion can affect the net present value (NPV) or discounted return on investment (DROI); optimum spacing is a function of diffusivity. Diffusivity is one of the most difficult parameters to determine in a tight/shale gas reservoir. The diffusivity, η, is defined as $k_m/(\phi\mu c_t)$. In this term the permeability and porosity, specifically for shale/tight gas reservoirs, are often the most difficult to determine, specifically in the laboratory (Sondergeld *et al.*, 2010b). In this section a new methodology needed to define the diffusivity term using linear flow and the appearance of boundary dominated flow is shown. Knowing this term will decrease the uncertainty in determining the fracture half length as well as help to optimize the spacing of hydraulic fracture clusters as previously discussed (Meyer *et al*., 2010). However, this methodology is an extension; in that Meyer only address one dimension, the distance between fractures ($2y_e$), whereas this methodology addresses the distance between fractures and the development plan of the distance between horizontal wells.

Until a reservoir has reached boundary dominated flow, the matrix diffusivity is an unknown. One can use laboratory or core data in order to estimate these values, however, due to reservoir conditions that are not able to be replicated in the laboratory the diffusivity is difficult to determine with confidence (Sondergeld *et al.*, 2010b). The

main assumption with this method is that the height of the reservoir contributing to flow is known; therefore it is not a method that can be applied without additional information. Microseismic information is sometimes a good indicator of effective fracture height (Warpinski *et al*., 2010). By having a fixed y_e (also the same as half the distance between fracture clusters), knowing that most fracture clusters are contributing and using the t_{ehs} value one can rearrange **Eq. 46** into **Eq. 47**.

$$\eta = \frac{k_m}{\phi \mu c_t}$$

$$\eta = \frac{\left(\frac{y_e}{0.159}\right)^2}{t_{ehs}} \qquad \textbf{(47)}$$

$$x_f = f_{cp} \frac{315.4T}{n_f h \sqrt{k_m (\phi \mu c_t)_m}} \frac{1}{\tilde{m}} \qquad \textbf{(48)}$$

Once the diffusivity is known the average fracture half length can be determined with more certainty. Once average fracture half length is known then stimulation parameters such as stimulation volume or rate can be adjusted in order to increase fracture length. Additionally, once fracture length is known lateral spacing can be determined. Finally, with known diffusivity value, reservoir development can be optimized. Below is the workflow that is recommended in order to optimize development.

1. Place fracture clusters/fracture spacing close together such that $2y_e$ is less than ~100' (depending upon reservoir geomechanical properties) in order to minimize stress shadowing
2. With cluster/hydraulic fractures close together, BDF should be seen early
3. Once BDF is known, use t_{ehs} and known y_e to determine reservoir η.
4. Once η is known, average x_f can be calculated using **Eq. 48** with more certainty

5. Stimulation parameters can be adjusted to optimize x_f
6. Fracture spacing ($2y_e$) can be optimized using methodology of Meyer *et al.* (2010)
7. Well spacing can be optimized due to known x_f

6.6 Conclusion

In this section, simple analytical approaches for forecasting multi-fractured horizontal wells completed in shale gas reservoirs have been provided. Evidence for the use of a bi-wing model rather than a fracture network model was given that was more consistent with image data and production performance. Additionally, approaches for forecasting homogeneous and heterogeneous completion cases were presented. The following conclusions may be drawn:

1) Bi-wing fracture systems are consistent with observations from image logs and production performance was given.
2) For homogeneous completion cases, the simple 2-segment modified model as suggested by Nobakht *et al.* (2010), combining pre-fracture interference transient linear flow with post-fracture interference decline (as described with Arps hyperbolic decline equation with $b = 0.5$) does an adequate job of modeling these scenarios.
3) For heterogeneous completions, where different segments of the hydraulic fractures interfere at varying times, a transitional period occurs where the flow cannot be modeled with an Arps hyperbolic, $b = 0.5$. The simple analytical approach does a better job of modeling this transitional flow behavior; it is shown

that a $b > 0.5$ is required to model this transitional flow period, which can last for many years.

4) A procedure for designing hydraulic fracture spacing and well spacing, which is dependent on establishing the time at which hydraulic fractures interfere and a subsequent permeability estimate, should assist operators with these critical decisions.

CHAPTER VII
CONCLUSIONS AND RECOMMENDATIONS

I have considered shale gas reservoir issues from the microscopic to the macroscopic scales through investgations of gas storage in the pore structure to gas production and decline curve analysis.

The sizes of pores and pore throats were considered with multiple methods including but not limited to adsorption, SEM, STEM, NMR and MICP. It was determined that many of the pore throats were below even the highest SEM resolution and magnification. Three methods were shown that help to "see" the throats that are the main connection within the kerogen network in these shales. The two methods, MICP, and adsorption were used to first infer the pore throat sizes. STEM resolution showed that throats could be seen that are at the size where MICP and adsorption data inferred connectivity. This is an important finding because the connectivity of the pore system provides one component of the production mechanisms of these systems. This methodology can be carried into other reservoirs to give new insights to the connectivity of these systems.

Due to the extremely small pore sizes discovered and where they were discovered within the system a new petrophysical model was proposed for shale gas reservoirs. In this petrophysical model the sorbed phase, which until this point did not take up a measureable reservoir volume, was given a reservoir volume and an equivalent saturation function dependent upon the Langmuir adsorption isotherm. This finding has far reaching implications in terms of estimates of resource in place. Additionally, new

insights and added complexities were discussed, including the complexity of a change in the values reported on isotherms and their effects.

The added complexity of multi-component models and evaluated the problem with two methodologies. First, the more widely used Extended Langmuir Isotherm was evaluated. The issue with this type of model, although simple, it is not thermodynamically consistent. Second, the thermodynamically consistent, Ideal Adsorbed Solution model was evaluated. This model brought more questions specifically when the model contains two components that are not very similar, such as C1 and C4.

A new Life-Cycle decline methodology was proposed. The assumptions behind this methodology are somewhat controversial because many people within the industry believe in a fracture network model. In this work, both direct and indirect evidence suggests the system acts more as composite bi-wing fracture system. This change in the conceptual model allows for a simpler analytical model to explain the production and forecast future production.

Recommended future research could be grouped into three areas. First, continued research at the pore-scale is recommended. It is this author's belief the understanding of these systems at the fundamental pore level is just beginning. Second, more research, specifically, experimental research should be performed on the sorption of mixed gases and their comparison to multi-component models using single component data. A potentially, large issue was discovered and brought to light in this dissertation with the IAS modeled 90:10, C1:C4 system. Finally, more field data and evaluation methodologies need to be investigated on the validity of the network model due to its

wide acceptance within the industry even though there are multiple points of contradictory evidence.

REFERENCES

[1] Al-Ahmadi, H.A., Almarzooq, A.M., and Wattenbarger, R.A. 2010. Application of Linear Flow Analysis to Shale Gas Wells-Field Cases. Paper SPE 130370 presented at the SPE Unconventional Gas Conference held in Pittsburgh, Pennsylvania, 23-25 February.

[2] Agarwal, R.G., Gardner, D.C., Kleinsteiber, S.W., and Fussell, D.D., 1999. Analyzing well production data using combined type curve and decline curve concepts. *SPE Reservoir Eval. Eng.* 2 (5), 478-486. SPE-57916-PA.

[3] Allen, M.P., and Tildesley, D.J. 2007. *Computer Simulation of Liquids*. London: Oxford University Press.

[4] Ambrose, R.J., Hartman, R.C., Diaz-Campos, M., Akkutlu, I.Y., and Sondergeld, C.H. 2010. New Pore-scale Considerations in Shale Gas in-place Calculations. SPE-131772, paper presented during the SPE Unconventional Gas Conference held in Pittsburgh, Pennsylvania, February 23-25. Paper accepted for publication in SPE Journal.

[5] Anderson, J. R. and Pratt, K.C., 1985. *Introduction to Characterization and Testing of Catalysts.* Academic Press, Sydney, Australia.

[6] Arps, J.J., 1945. Analysis of Decline Curves. *Trans.*, AIME, **160**: 228-247.

[7] Baker Hughes, 2010. StarTrak Brochure, Bakerhughes.com.

[8] Bello, R.O. and Wattenbarger, R.A. 2008. Rate Transient Analysis in Naturally Fractured Shale Gas Reservoirs. Paper SPE 114591 presented at the CIPC/SPE Gas Technology Symposium 2008 Joint Conference, Calgary, Alberta Canada, 16-19 June.

[9] Bello, R.O. and Wattenbarger, R.A., 2009. Modeling and Analysis of Shale Gas Production with Skin Effect. Paper 2009-082 presented at the 2009 Canadian International Petroleum Conference, Calgary, Alberta, Canada, 16-18 June.

[10] Bello, R.O. and Wattenbarger, R.A., 2010. Multi-stage Hydraulically Fractured Shale Gas Rate Transient Analysis. Paper SPE 126754 presented at the SPE North Africa Technical Conference and Exhibition, Cairo, Egypt, 14-17 February.

[11] Brunauer, S., Emmett, P.H., and Teller, E., 1938. Adsorption of Gases in Multimolecular Layers. *J. Am. Chem. Soc.,* **60**:309-319.

[12] Brunauer, S., Deming, L.S., and Deming, W.E., 1940. On a theory of the van der Waals adsorption of gases. *J. Am. Chem. Soc.,* **62**:1723-1732.

[13] Bustin, R.M., Bustin, A.M.M., Cui, X., Ross, D.J.K., and Murthy Pathi, V.S. 2008. Impacts of Shale Properties on Pore Structure and Storage Characteristics. Paper 119892, presented at the 2008 Shale Gas Production Conference, Fort Worth, TX, November 16-18.

[14] Bustin, R.M., Bustin, A., Ross, D., Chalmers, G., Murthy, V., Laxmi, C., and Cui, X., 2009. Shale Gas Opportunities and Challenges. *Search and Discovery Articles #40382*. 20 February.

[15] Carlson, E.S., and Mercer, J.C., 1989. Devonian Shale Gas Production: Mechanisms and Simple Models. *Journal of Petroleum Technology* **43** (4): pp 476-482.

[16] Carter, R.D., 1985. Type Curves for Finite Radial and Linear Gas-Flow Systems: Constant-Terminal-Pressure Case. *SPEJ* October 1985, pp 719-728.

[17] Chalmers, G., Bustin, R. M., and Powers, I., 2009. A Pore by Any Other Name Would Be as Small: The Importance of Meso- and Microporosity in Shale Gas Capacity. Presented at the American Association of Petroleum Geologists Annual Convention and Exhibition, Denver, CO, June 7-10.

[18] Cheng, Y., Lee, W.J., and McVay, D.A., April 2009. A new approach for reliable estimation of hydraulic fracture properties using elliptical flow data in tight gas wells. *SPE Reservoir Eval. Eng*., 254-262. SPE-105767-PA.

[19] Cipolla, C., Warpinski, N.R., Mayerhoffer, M.J., Lolon, E.P., and Vincent, M.C., 2008a. The Relationship Between Fracture Complexity, Reservoir Treatment and Fracture Treatment Design. Paper SPE 115769 presented at the SPE Annual Technical Conference and Exhibition, Denver, Colorado, 21-24 September.

[20] Cipolla, C., Warpinski, N.R., and Mayerhoffer, M.J., 2008b. Hydraulic Fracture Complexity: Diagnosis, Remediation, and Exploitation. Paper SPE 115771 presented at the SPE Asia Pacific Oil and Gas Conference and Exhibition, Perth Australia, 20-22 October.

[21] Clarkson, C.R., 2003. Application of a New Multicomponent Gas Adsorption Model to Coal Gas Adsorption Systems. *SPE Journal* 8:3, 236-251.

[22] Clarkson, C.R. and Beierle, J.J., 2011. Integration of Microseismic and other post-fracture surveillance with production analysis: A tight gas study. *Journal of Natural Gas Science and Engineering* **3**: 382-401.

[23] Clarkson, C.R. and Bustin, R.M. 2000. Binary Gas Adsorption/Desorption Isotherms: Effect of Moisture and Coal Composition upon Component Selectivity. *International Journal of Coal Geology* **42**, p. 241-272.

[24] Cramer, D.D., 2008. Stimulating Unconventional Reservoirs: Lessons Learned, Successful Practices, Areas for Improvement. Paper SPE 114172 presented at the SPE Unconventional Reservoir Conference, Keystone, Colorado, 10-12 February.

[25] Cui, X., Bustin, A.M., and Bustin, R. 2009. Measurements of Gas Permeability and Diffusivity of Tight Reservoir Rocks: Different Approaches and Their applications. *Geofluids* **9**: 208-233.

[26] Curtis, M. E., Ambrose, R. J., Sondergeld, C. H., and Rai, C. S., 2010. Structural Characterization of Gas Shales on the Micro- and Nano-scales. SPE-137693, paper presented at Canadian Unconventional Resources and International Petroleum Conference, CSUG, SPE, Calgary, Alberta, Canada, October 19-21.

[27] Curtis, M. E., Ambrose, R. J., Sondergeld, C. H., and Rai, C. S., 2011. Transmission and Scanning Electron Microscopy Investigation of Pore Connectivity of Gas Shales on the Nanoscale, paper presented at the North American Unconventional Gas Conference and Exhibition, SPE, The Woodlands, TX, June 12-16.

[28] Dastidar, R. 2007. Nuclear Magnetic Resonance (NMR) Study of Freezing and Thawing of Saturated Porous Media and Application to Shale and Pore Volume Compressibility Estimation, PhD Thesis, University of Oklahoma, Norman.

[29] Diaz-Campos, M., 2010. Uncertainties in Shale Gas-In-Place Calculations: Molecular Simulation Approach. Masters Thesis, Univeristy of Oklahoma, Norman, OK.

[30] Diaz-Campos, M., and Akkutlu, I.Y., 2011. Methane Solubility Enhancement in Water Confined to Nano-scale Pores. Microfluidics and Nanofluidics Handbook: Chemistry, Physics and Life Science Principles, Vol II, CRC Press/Taylor and Francis Group.

[31] Dollimore, D. and Heal, G.R., 1964. Improved Method For Calculation of Pore Size Distribution from Adsorption Data. *J. Appl. Chem. USSR*, **14**:109.

[32] Dubinin, MM. 1960. The Potential Theory of Adsorption of Gases and Vapors for Adsorbents with Energetically Nonuniform Surfaces. *Chemical Review*, 235-241

[33] Dubinin, M. M. and Radushkevich, L.V., 1947. *Proc. Acad. Sci. USSR*, **55**:331.

[34] Dullien, F.A.L., 1992. *Porous Media Fluid Transport and Pore Structure, Second Edition.* Academic Press, San Diego, CA.

[35] Dullien, F.A.L. and Dhawan, C.K., 1975. Bivariate pore-size distributions of some sandstones. *J. Interface Colloid Sci.* **52**: 129.

[36] Dunn, K.-J., Bergman, D. J., and Latorraca, G. A., 2002. *Nuclear Magnetic Resonance petrophysical and Logging Applications*, Pergamon, New York, 293pp.

[37] EIA, 2009. 2009 Annual Energy Outlook, DOE/EIA-0383(2009).

[38] Engelder, T., and Lash, G.G., 2008. Marcellus Shale Play's Vast Resource Potential Creating Stir in Appalachia. *The American Oil and Gas Reporter*, May.

[39] FEI, 2009. Magellan XHR SEM Product Data.

[40] Fetkovich, M.J., 1980. Decline Curve Analysis Using Type Curves. *Journal of Petroleum Technology* June 1980, pp 1065-1077. SPE Paper 4629.

[41] Fisher, M.K., Davidson, B.M., Goodwin, A.K., Fielder, E.O., Buckler, W.S., and Steinsberger, N.P., 2002. Integrating Fracture Mapping Technologies to Optimize Stimulations in the Barnett Shale. Paper SPE 77441 presented at the SPE Annual Technical Conference and Exhibition, San Antonio, Texas, September 29 - October 3.

[42] Frenkel, D. and Smit B. 2002. *Understanding Molecular Simulation – From Algorithms to Applications*. San Diego: Academic Press, Computational Science Series.

[43] Gale, J.F.W., Reed, R.M., and Holder, J., 2007. Natural Fractures in the Barnett Shale and their importance for hydraulic fracture treatments. *AAPG Bulletin*, **91**:603-622.

[44] Gale, J. and Holder, J., 2008. Natural Fractures in Shales and Their Importance for Gas Production. Techtonics Studies Groups Annual Meeting, La Roche-en-Ardenne, Belgium, 8-10 January.

[45] Gale, J.F.W., and Laubach, S.E., 2009. Natural Fracture in the New Albany Shale and Their Importance for Shale-Gas Production. Fracture Research and Application Consortium, Funded by RPSEA.

[46] Goldstein, J., Newbury, D., Joy, D., Lyman, C., Echlin, P., Lifshin, E., Sawyer, L., and Michael, J., 2007. *Scanning Electron Microscopy and X-Ray Microanalysis*, Springer, New York, NY.

[47] Gregg., S.J. and Sing, K.S.W. , 1982. *Adsorption, Surface Area and Porosity*. Academic Press, Inc., Orlando, FL.

[48] GRI (Gas Research Institute) 1997. *Coalbed Reservoir Gas in-place Analysis*, Chicago: Gas Research Institute.

[49] Hall, F.E., Zhou, C., Gasem, K.A.M., Robinson, R.L. Jr., and Yee, D. 1994. Adsorption of Pure Methane, Nitrogen, and Carbon Dioxide and Their Binary Mixtures on Wet Fruitland Coal. Paper SPE 29194 presented at the 1994 SPE Eastern Regional Conference and Exhibition, Charleston, West Virginia, 8–10 November.

[50] Hartman, R.C., Lasswell, P., and Bhatta, N., 2008. Recent Advances in the Analytical Methods Used for Shale Gas Reservoir Gas-in-Place Assessment. *Search and Discovery Article #40317*. 30 October.

[51] Haydel, J., and Kobayashi, R. 1967. Adsorption Equilibria in the Methane-Propane-Silica Gel System at High Pressures. *Industrial and Engineering Chemistry Fundamentals*, **6**: 564-554.

[52] Howard, J.J. 1991. Porosimetry Measurement of Shale Fabric and its Relationship to Illite/Smectite Diagenesis.*Clays and Clay Minerals* **39** (4): 355-361.

[53] Ibrahim, M. and Wattenbarger, R.A., 2006. Analysis of Rate Dependence in Transient Linear Flow in Tight Gas Wells. Paper SPE 100836 presented at the Abu Dhabi International Petroleum Exhibition and Conference, Abu Dhabi, U.A.E., 5-8 November.

[54] Ilk, D., Rushing, J.A., Perego, A.D., and Blasingame, T.A., 2008. Paper SPE 116731 presented at the SPE Annual Technical Conference and Exhibition, Denver, CO, 21-24 September.

[55] Jacobi, D., Gladkikh, M., LeCompte, B., Hursan, G., Mendez, F., Longo, S., Ong, S., Bratovich, M., Patton, G., and Shoemaker, P., 2008. Integrated Petrophysical Evaluation of Shale Gas Reservoirs. Paper SPE 114925 presented at the CIPC/SPE Gas Technology Symposium Joint Conference, Calgary, Canada, 16-19 June.

[56] Kale, S. V., Rai, C. S., and Sondergeld, C. H. 2010. Petrophysical Characterization of Barnett Shale. paper SPE 131770-PP, Presented at the SPE Unconventional Gas Conference, Pittsburgh, Pennsylvania, 23-25 February.

[57] Kang, S.M., Fathi, E., Ambrose, R. J., Akkutlu, I.Y., and Sigal, R.F., 2010. CO_2 Storage Capacity of Organic-Rich Shales. Paper SPE 134583 presented at the SPE Annual Technical Conference, Florence, Italy, 19-22 September.

[58] King, G.E., Hailer, L., Shuss, J., and Dobkins, T.A., 2008. Increasing Fracture Path Complexity and Controlling Downward Fracture Growth in the Barnett Shale. Paper SPE 119896 presented at the 2008 SPE Shale Gas Production Conference, Fort Worth, Texas, 16-18 November.

[59] King, G. E., 2010. Thirty Years of Gas Shale Fracturing: What Have We Learned? Paper SPE 133456 presented at the SPE Annual Technical Conference, Florence, Italy, 19-22 September.

[60] Langmuir, I., 1916. The evaporation, condensation and reflection of molecules and the mechanism of adsorption. *Phys. Rev.* **8**(2):149-176.

[61] Larsen, L., and Hegre, T.M. 1991. Pressure-Transient Behavior of Horizontal Wells With Finite-Conductivity Vertical Fractures. Paper SPE 22076 presented at the International Arctic Technology Conference, Anchorage, Alaska, 29–31 May.

[62] Lash, G.G., 2008. The Upper Devonian Rhinestreet Shale: An Unconventional Reservoir in Western New York State. SUNY, Fredonia, NY.

[63] Loucks, R.G., Reed, R.M., Ruppel, S.C., and Jarvie, D.M. 2009. Morphology, Genesis, and Distribution of Nanometer-Scale Pores in Siliceous Mudstones of the Mississippian Barnett Shale. *Journal of Sedimentary Research* **79**: 848-861.

[64] Luffel, D.L. and Guidry, F.K. 1992 New Core Analysis Methods for Measuring Rock Properties of Devonian Shale. *J. Petroleum Tech.* 1184-1190.

[65] Luffel, D.L., Hopkins, C.W., and Schettler, P.D. 1993. Matrix Permeability Measurement of Gas Productive Shales. Paper SPE-26633 presented at the SPE 68th Annual Tech. Conference & Exhibition, Houston, Texas, October 3-6.

[66] Martinez, G.A. and Davis, L. A., 2000. Petrophysical Measurements on Shales Using NMR , paper 62851-MS DOI:10.2118/62851-MS , SPE/AAPG Western Regional Meeting, 19-22 June, Long Beach, California.

[67] Mattar, L., and Anderson, D.M., 2005. Dynamic material balance (oil or gas-in-place without shut-ins). In: Paper Presented at the Petroleum Society's 6th Canadian International Petroleum Conference held in Calgary, Alberta, Canada, 7-9 June.

[68] Mattar, L. and McNeil, R., June 1997. The 'flowing' material balance. J. Can. Pet. Technol., 52-55.

[69] Mavor, M.J., Hartman, R. C., and Pratt, T.J. 2004. Uncertainty in Sorption Isotherm Measurements. Paper No. 411 presented at the International Coalbed Methane Symposium, University of Alabama, Tuscaloosa, May.

[70] Mavor, M.J., Pratt, T.J., Nelson, C.R., and Casey, T.A., 1996. Improved Gas-In-Place Determination for Coal Gas Reservoirs. Paper SPE 35623 presented at the SPE Gas Technology Symposium, Calgary, Alberta, Canada, April 28- May 1.

[71] Maxwell, S.C., Urbancic, T.J., Steinsberger, N., and Zinno, R., 2002. Microseismic Imaging of Hydraulic Fracture Complexity in the Barnett Shale. Paper SPE 77440 presented at the 2002 Annual Technical Conference and Exhibition, San Antonia, Texas, 29 September - 3 October.

[72] Mayerhoffer, M.J., Lolon, E.P., Youngblood, J.E., and Heinze, J.R., 2006. Integration of Microseismic Fracture Mapping Results with Numerical Fracutre Network Production Modeling in the Barnett Shale. Paper SPE 102103 presented at the Annual Technical Conference and Exhibition, San Antonio, Texas, 24-27 September.

[73] McCain W.D. 1990. The properties of Petroeleum Fluids. 2nd Edition PennWell Publishing Company, Tulsa Oklahoma.

[74] Medeiros, F., Ozkan, E., and Kazemi, H., 2008. Productivity and Drainage Area of Fractured Horizontal Wells in Tight Gas Reservoirs. *SPE Reservoir Evaluation & Engineering*, October: 902-911. Paper SPE 108110-PA.

[75] Menon, P. G. 1968. Adsorption at High Pressures. *Chemical Reviews* **68**: 277-294.

[76] Meyer, B.R., Bazan, L.W., Jacot, R. H., and Lattibeaudiere, M.G., 2010. Optimization of Multiple Transverse Fractures in Horizontal Wellbores. Paper SPE 131732 presented at the SPE Unconventional Gas Conference, Pittsburgh, PA, 23-25 February.

[77] Miller, C., Water, G., and Rylander, E., 2011. Evaluation of Production Log Data from Horizontal Wells Drilled in Organic Shales. Paper SPE 144326 presented the North American Unconventional Gas Conference and Exhibition, The Woodland, TX, 14-16 June.

[78] Ming, L., Anzhong, G., Xuesheng, L., and Rongshun, W. 2003. Determination of the Adsorbate

Density from Supercritical Gas Adsorption Equilibria Data. *Carbon* **41**: 585-588.

[79] Moncrieff, J. 2009. Microstructure of Shale. Poster presentation at SPWLA Annual Meeting, Houston, Texas.

[80] Moschovidis, Z., Steiger, R., Peterson, R., Warpinski, N., Wright, C., Chesney, E., Hagan, J., Abou-Sayed, A., Keck, R., Fleming, C., Wolhart, S., McDaniel, B., Sinor, Al., Ottesen, S., Miller, L., Beecher, R., Dudley, J., Zinno, D., and Akhmedov, O., 2000. The Mounds Drill-Cuttings Injection Field Experiment: Final Results and Conclusions. Paper IADC/SPE 59115 presented at the IADC/SPE Drilling Conference, New Orleans, Louisiana, 23-25 February.

[81] Myers, A.L., 1968. Adsorption of Gas Mixtures. *Ind. Eng. Chem.* **60**, p. 45-49.

[82] Myers, A.L., and Prausnitz, J.M. 1965. Thermodynamics of Mixed-Gas Adsorption. *AIChEJ* **11** (1), 121.

[83] Nearing, T.R. and Startzman, R.A., 1988. Shale Well Productivity. Paper SPE 18553 presented at the 1988 SPE Eastern Regional Meeting, Charleston, West Virgina, 1-4 November.

[84] Nobakht, M., Mattar, L., Moghadam, S., and Anderson, D.M., 2010. Simplified Yet Rigorous Forecasting of Tight/Shale Gas Production in Linear Flow. Paper SPE 133615 presented at the SPE Western Regional Meeting, Anaheim, California 27-29 May.

[85] Nobakht, M., and Mattar, L. 2010. Analyzing Production Data from Unconventional Gas Reservoirs with Linear Flow and Apparent Skin. Paper SPE 137454 presented at the Canadian Unconventional Resources and International Petroleum Conference held in Calgary, Alberta, 19-21 October.

[86] Olsen, T.N., Bratton, T.R., and Thiercelin, M.J., 2009. Quantifying Proppant Transport for Complex Fractures in Unconventional Formations. Paper SPE 119300 presented at the 2009 SPE Hydraulic Fracturing Technology Conference, The Woodlands, TX, 19-21 January.

[87] Overbey, W.K., Yost II, A.B., and Wilkins, D.A., 1988a. Inducing Multiple Hydraulic Fractures From a Horizontal Wellbore. Paper SPE 18249 presented at the SPE Annual Technical Conference and Exhibition, Houston, Texas, 2-5 October.

[88] Overbey, W.K., Yost, L.E., and Yost II, A.B., 1988b. Analysis of Fractures Observed by Borehole Video Camera in a Horizontal Well. Paper SPE 17760 presented at the SPE Gas Technology Symposium, Dallas, Texas, 13-15 June.

[89] Ozawa, S., Kusumi, S., and Ogino, Y. 1976. Physical Adsorption of Gases at High Pressure. *J. Colloid Interface Science* 83-91.

[90] Ozkan, E., Brown, M., Raghavan, R., and Kazemi, H. 2009. Comparison of Fractured Horizontal-Well Performance in Conventional and Unconventional Reservoirs. Paper SPE 121290 presented at the SPE Western Regional Meeting, San Jose California, 24–26 March.

[91] Passey, Q. R., Bohacs, K. M., Esch, W. L., Klimentidis, R., and Sinha, S., 2010. From Oil-Prone Source Rock to Gas-Producing Shale Reservoir – Geologic and Petrophysical Characterization of Unconventional Shale-Gas Reservoirs, SPE-131350, paper presented at the CPS/SPE International Oil & Gas Conference and Exhibition in China, SPE, Beijing, China, June 8-10.

[92] Poe, B.D., Conger, J.G., Farkas, R., Jones, B., Lee, K.K., and Boney, C.L. 1999. Advanced fractured well diagnostics for production data analysis. Paper SPE 56750 presented at the SPE Annual Technical Conference and Exhibition, Houston, TX, 3-6 October.

[93] Raghavan, R.S., Chen, C. C., and Agarwal, B. 1997. An Analysis of Horizontal Wells Intercepted by Multiple Fractures. *SPEJ* **2** (September 1997): 235-245. SPE-27652-PA.

[94] Ritter, H.L. and Drake, L.C., 1945. *Ind. Eng. Chem.* **17**: 782.

[95] Ritter, J.A and Yang, R.T. 1987 Equilibrium Adsorption of Multicomponent Gas-Mixtures at Elevated Pressures. *Industrial & Engineering Chemistry Research*, 26:8, 1679-1686

[96] Ross, D.J.K. and Bustin, R.M. 2007. Impact of mass balance calculations on adsorption capacities in microporous shale gas reservoirs, *Fuel*. **86**:2696-2706.

[97] Ruthven, D.M., 1984. Principles of Adsorption and Adsorption Processes. John Wiley and Sons, Inc., New York.

[98] Schettler, P.D. and Parmely, C.R, 1991. Contributions to Total Storage Capacity in Devonian Shales. SPE Paper 23422 presented at the SPE Eastern Regional Meeting, Lexington, KY, 22-25 October.

[99] Schettler, P.D., Parmely, C.R., and Lee, W. J., 1989. Gas Storage and Transport in Devonian Shales. SPE Paper 17070, *SPE Formation and Evaluation.* September, 1989: 371-376.

[100] Schieber, J., 2010. Common Themes in the Formation and Preservation of Intrinsic Porosity in Shales and Mudstones – Illustrated with Examples across the Phanerozoic. SPE-132370, paper presented at the Unconventional Gas Conference, SPE, Pittsburgh, PA, February 23-25.

[101] Selleck, B., 2011. 987565 Deformation in the Appalachian Foreland: Detachment Structures in the Basal Marcellus Shale, Central New York, *AAPG 2011*.

[102] Slatt, R.M., Singh, P., Philp, R.P., Marfurt, K.J., Abousleiman, Y., and O'Brien, N.R., 2008. Workflow for Stratigraphic Characterization of Unconventional Gas Shales. Paper SPE 119891 presented at the SPE Shale Gas Production Conference, Fort Worth, 16-18 November.

[103] Smith, J.R., Chen, A., Gostovic, D., Hickley, D., Kundinger, D., Duncan, K.L., DeHoff, R.T., Jones, K.S., and Wachsman, E.D., 2009. Evaluation of the relationship between cathode microstrucutre and electrochemical behavior of SOFCs. *Solid State Ionics* **180**: 90-98.

[104] Sondergeld, C.H., Ambrose, R.J., Rai, C.S. and Moncrieff, J. 2010a. Micro-Structural Studies of Gas Shales, Paper SPE 131771 presented at the SPE Unconventional Gas Conference, Pittsburg, PA, 23-25 February.

[105] Sondergeld, C.H., Newsham, K.E., Comisky, J.T., Rice, M.C., and Rai, C.S. 2010b. Petrophysical Considerations in Evaluating Producing Shale Gas Resources. Paper 131768 presented at the SPE Unconventional Gas Conference, Pittsburgh, PA, 23-25 February.

[106] Tan, Z. and Gubbins, K.E., 1990. Adsorption In Carbon Micropores at Supercritical Temperatures. *J. Phys. Chem.*, **94**:6061-6069.

[107] Tsai, M.C., Chen, W.N., Cen, P.L., Yang, R.T., and Kornosky, R.M. 1985. Adsorption of Gas Mixture on Activated Carbon. *Carbon* **23**: 167-73.

[108] Tudor, E.H., Nevison, G.W., Allen, S., and Pike, B., 2009. Case Study of Novel Fracturing Fluid that Maximizes Effective Fracture Length. Paper SPE 124480 presented at the SPE Annual Technical Conference and Exhibition, New Orleans, LA, 4-7 October.

[109] Valkó, P.P., 2009. Assigning Value to Stimulation in the Barnett Shale: A Simultaneous Analysis of 7000 Plus Production Histories and Well Completion Records. Paper SPE 119369 presented at the SPE Hydraulic Fracturing Technology Conference, The Woodlands, TX 19-21 January.

[110] Valkó, P.P. and Lee, J., 2010. A Better Way TO Forecast Production From Unconventional Gas Wells. Paper SPE 134231 presented at the SPE Annual Technical Conference and Exhibition, Florence, Italy, 19-22 September.

[111] van Kruysdijk, C.P.J.W., and Dullaert, G.M. 1989. A Boundary Element Solution of the Transient Pressure Response of Multiple Fractured Horizontal Wells. Paper presented at the 2nd European Conference on the Mathematics of Oil Recovery, Cambridge, England.

[112] Wang, F. P., and Reed, R. M. 2009. Pore Networks and Fluid Flow in Gas Shales. Paper SPE 124253 presented at the Annual Technical Conference and Exhibition, SPE, New Orleans, LA, October 4-7.

[113] Warpinski, N.R., 1991. Hydraulic Fracturing in Tight Fissured Media. Paper SPE 21054, *Journal of Petroleum Technology*, **43**:2 146-152 and 208-209.

[114] Warpinski, N.R., Mayerhoffer, M.J., Vincent, M.C., Cipolla, C.L., and Lolon, E.P., 2008. Stimulating Unconventional Reservoirs: Maximizing Network Growth While Optimizing Fracture Conductivity. Paper SPE 114173 presented at the SPE Unconventional Reservoirs Conference, Keyston, Colorado, 10-12 February.

[115] Warpinski, N.R., Waltman, C.K., Du, J., and Ma, Q., 2009. Anisotropy Effects in Microseismic Monitoring. Paper SPE 14208 presented at the SPE Annual Technical Meeting and Exhibition, New Orleans, LA, 4-7 October.

[116] Warpinski, N.R., Waltman, C.K., and Weijers, L., 2010. An Evaluation of Microseismic Monitoring of Lenticular Tight-Sandstone Stimulations. Paper SPE 131776 presented at the SPE Unconventional Gas Conference held n Pittsburgh, Pennsylvania, 23-25 February.

[117] Wattenbarger, R.A., El-Banbi, A.H., Villegas, M.E., and Maggard, J.B., 1998. Production Analysis of Linear Flow into Fractured Tight Gas Wells. Paper SPE 39931 presented at the SPE Rocky Mountain Regional/Low Permeability Reservoirs Symposium and Exhibition, Denver, CO, 5-8 April.

[118] Wentworth, C. K., 1922. A scale of grade and class terms for clastic sediments, J. Geology V. 30, 377-392.

[119] Xu, X. and Davis, L.A., 1999. The Relaxation of Pore Size NMR T_2 Diffusional Relaxation in Porous Media. SPE Paper 56800 presented at the SPE Annual Technical Conference and Exhibition, Houston, TX, 3-6 October.

[120] Zhou, C.H., and Hall, F. 1994. Predicting Gas-Adsorption using 2-Dimensional Equations of State. *Industrial & Engineering Chem. Research*, 33:5, 1280-1289.

NOMENCLATURE

a'	van der Waals attraction
A	specific surface area of adsorbent, m^2/g
A_{cm}	total matrix surface area draining into fracture system, ft^2
A_s	surface area
b	Arps' hyperbolic decline exponent, dimensionless
b'	van der Waals co-volume constant (ft^3/lb-mol)
b''	intercept of $\frac{1}{q}$ versus $\sqrt{t}$ plot from Nobakht *et al.* (2010), 1/Mscf/day
B_g	gas formation volume factor, reservoir volume/surface volume
B_o	oil formation volume factor, reservoir volume/surface volume
B_w	water formation volume factor, reservoir volume/surface volume
c	heat of adsorption constant
c_t	total matrix compressibility, psi^{-1}
D_D	drawdown parameter, dimensionless
D_e	pore throat diameter, nm, μm
D_{ehs}	decline rate at end of half slope or linear acting flow, 1/d
f	fraction of porosity in the organics
f_{cp}	slope correction factor, dimensionless
G_f	free gas storage capacity, scf/ton
G_s	adsorbed gas storage capacity, scf/ton
G'_s	Raw Gibbs adsorbed gas storage capacity, scf/ton
G_{sL}	Langmuir storage capacity, scf/ton
G_{sLi}	Langmuir storage capacity of component *i*, scf/ton
G_{so}	dissolved gas-in-oil storage capacity, scf/ton
G_{st}	total gas storage capacity, scf/ton
G_{sw}	dissolved gas-in-water storage capacity, scf/ton
h	reservoir height, ft
Int	intercept on LFA plot, (psi^2/cp/Mscf/d)

k_m	matrix permeability, md
L	length
$\hat{M}$	apparent natural gas molecular weight, lbm/lbmole
$\tilde{m}$	slope of $(p_{pi} - p_{pwf})/q_g$ *versus* $\sqrt{t}$ plot, 1/ *(*day$^{1/2}$Mscfd*)*
n	number of moles adsorbed
n_c	number of components
n_f	number of fractures per completion, dimensionless
n_i°	amount of pure component adsorbed from pure gas at the same temperature and spreading pressure as the adsorbed mixture, mol/g
n_m	monolayer capacity in number of moles
n_t	total amount adsorbed, mol/g
n_1	number of moles at the start of pressure step, lb-moles
n_2	number of moles at the end of pressure step, lb-moles
n'_1	Gibbs isotherm number of moles at the start of pressure step, lb-moles
n'_2	Gibbs isotherm number of moles at the end of pressure step, lb-moles
p_L	Langmuir pressure, psia, kPa, MPa
p^o	gas vapor pressure, psia, kPa, MPa
p_i°	gas (vapor) pressure of the pure component adsorbed at the same temperature and spreading pressure as the solution
p	pressure, psia, kPa, MPa
p_c	critical pressure, psia
p_{pc}	pseudo-critical pressure, psia
p_{pi}	pseudo-pressure initial reservoir, psi^2/cp
p_{pwf}	pseudo-pressure well flowing, psi^2/cp
p_{r1}	pressure of reference cell at start, psia
p_{r2}	pressure of reference cell at end, psia
p_{s1}	pressure of sample cell at start, psia
p_{s2}	pressure of sample cell at end, psia
p_{std}	pressure, standard (14.69 psia)

P_c	capillary pressure, psia, kPa, MPa
q_1	isosteric heat of adsorption of a monolayer
q_g	gas rate, Mscf/d
q_L	molar heat of condensation
r	radius
R	universal gas constant, 10.73159 psia-ft^3/mole-R^o or 8.314 J/mol•K
R_o	Vitrinite reflectance, %
R_{so}	solution gas-oil ratio, scf/STB
R_{sw}	solution gas-water ratio, scf/STB
S	surface area
S_a	sorbed phase saturation, dimensionless
S_o	oil saturation, dimensionless
S_w	water saturation, dimensionless
t	time, days
t_{ehs}	time at end of half slope or linear acting flow, d
t_{ehsj}	time at end of half slope or linear acting flow for fraction of well j, d
T	temperature, ^{o}F, ^{o}R, ^{o}C, or K
T_c	critical temperature, ^{o}R
T_{pc}	pseudo-critical temperature, ^{o}R
T_{r1}	reference cell temperature at start, ^{o}R
T_{r2}	reference cell temperature at end, ^{o}R
T_{s1}	sample cell temperature at start, ^{o}R
T_{s2}	sample cell temperature at end, ^{o}R
T_1	NMR relaxation time cause by energy loss to environment
T_2	NMR relaxation time cause by transverse spin
V	volume
V_{De}	volume of pores with entry diameters less than D_e
V_r	reference volume, ft^3
V_T	total pore volume

V_{v0}	initial void volume, ft^3
V_{v1}	void volume step 1, ft^3
V_{v2}	void volume step 2, ft^3
x_f	fracture half-length, ft
x_i	adsorbed phase mole fraction of component i
y_e	distance from fracture to boundary (half of distance between fractures), ft
y_i	gas phase mole fraction of component i
z	compressibility factor
z_i	mole fraction of component i
z_{r1}	compressibility factor of reference cell at start
z_{r2}	compressibility factor of reference cell at end
z_{s1}	compressibility factor of sample cell at start
z_{s2}	compressibility factor of sample cell at end

Greek

α	Langmuir adsorption constant
α_{fj}	fraction of total fracture area associated with boundary time *j*, fraction
α_{ij}	separation factor or selectivity ratio, Eq. 24f
η	diffusivity, mD-psi/cp
ϕ	total porosity fraction, dimensionless
ϕ_a	sorbed phase porosity fraction, dimensionless
$\phi_{a,mix}$	sorbed phase porosity fraction of gas mixture , dimensionless
μ	viscosity, cp
π	spreading pressure
π^*	reduced spreading pressure
ρ	NMR surface relaxivity, μm/ms
ρ_b	bulk rock density, g/cm^3
ρ_{CH4}	mass density of methane in pore, g/cm^3
ρ_f	free gas phase density, g/cm^3

ρ_{Number}	number density of methane, number of molecules/ Å^3
ρ_s	sorbed phase density, g/cm^3
$\rho_{s,mix}$	sorbed phase density of the gas mixture, g/cm^3
θ	fraction of surface area covered by adsorbed molecules

Other

dx	differential of x
$n(p)$	pure component isotherm function
$(\alpha(D_e))$	pore size distribution density function

APPENDIX A

Beginning with **Eq. 10b**, the value G_s needs to be converted into a volume, a simple unit conversion can be performed. Typical units for the equation below is scf/ton.

$$G_s = G_{sL}\frac{p}{p + p_L}$$

Given that G_{sL} is in scf, we can convert scf into a mass with the ideal gas law at standard temperature and pressure:

$$V/n = RT / p$$

$$V/n = 10.73159\frac{\text{ft}^3\text{psi}}{^{\text{o}}\text{R lb - mol}}519.67\ ^{\text{o}}\text{R}\Big/14.696\ \text{psia} = 379.48\frac{\text{ft}^3}{\text{lb - mol}}$$

With density in g/cm^3 and the desired units in scf/ton, we can use the above value to calculate a conversion constant.

$$\frac{1}{379.48\frac{\text{ft}^3}{\text{lb - mol}}}\cdot\frac{1\,\text{ton}}{2000\,\text{lb}} = 1.318\times10^{-6}\frac{\text{ton mol}}{\text{ft}^3}$$

Using the conversion constant, the density of the adsorbed phase, the bulk density of the rock, and the molecular weight of the adsorbed phase we can calculate the fractional volume occupied by the sorbed phase.

$$\phi_a = 1.318\times10^{-6}\hat{M}\frac{\rho_b}{\rho_s}\left(G_{sL}\frac{p}{p + p_L}\right)$$

APPENDIX B

As shown in chapter 4, the sorbed phase density is one of the input parameters needed to determine gas storage capacities of shale. Utilizing **Eq. 15**, one can convert a Langmuir isotherm back to a raw Gibbs isotherm. As stated earlier, the Gibbs isotherm is corrected with the sorbed phase density to determine the true sorbed gas content. However, if a Langmuir isotherm was calculated with the incorrect data, then the isotherm must be transformed back into the raw data, and re-transformed with the correct density value.

$$G_s = \frac{G'_s}{1 - \frac{\rho_f}{\rho_s}} \qquad \textbf{(A1)}$$

Utilizing the Langmuir constants in for shale 'A' in **Table 6**, and **Eq. 15** (above), the **Table B**, below was created. This table shows the original isotherm, the re-calculated raw Gibbs isotherm and the corrected Langmuir Isotherm. The sorbed phase density used to determine the first isotherm was 0.4233 g/cm^3, the sorbed phase density that was used for the correction was 0.375 g/cm^3. Also, the data is presented graphically in **Fig. B.**

Pressure psia	Gas z factor	Report Langmuir (scf/ton) Gs (0.4233 g/cm^3)	Gibbs Correction Factor (0.4233 g/cm3)	Gibbs Raw Isotherm (scf/ton)	Corrected Gibbs Correction Factor	Corrected Langmuir (scf/ton) Gs (0.375 g/cm^3)
0.00	1.00	0.00	0.0000	0.00	0.0000	0.00
500.00	0.97	15.15	0.9543	14.46	0.9484	15.25
1000.00	0.94	23.26	0.9059	21.07	0.8937	23.57
1500.00	0.92	28.30	0.8559	24.22	0.8373	28.93
2000.00	0.91	31.75	0.8059	25.58	0.7809	32.76
2500.00	0.91	34.25	0.7574	25.94	0.7262	35.72
3000.00	0.92	36.14	0.7118	25.73	0.6747	38.13
3500.00	0.94	37.63	0.6698	25.21	0.6273	40.19
4000.00	0.96	38.83	0.6315	24.52	0.5840	41.99

Table B - Table showing Langmuir isotherm calculated with a density of 0.4233 g/cc. Back-calculated, raw Gibbs Isotherm and a re-calculated Langmuir isotherm with more accurate sorbed phase density.

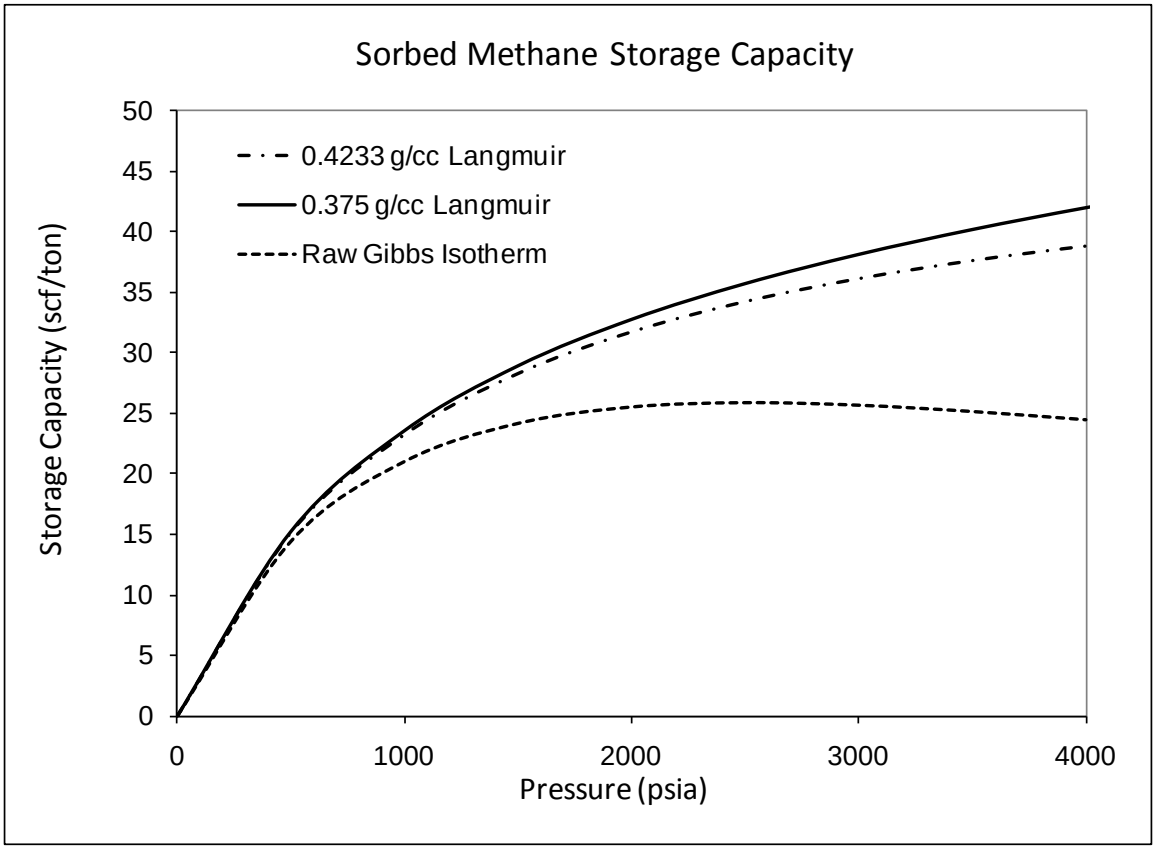

Fig. B - Langmuir isotherm calculated from Raw Gibbs Isotherm, one using a 0.4233 g/cm^3 sorbed phase density, the other using a 0.375 g/cm^3 sorbed phase density.